อิทธิพลของความหนาต่อการกระจายของตัวประกอบความเข้มของความเค้น

นาย กิตติศักดิ์ สุยสุทธิ์

วิทยานิพนธ์นี้เป็นส่วนหนึ่งของการศึกษาตามหลักสูตรปริญญาวิศวกรรมศาสตรมหาบัณฑิต
สาขาวิชาวิศวกรรมโยธา ภาควิชาวิศวกรรมโยธา
คณะวิศวกรรมศาสตร์ จุฬาลงกรณ์มหาวิทยาลัย
ปีการศึกษา 2553

INFLUENCE OF THICKNESS ON DISTRIBUTION OF STRESS INTENSITY FACTORS

MR. KITTISAK SUISUT

A Thesis Submitted in Partial Fulfillment of the Requirements
for the Degree of Master of Engineering Program in Civil Engineering

Department of Civil Engineering
Faculty of Engineering
Chulalongkorn University

Academic Year 2010

Thesis Title	INFLUENCE OF THICKNESS ON DISTRIBUTION OF STRESS INTENSITY FACTORS
By	Mr. Kittisak Suisut
Field of Study	Civil Engineering
Thesis Advisor	Assistant Professor Jaroon Rungamornrat, Ph.D.

Accepted by the Faculty of Engineering, Chulalongkorn University in Partial Fulfillment of the Requirements for the Master's Degree

..... Dean of the Faculty of Engineering

(Associate Professor Boonsom Lerdhirunwong, Dr.Ing.)

THESIS COMMITTEE

..... Chairman

(Professor Teerapong Senjuntichai, Ph.D.)

..... Thesis Advisor

(Assistant Professor Jaroon Rungamornrat, Ph.D.)

..... Examiner

(Assistant Professor Watanachai Smittakorn, Ph.D.)

..... External Examiner

(Assistant Professor Sasikorn Leungvichcharoen, D.Eng.)

กิตติศักดิ์ สุยสุทธิ์ : อิทธิพลของความหนาต่อการกระจายของตัวประกอบความเข้มของความเค้น. (INFLUENCE OF THICKNESS ON DISTRIBUTION OF STRESS INTENSITY FACTORS) อ.ที่ปรึกษาวิทยานิพนธ์หลัก: ผศ.ดร. จรูญ รุ่งอมรรัตน์, 82 หน้า.

วิทยานิพนธ์ฉบับนี้นำเสนอผลการศึกษาอิทธิผลของความหนาของชิ้นส่วนทดสอบแบบ CT ที่มีต่อการกระจายตัวของตัวประกอบความเข้มของความเค้นแบบเปิดตามขอบของรอยแตกร้าว โดยทำการจำลองชิ้นส่วนทดสอบ CT แบบสามมิติที่ความหนาต่างๆกัน เพื่อให้สามารถคำนวณค่าตัวประกอบความเข้มของความเค้นที่จุดต่างๆตลอดขอบรอยแตกร้าวได้ ข้อมูลดังกล่าวนี้ทำให้ทราบพฤติกรรมบริเวณที่ใกล้กับจุดที่ขอบรอยแตกร้าวตัดกับผิวของชิ้นส่วนทดสอบซึ่งค่าตัวประกอบความเข้มของความเค้นมีอัตราการเปลี่ยนแปลงสูง และทราบความกว้างของขอบรอยแตกร้าวที่มีค่าตัวประกอบความเข้มของความเค้นค่อนข้างคงที่หรือมีพฤติกรรมความเครียดแบบระนาบสำหรับชิ้นส่วนทดสอบที่มีความหนาต่างๆกัน การวิเคราะห์ปัญหารอยแตกร้าวแบบสามมิติใช้ระเบียบวิธีบาวดารีเอลิเมนต์แบบสมมาตรของกาเลอร์คินชนิดเอกฐานอย่างอ่อน ซึ่งเป็นระเบียบวิธีเชิงตัวเลขที่นิยมใช้ในการแก้ปัญหารอยแตกร้าวซึ่งให้ผลเฉลยเชิงตัวเลขที่มีความถูกต้องสูงและประหยัดค่าใช้จ่ายในการคำนวณ สมการกำกับเชิงปริพันธ์เกี่ยวข้องเฉพาะพื้นผิวของชิ้นส่วนที่ทำการจำลองเท่านั้น ดังนั้นจำเป็นต้องสร้างโครงตาข่ายสำหรับใช้ในการประมาณผลเฉลยเฉพาะบริเวณผิวของชิ้นส่วนทดสอบและผิวของรอยแตกร้าวเท่านั้น นอกจากนี้ชิ้นส่วนพิเศษได้ถูกนำมาใช้สำหรับจำลองพฤติกรรมบริเวณขอบรอยแตกร้าวเพื่อให้สามารถคำนวณค่าตัวประกอบความเข้มของความเค้นได้สะดวกและมีความถูกต้องมากยิ่งขึ้นแม้ว่าชิ้นส่วนพิเศษที่ใช้จะมีขนาดค่อนข้างใหญ่ก็ตาม วิทยานิพนธ์ฉบับนี้นำเสนอและสรุปผลที่ได้จากการศึกษาชิ้นส่วนทดสอบ CT ทั้งในกรณีที่ทำมาจากวัสดุยืดหยุ่นเชิงเส้นประเภทไอโซโทรปิกและประเภททรานเวอร์สลีไอโซโทรปิก

ภาควิชา วิศวกรรมโยธา ลายมือชื่อนิสิต .....

สาขาวิชา วิศวกรรมโยธา ลายมือชื่อ อ.ที่ปรึกษาวิทยานิพนธ์หลัก .....

ปีการศึกษา 2553

#5070220621 : MAJOR CIVIL ENGINEERING

KEYWORDS : THICKNESS EFFECT / CRACKS/ STRESS INTENSITY FACTORS/ SGBEM/ WEAKLY SINGULAR

KITTISAK SUISUT: INFLUENCE OF THICKNESS ON DISTRIBUTION OF STRESS INTENSITY FACTORS. ADVISOR: ASST.PROF. JAROON RUNGAMORNRAT, Ph.D., 82 pp.

This thesis offers an extensive investigation of the influence of specimen thickness on the distribution of the mode-I stress intensity factor (SIF) along the fracture front of the compact tension specimen. The analysis is carried out in a fully 3D context and the characteristic of the SIF-distribution and width of the layer in the vicinity of surface breaking points where the stress intensity factor exhibits rapid variation and the layer where the SIF is nearly constant are thoroughly examined for various thicknesses of testing specimens. In the modeling, a well-known numerical technique, called a weakly-singular symmetric Galerkin boundary element method (SGBEM), is employed. The most attractive features of this technique include that the mesh generation cost is comparatively cheap since only 2D discretization on the outer boundary of the specimen and on the fracture surface is required and the calculated stress intensity factor along the fracture front is highly accurate with use of relatively coarse mesh. The latter feature results from applications of high order, special crack-tip elements in the local region surrounding the fracture front along with the use of a direct formula to extract the SIF. Extensive results are reported and discussed for specimens made from both isotropic and transversely isotropic materials.

Department : Civil Engineering Student's Signature .....

Field of Study : Civil Engineering Advisor's Signature .....

Academic Year : 2010 .....

ACKNOWLEDGEMENTS

This thesis could not successfully completed without my thesis advisor. I would like to thank him very much. My advisor, Assist. Prof. Dr. Jaroon Rungamornrat, who gave good advice, idea and guidance. My thesis committees, who gave me for all of good comments and suggestions. And the special thanks for the Department of Civil Engineering, Faculty of Engineering, Chulalongkorn University gave an opportunity to study in Master's Degree. Finally, this graduation would not be achieved without my parents. Mr. Nuyuk and Mrs. Aree Suisut, who help me in everything. I cannot describe overall if I write it.

CONTENTS

Page

LIST OF TABLES

LIST OF FIGURES

Page

Page

Page

Page

Page

CHAPTER I

INTRODUCTION

1.1 General

Small defects and flaws are unavoidably introduced in components during the manufacturing and fabrication process or initiated during applications as a result of external excitations. Defects and flaws present in the component act as the stress riser and, in turn, the strength reducer due to the high stress concentration introduced in their neighborhood and this can eventually lead to progressive failure of such component once certain critical conditions have been attained. Fracture and fatigue analysis and assessment have therefore become essential ingredients in the design of engineering components to ensure their safety and integrity under service conditions. To aid such analysis, physically admissible, mathematical models and powerful solution techniques must be developed in order to capture and predict responses of interest with acceptable level of accuracy.

In general, fractures can be classified as either brittle fractures or ductile fractures depending on their dominant failure characteristic and behavior of fields in the vicinity of the fracture front. Behavior of the ductile fracture is dominated primarily by the significant plastic deformation induced around the front while the brittle fracture is characterized by a rapid rate of crack advance with relatively row energy release and a localized plastic deformation, i.e. small-scale yielding pertains (see for examples, Anderson, 2005; Gdoutos, 2005). Common mathematical models used in the modeling of the latter type of fractures are established within the context of linear elastic fracture mechanics (LEFM). For this particular case, a localized zone of plastic deformation is discarded and the entire body including a region of high stress concentration is assumed to be linearly elastic. A single parameter, either the stress intensity factor or the strain energy release rate, can be used to completely describe the dominant or asymptotic field in the neighborhood of the crack front (K-field). For ductile fractures, the

size of a region with inelastic deformation is relatively large when compared with the crack dimension and the K-field predicted by LEFM does not exist. Various models based on elastic-plastic fracture mechanics (EPFM) have been proposed instead to improve the response prediction (see Anderson, 2005). For this type of fractures, two different parameters, one associated with the J-integral and the other corresponding to the crack opening displacement, have been widely used to measure the extent of fields around the crack front. It should be remarked that while LEFM-based analysis yields certain unrealistic aspects of the fields near the crack front (e.g. singularity of the stress and strain field at the crack front), results from such analysis have been used successfully in the response prediction for various engineering applications (e.g. fatigue analysis, prediction of crack growth initiation and propagation direction, etc.). The present study is focused only on brittle fractures.

The stress intensity factor is a fundamental quantity in linear elastic fracture mechanics that provides a complete measure of a dominant field in the vicinity of the crack front and, in particular, indicates the extent or magnitude of an asymptotic, singular stress field (e.g. Williams, 1957). In general, the stress intensity factor depends on several factors such as loading conditions, material properties, geometries of both bodies and cracks and the location along the crack front, and determination of such quantity requires solving a complete boundary value problem associated with the entire body. Supported by evidences from various experiments (e.g. Krishna Rao and Hasebe, 1995 and Xin *et al*., 2010), a body containing pre-existing cracks, when loaded, only deforms without creating any new surface for a certain range of applied loads. Once the applied load reaches a critical value (i.e. the corresponding stress intensity factor reaches its critical value), crack growth initiation is observed. The critical value of the stress intensity factor at the onset of crack advance is termed the fracture toughness. This quantity, generally taken as a property of materials, indicates the ability of the constituting material to resist the formation of a new surface. Fracture toughness can be determined from experiments following various well-known standards such as the British standard (BS), the American Society for Testing and Materials (ASTM), a series of

International Standard (ISO) and the European Structural Integrity Society (ESIS). Among several types of specimens and crack configurations found in earlier experimental studies (e.g. single-edge notched bending (SEB), compact tension (CT), arc-shaped tension (AT) and disk-shaped compact tension (DCT) specimens), the two most common specimens widely used to determine the fracture toughness are the single-edge notched bending (SEB) specimen and the compact tension (CT) specimen as shown schematically in Figure 1.1 according to ASTM E399-90 (1997).

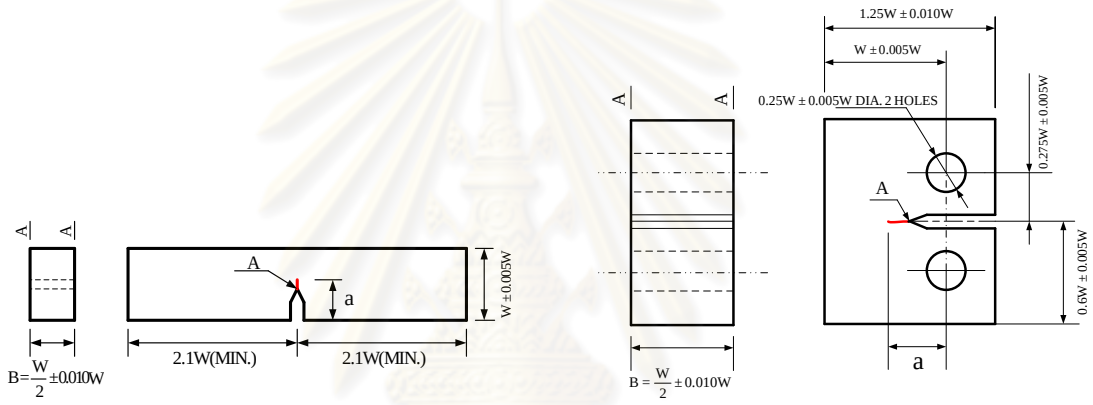

Figure 1.1 Schematic of specimen configuration and crack: (a) single-edge notched bending (SEB) specimen and (b) compact tension (CT) specimen

Results from many experiments revealed that the fracture toughness exhibits strong dependence on the thickness of a specimen used as shown in Figure 1.2 (e.g. Anderson, 2005). A thinner specimen generally yields larger fracture toughness. As the specimen thickness increases to a certain value, the fracture toughness converges to a constant value termed the plane strain fracture toughness and denoted by K_{IC}. The plane strain fracture toughness represents a true material property since it is independent of the specimen thickness and this situation can be achieved only when the specimen thickness is sufficiently large to render the behavior over the majority of the crack front dominated by a plane strain condition. The ASTM E399-90 (1997) recommended the minimum specimen thickness to obtain a valid K_{IC} by

$$B \geq 2.5\left(\frac{K_{IC}}{\sigma_y}\right)^2 \tag{1.1}$$

where B is the specimen thickness, K_{IC} is the plane strain fracture toughness to be determined, and σ_y is the yield strength of constituting material. Inequality (1.1) was developed based on the assumption that the plastic zone size must be relatively small compared to the specimen thickness (i.e. $r_p \leq B/50$ where r_p is the plastic zone size along the crack front) and its applicability is still restricted to fractures at room temperature and high-strength materials. In addition, the estimation of the specimen thickness by (1.1) involves K_{IC} which is unknown a priori.

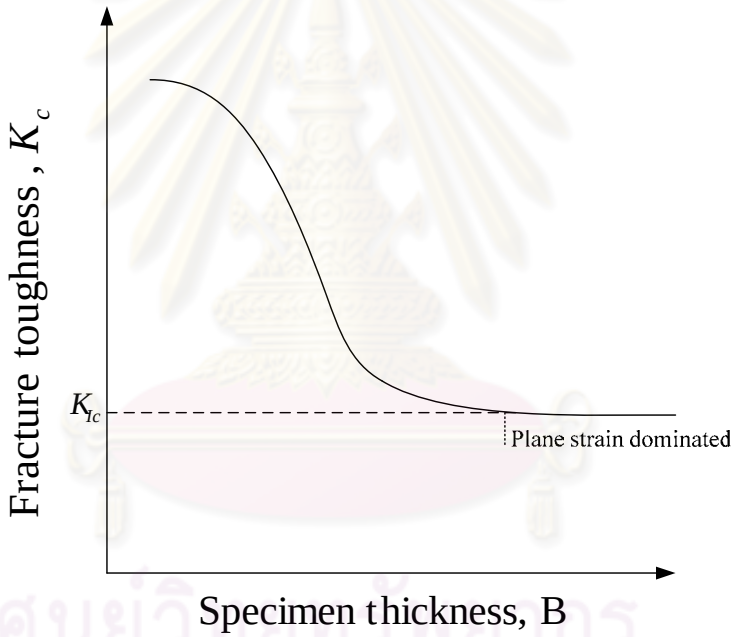

Figure 1.2 Relationship between fracture toughness K_c and specimen thickness B

An alternative to the above recommended empirical formula is to apply linear elastic fracture mechanics to perform comprehensive three-dimensional stress analysis along with an extensive parametric study on the specimen thickness. Knowledge of the distribution of the stress intensity factor along the entire crack front for various specimen thicknesses should at least provide useful information for selecting a proper specimen thickness to ensure that the plane strain condition is dominated and, as a result, the plane strain fracture toughness is obtained. More specifically, the

thickness of the specimen can be increased in the simulation until the stress intensity factor over the majority of the crack front attains the value corresponding to the plane strain condition.

1.2 Background and review

A mathematical model formulated within the context of two-dimensional boundary value problems has been widely used in the stress analysis of a body containing defects and flaws due to its simplicity and cheap computational cost while still predicting results with an acceptable level of accuracy for several engineering applications. On the basis of an extensive literature survey, various studies on two-dimensional crack problems based on both the plain stress and plain strain assumptions were recorded (e.g. Chang and Mear, 1995; Dirgantara and Aliabadi, 2002; Khraishi and Demir, 2003; Freese and Baratta, 2006; Kutak *et al*., 2007). It should be noted first that the former assumption is well-suited for modeling a body of a relatively small thickness in comparison with other dimensions whereas the latter is appropriate for components of comparatively large thickness. Here, details of some selected studies from this category are given. Dirgantara and Aliabadi (2002) applied the dual boundary element method to solve an elastic thin plate containing three types of cracks (i.e. centered crack, edge crack and cracks emanating from a hole). In their study, the crack surface displacement extrapolation (CSDE) technique was utilized along with the J-integral scheme to determine the stress intensity factors. Numerical results obtained were found to be in excellent agreement with existing benchmark solutions. Freese and Baratta (2006) thoroughly investigated a single edge-cracked specimen by using the weight function method and the modified mapping collocation technique. In their parametric study, the full range of crack length to specimen width ratio and various loading conditions such as three-point and four-point bending, pure bending, eccentrically loaded tension were considered. General explicit expressions for computing the stress intensity factors were also deduced. Recently, Kutak *et al.* (2007) proposed explicit formula for approximating the mode-I stress intensity factor for center crack, single edge crack, and double edge crack in a linearly elastic thin plate under

the normal traction. In their work, the neural networks and the displacement extrapolation method (DEM) were employed to determine the stress intensity factor and a commercial FEM-package, ANSYS, was utilized to validate their numerical results. Expressions of the stress intensity factors for two-dimensional cracked bodies with various geometries, crack configurations, and loading conditions can also be found in many textbooks of fracture mechanics (e.g. Barsom and Rolfe, 1999; Anderson, 2005; Gdoutos, 2005). While use of a two-dimensional mathematical model to perform fracture analysis gains popularity from its simplicity, it still poses several drawbacks. As already been known, a two-dimensional model with the plane stress assumption is well-suited only for modeling a body of a relatively small thickness in comparison with other dimensions whereas that based on the plane strain assumption is appropriate for components of comparatively large thickness. In practices, there are various situations that both plane stress and plane strain assumptions do not apply (e.g. components with) and, for those cases, fracture data (viz. stress intensity factors) exhibits strong dependence on the component dimensions. To gain more insight into such complex boundary value problems, a comprehensive three-dimensional analysis must be performed.

In past decades, work related to three-dimensional linear fracture analysis has increasingly gained attention from various researchers due to the significant progress of powerful numerical techniques and personal computers and the need of more sophisticated mathematical models to better predict responses of complex physical problems encountered in practices. Here, we summarize a series of earlier studies relevant to the present study. Alam and Mendelsen (1983) utilized the method of line to study the mode-I stress intensity factor along the curved crack front of the compact tension specimen (according to the ASTM standard) under pure tension loading. Results from their study revealed that the distribution of the stress intensity along the crack front exhibits strong dependence on the difference between the crack length at the center of the crack front and the crack length at the boundary of the specimen, termed the crack tunnel depth. In particular, the stress intensity factor

decreases in the central region of the crack front while increases over a small region near the intersection between the crack front and the outer boundary as the crack tunnel depth increases. Although such analysis was performed within the three-dimensional context, the specimen thickness was fixed and, as a result, the influence of this parameter on the distribution of the stress intensity factor cannot be addressed.

Later, Sukumar *et al*. (1997) developed a numerical technique based on the coupling between the finite element method and the element-free Galerkin method to solve an isotropic, linearly elastic, single edge cracked specimen subjected to the uniform normal traction at its top and bottom surfaces. The element-free Galerkin method was employed specially to model the crack surface and the stress intensity factor along the crack front is calculated using the volume and planar domain integral. It can be concluded from this study that the stress intensity factor attains its maximum value at the middle of the crack front and decreases very rapidly in the region where the crack front meets the boundary. In addition, the complete distribution of the stress intensity factor along the crack front obtained from such analysis shows significant discrepancy from the plane strain case and this additionally supports the need of the three-dimensional model. It should be noted however that this study is restricted only to a specimen of fixed thickness and an isotropic material with Poisson's ratio equal to 0.3. This is still insufficient to describe the influence of the thickness on the distribution of the stress intensity factor along the entire crack front. Next, Li *et al*. (1998) presented highly accurate numerical solutions of an identical problem by using a powerful numerical technique based on a weakly singular, symmetric Galerkin boundary element method (SGBEM). However, the main focus of this work was to develop the computational procedure and this particular problem chosen in their analysis was only for verification purpose.

Next, Wu (2006) explored the influence of thickness on the distribution of the mode-I stress intensity factor for the center-cracked specimen subjected to uniform normal traction at its top and bottom surfaces. In the analysis, a finite element software ANSYS was utilized to model the associated boundary value problem and the quarter-

point displacement method was employed to extract the stress intensity factor along the crack front. Results from this study indicated that the stress intensity factor in the central region of the crack front starts to attain a converged constant value (i.e. the plane strain condition) for a specimen with the thickness larger than four times of the crack length. It should be noted that their study is still restricted only to a center-cracked specimen made of an isotropic material with Poisson's ratio equal to 0.3. Later, Kotosov (2007) applied the first order plate theory to investigate the influence of the plate thickness on the value of the stress intensity factors for a through crack embedded in a linearly elastic infinite plate of finite thickness and subjected to both remote uniaxial tension and remote shear. Results from this study suggested that when the thickness of the plate increases, the stress intensity factors decreases and finally converges to the value associated with the plane strain condition. While the analysis has taken the thickness of the plate into account, use of the plate theory provides no information of the distribution of the stress intensity factors across the thickness. In particular, a single value of the stress intensity factor was obtained and it should represent only the average of such quantity over the entire crack front. Recently, Rungamornrat and Mear (2008b) revisited the same problem as that studied by Li *et al.* (1998) by incorporating material anisotropy. In their analysis, the weakly singular SGBEM based on a pair of weakly singular, weak-form integral equations for the displacement and traction proposed by Rungamornrat and Mear (2008a) was utilized. Similar to the work of Li *et al.* (1998), the key objective of this study was to develop an efficient and accurate numerical technique capable of performing three-dimensional linear fracture analysis. The distribution of the stress intensity factors along the crack front was reported and discussed for an isotropic material with Poisson's ratio equal to 1/3 and two types of transversely isotropic materials, i.e. zinc and graphite reinforced composite. However, the study did not consider the influence of the thickness on the value of the stress intensity factors.

From an extensive literature survey, the studies of the influence of the thickness of the body in the direction along the crack front on the value and distribution of the stress intensity factors are still restricted to certain geometries, crack

configurations, loading conditions, and certain types of constituting materials. For instance, complete investigation in the case of isotropic materials is limited to certain values of Poisson's ratio and specimen geometries while results for anisotropic case are available only for a specimen with a fixed thickness.

1.3 Research Objective

The key objective of this research is to explore the influence of the thickness of specimens, commonly used in the determination of the fracture toughness, on the distribution of stress intensity factors along the crack front.

1.4 Research Scope

The main focus of this research is to perform a stress analysis of a compact tension (CT) specimen of various thicknesses and under pure mode-I loading condition. Dimensions of the specimen and loading characteristics are chosen to be consistent with those specified in ASTM E399-90. Two types of materials, one associated with an isotropic elastic material and the other corresponding to a transversely isotropic elastic material, are considered in this study. For the latter type of material, the axis of material symmetry is taken to be perpendicular to the crack surface.

1.5 Research Methodology

A computational procedure based on a weakly singular, symmetric Galerkin boundary element method (SGBEM) is utilized to perform the comprehensive stress analysis of a three-dimensional, homogeneous, generally anisotropic, linearly elastic medium containing cracks. The stress intensity factor is computed using a special formula in terms of the gradient of the relative crack-face displacement data along the crack front which is obtained directly from the SGBEM.

1.6 Research Significance

Results from the present study provide the profound understanding of the behavior of the mode-I stress intensity factor along the entire crack front of the CT

specimen of various thicknesses for two important classes of linearly elastic materials, i.e. isotropic and transversely isotropic solids. The knowledge of the specimen thickness that yields the plane strain condition over the majority of the crack front has a direct application to the optimal design of a CT specimen used in the determination of the fracture toughness.

CHAPTER II

THEORETICAL BACKGROUND

This chapter devotes to the fundamental background in linear elastic fracture mechanics and the formulation of the boundary value problem associated with a cracked body. First, a stress field in the vicinity of the crack front and the definition of the stress intensity factors are briefly summarized. Next, a pair of weakly-singular weak-form boundary integral equations for the displacement and traction is presented. Finally, a symmetric weak formulation governing the three-dimensional crack problem is established.

2.1 Stress field near the crack front

Consider a crack embedded in a linearly elastic body as shown schematically in Figure 2.1. A reference local Cartesian coordinate system is chosen, for convenience, such that its origin is located at the crack front, the x_1-axis is normal to the crack front, the x_2-axis is normal to the crack surface and the x_3-axis is tangent to the crack front. Let (r, θ, x_3) denote a local cylindrical coordinate system defined based on the local (x_1, x_2, x_3) system as shown in Figure 2.1. By following the previous work by Westergaard (1939), Sneddon (1946), Irwin (1957) and Williams (1957), the stress field in the neighborhood of the crack front takes the following form

$$\sigma_{ij} = \left(\frac{k}{\sqrt{r}}\right)\tilde{\sigma}_{ij}(\theta) + \sum_{m=0}^{\infty} C_m r^{\frac{m}{2}} \hat{\sigma}_{ij}^{(m)}(\theta) \tag{2.1}$$

where σ_{ij} denote the Cartesian stress components; k is a constant depending on applied load, geometry of the body and crack, material properties, and location along the crack front; r is the distance from the crack front to a point of interest; $\tilde{\sigma}_{ij}$ is an angular dependent function; m is a non-negative integer; C_m are constants; and $\hat{\sigma}_{ij}^{(m)}$ are angular dependent functions.

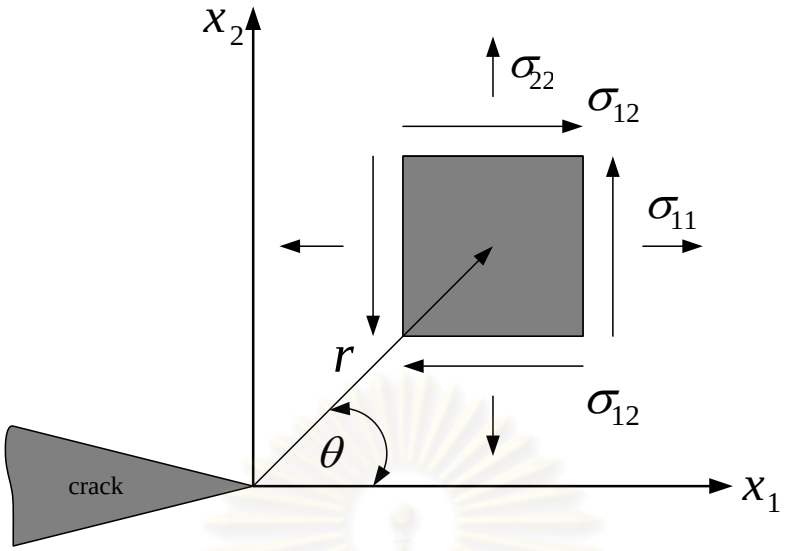

Figure 2.1 Schematic indicating stress field in the x_1-x_2 plane near the crack front

As apparent from above equation, the stress field near the crack front can be decomposed into two different parts where the first part (i.e. the second term on the right-hand side of (2.1)) remains finite and possesses a zero limit as r approaches zero and the second part (i.e. the first term on the right-hand side of (2.1)) is proportional to the inverse square-root function $1/\sqrt{r}$ which becomes infinite at the crack front. As approaching the crack front, the stress field is clearly dominated by the first term and, within the context of linear elastic fracture mechanics, the second term is typically discarded. The asymptotic stress field (generally known as the K-field) exhibits the singularity of order $1/\sqrt{r}$ and its characteristic can be completely determined by a single parameter k. Influence of loading conditions (including the magnitude and loading direction), properties of constituting materials, and geometry of the body and cracks on such local stress field is reflected through the constant k.

2.2 Stress intensity factors

The stress intensity factor, denoted by K, is an essential parameter in linear elastic fracture mechanics that is known to completely characterize the dominant stress field in the neighborhood of the crack front. This fracture data is directly related to the constant k in the expansion (2.1) via a simple relation:

$$K = k\sqrt{2\pi} \tag{2.2}$$

By inserting (2.2) into the first term on the right-hand side of (2.1), the dominant stress field now becomes

$$\sigma_{ij} = \left(\frac{K}{\sqrt{2\pi r}}\right)\tilde{\sigma}_{ij}(\theta) \tag{2.3}$$

From the eigen analysis, the above asymptotic stress field can be decomposed into three independent modes, i.e. the opening mode or mode I, the sliding mode or mode II and the tearing mode or mode III, corresponding to the different behavior of the relative crack-face displacement. More specifically, the component of the general relative crack-face displacement perpendicular to the crack surface, parallel to the crack surface and normal to the crack front, parallel to the crack surface and tangent to the crack front corresponds to the mode I, mode II and mode III, respectively, as shown in Figure 2.2. For general geometries and loading conditions, all three modes exist and the local stress field (2.3) can further be written in a form

$$\sigma_{ij} = \left(\frac{K_I}{\sqrt{2\pi r}}\right)\tilde{\sigma}_{ij}^{I}(\theta) + \left(\frac{K_{II}}{\sqrt{2\pi r}}\right)\tilde{\sigma}_{ij}^{II}(\theta) + \left(\frac{K_{III}}{\sqrt{2\pi r}}\right)\tilde{\sigma}_{ij}^{III}(\theta) \tag{2.4}$$

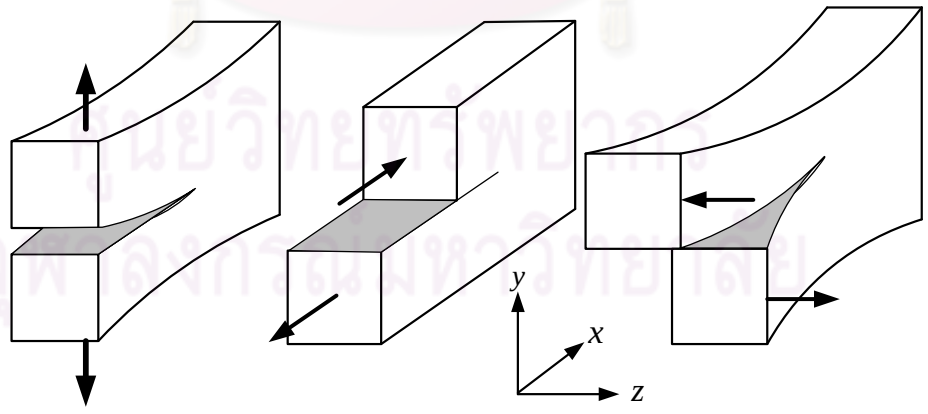

(a) (b) (c)

Figure 2.2 Schematics indicating the relative crack-face displacement for (a) mode I or opening mode, (b) mode II or sliding mode, and (c) mode III or tearing mode

where K_I, K_{II} and K_{III} are mode-I, mode-II and mode-III stress intensity factors, respectively, and $\tilde{\sigma}_{ij}^{I}$, $\tilde{\sigma}_{ij}^{II}$ and $\tilde{\sigma}_{ij}^{III}$ are corresponding functions describing the angular dependent behavior in the local region surrounding the crack front. The stress intensity factors for all three modes can be obtained from the local stress field resulting from solving a complete boundary value problem via following formulas

$$K_I = \lim_{r\to 0}\left(\sqrt{2\pi r}\,\sigma_{22}(r,\theta=0)\right) \tag{2.5}$$

$$K_{II} = \lim_{r\to 0}\left(\sqrt{2\pi r}\,\sigma_{12}(r,\theta=0)\right) \tag{2.6}$$

$$K_{III} = \lim_{r\to 0}\left(\sqrt{2\pi r}\,\sigma_{23}(r,\theta=0)\right) \tag{2.7}$$

It is remarked that the definitions (2.5)-(2.7) apply to both isotropic and generally anisotropic materials. Barnett and Asaro (1972) and Xu (2000) proposed an alternative expression for determining the mixed-mode stress intensity factors for generally anisotropic media in terms of the relative crack-face displacement:

$$k_i = \frac{\sqrt{2\pi}}{4} B_{il} \lim_{x_1\to 0^-}\left(\frac{\Delta u_l}{\sqrt{-x_1}}\right) \tag{2.8}$$

where k_i are related to the stress intensity factors by $k_1 = K_{II}$, $k_2 = K_I$, $k_3 = K_{III}$; Δu_l are components of relative crack-face displacement with respect to the local coordinate system (x_1, x_2, x_3) defined in Figure 2.1; and B_{il} are constants involving all elastic constants and the geometry of the crack front by

$$B_{il} = \frac{1}{2\pi}\int_0^{2\pi}\left[(\mathbf{a},\mathbf{a})_{il} - (\mathbf{a},\mathbf{b})_{im}(\mathbf{b},\mathbf{b})^{-1}_{mn}(\mathbf{b},\mathbf{a})_{nl}\right]d\phi \tag{2.9}$$

where **a** and **b** are orthonormal vectors contained in the plane defined by $x_3 = 0$; ϕ is the angle between the vector **a** and the x_1-axis; the operator $(\cdot,\cdot)$ is defined in terms of the elastic constants E_{ijkl} by $(\mathbf{a},\mathbf{b})_{ij} = a_m E_{mijn} b_n$; and $(\mathbf{b},\mathbf{b})^{-1}$ denotes the inverse of $(\mathbf{b},\mathbf{b})$. The formula (2.8) can be used, when supplemented by positive features of the selected numerical scheme, to accurately and efficiently compute the stress intensity factor along the crack front for both isotropic and anisotropic cases. The explicit form of the angular dependent functions $\tilde{\sigma}_{ij}^{I}$, $\tilde{\sigma}_{ij}^{II}$ and $\tilde{\sigma}_{ij}^{III}$ for certain special cases (e.g. two-

dimensional problem with both plane stress and plane strain assumptions, anti-plane shear problem, etc.) can be found in textbooks for fundamental fracture mechanics (e.g. Anderson, 2005; Gdoutos, 2005; Barsom and Rolfe, 1999; Kanninen and Popelar, 1985; Hellan, 1984).

2.3 Boundary integral equations for cracked body

It is evident from sections 2.1 and 2.2 that the asymptotic and eigen analysis provide only information about the form of dominant elastic fields in the neighborhood of the crack front but leaving several important information such as loading conditions, geometries and material properties in terms of unknown constants termed the stress intensity factors. This essential fracture data can be determined once the complete boundary value problem associated with the entire body is solved. The local stress field in the region surrounding the crack front and the relative crack-face displacement resulting from such comprehensive stress analysis can be used to extract the stress intensity factors via the relations (2.5)-(2.7) or (2.8). In the present study, a numerical technique based on the weakly-singular, symmetric Galerkin boundary element method (SGBEM) is selected to perform such stress analysis. In this section, we briefly summarize a set of boundary integral equations essential for the development of the SGBEM.

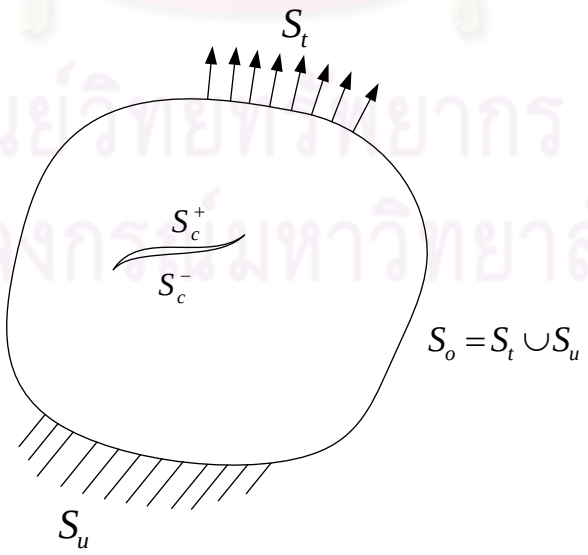

Figure 2.3 Schematic of three-dimensional cracked body

Consider a three-dimensional, finite, cracked body that is made of a generally anisotropic, linearly elastic material as shown in Figure 2.3. The boundary of the body can be decomposed into three surfaces $S_C^+ \cup S_C^-$, S_u, and S_t where $S_C^+ \cup S_C^-$ represents two geometrically coincident crack surfaces, S_u is a portion of the regular boundary on which the displacement is fully prescribed, and S_t is the remaining regular boundary on which the traction is prescribed. It is remarked that on the crack surface the traction is assumed to be known.

A pair of completely regularized boundary integral equations for the displacement and the traction applicable to a cracked body made of a generally anisotropy material was proposed by Rungamornrat and Mear (2008a). The final form of those two equations are given by

$$\begin{aligned}\frac{1}{2}\int_{S_o}\tilde{t}_p(\mathbf{y})\,u_p(\mathbf{y})\,dS(\mathbf{y}) &= \int_{S_o}\tilde{t}_p(\mathbf{y})\int_{S_o}U_j^p(\boldsymbol{\xi}-\mathbf{y})t_j(\boldsymbol{\xi})\,dS(\boldsymbol{\xi})\,dS(\mathbf{y}) \\ &+ \int_{S_o}\tilde{t}_p(\mathbf{y})\int_{S}G_{mj}^p(\boldsymbol{\xi}-\mathbf{y})D_m v_j(\boldsymbol{\xi})\,dS(\boldsymbol{\xi})\,dS(\mathbf{y}) \\ &- \int_{S_o}\tilde{t}_p(\mathbf{y})\int_{S}n_i(\boldsymbol{\xi})H_{ij}^p(\boldsymbol{\xi}-\mathbf{y})v_j(\boldsymbol{\xi})\,dS(\boldsymbol{\xi})\,dS(\mathbf{y})\end{aligned} \tag{2.10}$$

$$\begin{aligned}-\int_{S}c(\mathbf{y})\tilde{v}_k(\mathbf{y})t_k(\mathbf{y})\,dS(\mathbf{y}) &= \int_{S}D_t\tilde{v}_k(\mathbf{y})\int_{S}C_{mj}^{tk}(\boldsymbol{\xi}-\mathbf{y})D_m v_j(\boldsymbol{\xi})\,dS(\boldsymbol{\xi})\,dS(\mathbf{y}) \\ &+ \int_{S}D_t\tilde{v}_k(\mathbf{y})\int_{S_o}G_{tk}^j(\boldsymbol{\xi}-\mathbf{y})t_j(\boldsymbol{\xi})\,dS(\boldsymbol{\xi})\,dS(\mathbf{y}) \\ &+ \int_{S}\tilde{v}_k(\mathbf{y})\int_{S_o}n_l(\mathbf{y})H_{lk}^j(\boldsymbol{\xi}-\mathbf{y})t_j(\boldsymbol{\xi})\,dS(\boldsymbol{\xi})\,dS(\mathbf{y})\end{aligned} \tag{2.11}$$

where $S_o = S_u \cup S_t$, $S = S_u \cup S_t \cup S_c^+$, $\tilde{t}_p$ and $\tilde{v}_k$ are admissible test functions, $D_m(\cdot) = n_i\varepsilon_{ijm}\partial(\cdot)/\partial\xi_j$ denotes a surface differential operator, ε_{ijm} is a permutation symbol, $c(\mathbf{y})$ is a geometric dependent function defined by $c(\mathbf{y}) = 1/2$ for $\mathbf{y} \in S_o$ and $c(\mathbf{y}) = 1$ for $\mathbf{y} \in S_c^+$, $t_i(\boldsymbol{\xi})$ denotes the traction at point $\boldsymbol{\xi}$ on the boundary, $v_i(\boldsymbol{\xi})$ is the boundary data defined by

$$v_i(\boldsymbol{\xi}) = \begin{cases} u_i(\boldsymbol{\xi}) \ , & \boldsymbol{\xi} \in S_o \\ \Delta u_i(\boldsymbol{\xi}) \ , & \boldsymbol{\xi} \in S_c^+ \end{cases} \tag{2.12}$$

with $u_i(\boldsymbol{\xi})$ and $\Delta u_i(\boldsymbol{\xi}) = u_i^+(\boldsymbol{\xi}) - u_i^-(\boldsymbol{\xi})$ denoting the displacement on the regular boundary and the jump in the displacement across the crack surface. All four kernels appearing in above two integral equations are given explicitly by

$$H_{ij}^p(\boldsymbol{\xi}-\mathbf{y}) = -\frac{1}{4\pi}\frac{(\xi_i - y_i)\delta_{pj}}{r^3} \tag{2.13}$$

$$U_i^p(\boldsymbol{\xi}-\mathbf{y}) = K_{mp}^{mi}(\boldsymbol{\xi}-\mathbf{y}) \tag{2.14}$$

$$G_{mj}^p(\boldsymbol{\xi}-\mathbf{y}) = \varepsilon_{abm}E_{ajdc}K_{cp}^{bd}(\boldsymbol{\xi}-\mathbf{y}) \tag{2.15}$$

$$C_{mj}^{tk}(\boldsymbol{\xi}-\mathbf{y}) = A_{mjdn}^{tkoe}K_{dn}^{oe}(\boldsymbol{\xi}-\mathbf{y}) \tag{2.16}$$

where δ_{ij} is a Kronecker delta and the constant A_{mjdn}^{tkoe} and the function $K_{jl}^{ik}(\boldsymbol{\xi}-\mathbf{y})$ are defined by

$$A_{mjdn}^{tkoe} = \varepsilon_{pam}\varepsilon_{pbt}\left(E_{bknd}E_{ajeo} - \frac{1}{3}E_{ajkb}E_{dneo}\right) \tag{2.17}$$

$$K_{jl}^{ik}(\boldsymbol{\xi}-\mathbf{y}) = \frac{1}{8\pi r^2}\oint_{\mathbf{z}\cdot\mathbf{r}=0}(\mathbf{z},\mathbf{z})_{kl}^{-1}z_i z_j ds(\mathbf{z}) \tag{2.18}$$

where $\mathbf{r} = \boldsymbol{\xi} - \mathbf{y}$ denotes the position vector, $r = \sqrt{\mathbf{r}\cdot\mathbf{r}}$, $\mathbf{z}$ is a unit vector, $(\mathbf{z},\mathbf{z})_{kl} = z_m E_{mklp} z_p$, and the closed contour integral is defined on a unit circle on a plane normal to the position vector $\mathbf{r}$ (i.e. $\mathbf{z}\cdot\mathbf{r} = 0$). It is worth noting that the kernels $U_i^p(\boldsymbol{\xi}-\mathbf{y})$, $G_{mj}^p(\boldsymbol{\xi}-\mathbf{y})$ and $C_{mj}^{tk}(\boldsymbol{\xi}-\mathbf{y})$ are material dependent and possess the same structure in terms of the line integral whereas the kernel $H_{ij}^p(\boldsymbol{\xi}-\mathbf{y})$ is independent of elastic constants. In addition, all four kernels are singular only at $\boldsymbol{\xi} = \mathbf{y}$ and are of order $\mathcal{O}(1/r)$ (see details of derivations and extensive discussion of these kernels in the work of Rungamornrat and Mear, 2008a). For the special case of isotropy, i.e. $E_{ijkl} = \mu\left[\delta_{ik}\delta_{jl} + \delta_{il}\delta_{jk} + 2\nu\delta_{ij}\delta_{kl}/(1-2\nu)\right]$ where μ is the elastic shear modulus and ν is Poisson's ratio, the closed contour integral (2.18) can be integrated explicitly and the kernels $U_i^p(\boldsymbol{\xi}-\mathbf{y})$, $G_{mj}^p(\boldsymbol{\xi}-\mathbf{y})$ and $C_{mj}^{tk}(\boldsymbol{\xi}-\mathbf{y})$ now simply reduce to a closed form identical to those obtain by Li and Mear (1998) and Li *et al*. (1998):

$$U_i^p(\boldsymbol{\xi}-\mathbf{y})=\frac{1}{16\pi(1-\nu)\mu}\left(\frac{3-4\nu}{r}\delta_{ip}+\frac{(\xi_i-y_i)(\xi_p-y_p)}{r^3}\right) \tag{2.19}$$

$$G_{mj}^p(\boldsymbol{\xi}-\mathbf{y})=\frac{1}{8\pi(1-\nu)r}\left((1-2\nu)\varepsilon_{mpj}+\frac{(\xi_t-y_t)(\xi_p-y_p)}{r^2}\varepsilon_{tjm}\right) \tag{2.20}$$

$$C_{mj}^{tk}(\boldsymbol{\xi}-\mathbf{y})=\frac{\mu}{4\pi(1-\nu)r}\left((1-\nu)\delta_{tk}\delta_{mj}+2\nu\delta_{km}\delta_{jt}-\delta_{kj}\delta_{tm}-\frac{(\xi_j-y_j)(\xi_k-y_k)}{r^2}\delta_{tm}\right) \tag{2.21}$$

The boundary integral equations (2.10) and (2.11) possess several positive features useful for the present study including that (i) they are cast in a weak form well-suited for establishing the symmetric weak formulation for the SGBEM discussed in the following section, (ii) all kernels are only weakly singular of $\mathcal{O}(1/r)$ allowing all involved integrals be interpreted in an ordinary sense and only requiring displacement data on the regular boundary and crack of the type C^0 for those integrals to be valid, (iii) they are applicable to cracks of general geometries and under arbitrary loading conditions, and (iv) they apply to both isotropic and generally anisotropic linearly elastic media.

2.4 Symmetric weak formulation for crack problem

To construct a symmetric weak formulation associated with the boundary value problem for a cracked body, a standard procedure similar to that employed by Li et al. (1998) and Rungamornrat and Mear (2008b) is employed. In such procedure, a pair of weakly singular, weak-form integral equations for the displacement and traction (2.10) and (2.11) is employed as follows. On the surface S_u, the displacement integral equation (2.10) is applied by choosing a test function such that $\tilde{t}_p=0$ on S_t and on the surface S_t, the traction integral equation (2.11) is applied with a special choice of test function satisfying $\tilde{v}_p=0$ on $S_u\cup S_c^+$. Finally, on a single crack surface S_c^+, the traction integral equation (2.11) is again applied by choosing a test function $\tilde{v}_p=\Delta\tilde{u}_p$ on S_c^+ and $\tilde{v}_p=0$ on $S_o=S_u\cup S_t$. A set of weak-form equations resulting from appropriate applications to each surface is given in a concise form by (also see Li *et al.*, 1998; Rungamornrat and Mear, 2008b)

$$\begin{aligned} \mathcal{A}_{uu}(\tilde{\boldsymbol{t}},\boldsymbol{t}) &+ \mathcal{B}_{ut}(\tilde{\boldsymbol{t}},\boldsymbol{u}) &+ \mathcal{B}_{uc}(\tilde{\boldsymbol{t}},\boldsymbol{\Delta u}) &= \mathcal{R}_1(\tilde{\boldsymbol{t}}) \\ \mathcal{B}_{ut}(\boldsymbol{t},\tilde{\boldsymbol{u}}) &+ \mathcal{C}_{tt}(\tilde{\boldsymbol{u}},\boldsymbol{u}) &+ \mathcal{C}_{tc}(\tilde{\boldsymbol{u}},\boldsymbol{\Delta u}) &= \mathcal{R}_2(\tilde{\boldsymbol{u}}) \\ \mathcal{B}_{uc}(\boldsymbol{t},\boldsymbol{\Delta}\tilde{\boldsymbol{u}}) &+ \mathcal{C}_{ct}(\boldsymbol{\Delta}\tilde{\boldsymbol{u}},\boldsymbol{u}) &+ \mathcal{C}_{cc}(\boldsymbol{\Delta}\tilde{\boldsymbol{u}},\boldsymbol{u}) &= \mathcal{R}_3(\boldsymbol{\Delta}\tilde{\boldsymbol{u}}) \end{aligned} \tag{2.22}$$

where the linear operators $\mathcal{A}_{PQ}$, $\mathcal{B}_{PQ}$ and $\mathcal{C}_{PQ}$ (with $P,Q \in \{u,t,c\}$) are given in terms of weakly singular, double surface integrals by

$$\mathcal{A}_{PQ}(\boldsymbol{X},\boldsymbol{Y}) = \int_{S_P} X_k(\mathbf{y}) \int_{S_Q} U_i^k(\boldsymbol{\xi}-\mathbf{y}) Y_i(\boldsymbol{\xi}) dS(\boldsymbol{\xi}) dS(\mathbf{y}) \tag{2.23}$$

$$\begin{aligned} \mathcal{B}_{PQ}(\boldsymbol{X},\boldsymbol{Y}) = &\int_{S_P} X_k(\mathbf{y}) \int_{S_Q} G_{mj}^k(\boldsymbol{\xi}-\mathbf{y}) D_m Y_j(\boldsymbol{\xi}) dS(\boldsymbol{\xi}) dS(\mathbf{y}) \\ &- \int_{S_P} X_k(\mathbf{y}) \int_{S_Q} n_m(\boldsymbol{\xi}) H_{mj}^k Y_j(\boldsymbol{\xi}) dS(\boldsymbol{\xi}) dS(\mathbf{y}) \end{aligned} \tag{2.24}$$

$$\mathcal{C}_{PQ}(\boldsymbol{X},\boldsymbol{Y}) = \int_{S_P} D_t X_k(\mathbf{y}) \int_{S_Q} C_{mj}^{tk}(\boldsymbol{\xi}-\mathbf{y}) D_m Y_j(\boldsymbol{\xi}) dS(\boldsymbol{\xi}) dS(\mathbf{y}) \tag{2.25}$$

and the operators $\mathcal{R}_1$, $\mathcal{R}_2$ and $\mathcal{R}_3$ involving the prescribed data on the boundary are given by

$$\mathcal{R}_1(\tilde{\boldsymbol{t}}) = \mathcal{F}_u(\tilde{\boldsymbol{t}},\boldsymbol{u_o}) - \mathcal{A}_{ut}(\tilde{\boldsymbol{t}},\boldsymbol{t_o}) - \mathcal{B}_{uu}(\tilde{\boldsymbol{t}},\boldsymbol{u_o}) \tag{2.26}$$

$$\mathcal{R}_2(\tilde{\boldsymbol{u}}) = -\mathcal{F}_t(\tilde{\boldsymbol{u}},\boldsymbol{t_o}) - \mathcal{B}_{tt}(\boldsymbol{t_o},\tilde{\boldsymbol{u}}) - \mathcal{C}_{tu}(\tilde{\boldsymbol{u}},\boldsymbol{u_o}) \tag{2.27}$$

$$\mathcal{R}_3(\boldsymbol{\Delta}\tilde{\boldsymbol{u}}) = -2\mathcal{F}_c(\boldsymbol{\Delta}\tilde{\boldsymbol{u}},\boldsymbol{t_c}) - \mathcal{B}_{tc}(\boldsymbol{t_o},\boldsymbol{\Delta}\tilde{\boldsymbol{u}}) - \mathcal{C}_{cu}(\boldsymbol{\Delta}\tilde{\boldsymbol{u}},\boldsymbol{u_o}) \tag{2.28}$$

in which the integral operator $\mathbf{F}_P$ (with $P \in \{u,c,t\}$) are given in terms of a regular single surface integral by

$$\mathcal{F}_P(\boldsymbol{X},\boldsymbol{Y}) = \frac{1}{2}\int_{S_P} X_i(\mathbf{y}) Y_i(\mathbf{y}) dS(\mathbf{y}). \tag{2.29}$$

The symmetry of the weak formulation (2.22) should be obvious from the form of the integral operators $\mathcal{A}_{PQ}$ and $\mathcal{C}_{PQ}$ and the symmetry of the kernels $U_i^p(\boldsymbol{\xi}-\mathbf{y})$ and

$C_{mj}^{tk}(\boldsymbol{\xi}-\mathbf{y})$. This set of integral equations forms a complete boundary value problem for a body containing cracks in terms of unknown boundary data such as the traction on the surface S_u, the displacement on the surface S_t and the relative crack-face displacement on the crack surface S_c^+. For a special case of pure traction boundary value problems (i.e. $S_u = \phi$), the weak formulation (2.22) simply reduces to

$$\begin{aligned} \mathrm{C}_{tt}(\tilde{\mathbf{u}},\mathbf{u}) \quad &+ \mathrm{C}_{tc}(\tilde{\mathbf{u}},\Delta\mathbf{u}) \quad = \mathrm{R}_2(\tilde{\mathbf{u}}) \\ \mathrm{C}_{ct}(\Delta\tilde{\mathbf{u}},\mathbf{u}) &+ \mathrm{C}_{cc}(\Delta\tilde{\mathbf{u}},\Delta\mathbf{u}) = \mathrm{R}_3(\Delta\tilde{\mathbf{u}}) \end{aligned} \tag{2.30}$$

where $\mathcal{R}_2$ and $\mathcal{R}_3$ are now given by

$$\mathrm{R}_2(\tilde{\mathbf{u}}) = -\mathrm{F}_t(\tilde{\mathbf{u}},\mathbf{t}_o) - \mathrm{B}_{tt}(\mathbf{t}_o,\tilde{\mathbf{u}}) \tag{2.31}$$

$$\mathrm{R}_3(\Delta\tilde{\mathbf{u}}) = -2\mathrm{F}_c(\Delta\tilde{\mathbf{u}},\mathbf{t}_c) - \mathrm{B}_{tc}(\mathbf{t}_o,\Delta\tilde{\mathbf{u}}) \tag{2.32}$$

The formulation (2.22) is employed later as a basis for the development of the weakly singular SGBEM.

CHAPTER III
SOLUTION PROCEDURE

In this chapter, we summarize a numerical technique utilized to solve the boundary value problem associated with a cracked body, the post-process to extract the stress intensity factor from the data along the crack front, a meshing procedure for the CT specimen, and the mesh refinement and study of convergence of numerical solutions.

3.1 Weakly singular SGBEM

To solve the boundary value problem for a cracked body governed by a set of integral equations (2.22), a weakly singular SGBEM developed by Li *et al*. (1998) for cracks in isotropic media and by Rungamornrat and Mear (2008b) for cracks in generally anisotropic media is adopted. Due to the weakly singular nature of the governing integral equations and the symmetry of the formulation, this numerical technique is superior to other standard boundary integral equation methods in several aspects. For instance, C^0 interpolation functions can be used in the discretization of all boundary data, all singular integrals exist in an ordinary sense and can be integrated accurately and efficiently using some standard quadrature, and it finally results in a symmetric system of linear algebraic equations. It should be remarked also that the discretization is required only on the boundary of the domain and the crack surface and this renders the reduction of the spatial dimension from 3 to 2 for three-dimensional problems. Unlike the standard finite element method (e.g. Hughes, 2000), the discretization is required for the entire domain and the meshing effort is non-trivial especially in the region near the crack front where an extremely fine mesh is required to accurately capture the singularity of the stress field (e.g. Swenson and Ingraffea, 1988; Martha *et al*., 1993; Ayhan *et al*., 2003). For the SGBEM developed by Li *et al*. (1998) and Rungamornrat and Mear (2008b), the asymptotic behavior of the field near the crack front as discussed in sections 2.1 and 2.2 is directly and properly integrated into

the near front approximation allowing relatively coarse meshes be employed to construct reasonably accurate numerical results. Here, we only summarize some important aspects of the SGBEM adopted in the present study while details of the development can be found in the work of Li *et al*. (1998) and Rungamornrat and Mear (2008b).

3.1.1 Discretization

The unknown displacement and traction on the regular boundary of the domain are approximated by using continuous interpolation functions defined in an element-wise fashion on standard, two-dimensional, isoparametric, C^0 elements (e.g. Hughes, 2000) resulting from the discretization. The relative crack-face displacement along the crack front is approximated by special continuous interpolation functions via the use of special crack-tip elements developed by Li *et al*. (1998) and Rungamornrat and Mear (2008b). The relative crack-face displacement on the remaining of the crack surface is approximated by the interpolation functions from standard, two-dimensional, isoparametric, C^0 elements. It should be noted that for the CT specimen considered in this study, the crack front intersects the regular boundary at two particular points known as vertices. Since shape functions on the crack-tip elements and on the standard elements are different, an element on the regular boundary which contains the vertex and is adjacent to the crack-tip element must be modified to maintain the continuity of the displacement field. This can be achieved by using a special element developed by Li *et al*. (1998).

3.1.2 Evaluation of kernels

For an isotropic case, all four kernels $H_{ij}^{p}(\boldsymbol{\xi}-\mathbf{y})$, $U_{i}^{p}(\boldsymbol{\xi}-\mathbf{y})$, $G_{mj}^{p}(\boldsymbol{\xi}-\mathbf{y})$ and $C_{mj}^{tk}(\boldsymbol{\xi}-\mathbf{y})$ are given in an explicit form in terms of fundamental functions. Thus, evaluation of these kernels for every pair of source and field points $(\boldsymbol{\xi},\mathbf{y})$ is trivial. For the case of generally anisotropic materials, the kernel $H_{ij}^{p}(\boldsymbol{\xi}-\mathbf{y})$ can still be directly calculated while the evaluation of the kernels $U_{i}^{p}(\boldsymbol{\xi}-\mathbf{y})$, $G_{mj}^{p}(\boldsymbol{\xi}-\mathbf{y})$ and $C_{mj}^{tk}(\boldsymbol{\xi}-\mathbf{y})$ by directly integrating the closed contour integral (2.18) for every pair $(\boldsymbol{\xi},\mathbf{y})$ can lead to massive computational cost. In this study, the interpolation technique proposed by Rungamornrat and Mear (2008b) is utilized to avoid such direct integration.

3.1.3 Numerical integration

All regular, single surface integrals are accurately and efficiently integrated by using standard Gaussian quadrature. For double surface integrals, three types of integrals including regular integrals, singular integrals and nearly singular integrals are encountered after the discretization. All regular integrals can be efficiently evaluated using standard Gaussian quadrature while both singular and nearly singular integrals are integrated numerically using special quadratures developed by Xiao (1998). Positive features of those special quadratures are that the integration can be performed in the computational domain (i.e. master element), the singularity and rapid variation behavior are removed via using proper variable transformations, and the accuracy of the scheme finally controlled by adjusting the number of Gauss points.

3.1.4 Solution of system of linear equations

A final system of linear algebraic equations resulting from the discretization is symmetric and also positive definite for pure traction boundary value problems as considered in the present study. It is worth noting that proper constraints must be introduced in order to eliminate the rigid body translations and rigid body rotations or, equivalently, to ensure that the system of linear equations possesses a unique solution. For three-dimensional, pure traction boundary value problems, six constraints are needed. To solve such a symmetric, positive definite system of linear equations, a standard conjugate gradient method with Jacobi-preconditioning is utilized (e.g. Hamming, 1987; Chapra and Canale, 1990). The obtained solution (for pure traction boundary value problems) contains nodal displacements on the regular boundary, nodal relative crack-face displacements on the crack surface, and extra degrees of freedom along the crack front resulting from the use of crack-tip elements. The last quantities are associated with the gradient of the relative crack-face displacement along the crack front and they can be used in the determination of the stress intensity factors as discussed in the following section.

3.2 Determination of stress intensity factors

It is apparent that a solution obtained directly from the weakly singular SGBEM contains nodal quantities (displacements, tractions, and relative crack-face

displacement) on the regular boundary and the crack surface. The elastic field within the body (e.g. stress and displacement) can also be computed using the integral relations proposed by Rungamornrat and Mear (2008a). If only the stress intensity factors are of interest, the definition (2.8) offers a better candidate comparing to the definition in terms of the stress (2.5)-(2.7) in order to avoid the computation of the field within the body. It is noted however that the direct use of the definition (2.8) still requires the evaluation of the limit and this calculation may affect the accuracy of the stress intensity factors. To enhance the accuracy, Rungamornrat and Mear (2008b) employed a special feature of the crack-tip element along with (2.8) to develop an explicit, limit-free formula for determining the mixed-mode stress intensity factors as follows

$$k_i(\mathbf{x}_c) = \sqrt{\frac{\pi}{2J\sin\beta}} B_{il}(\mathbf{x}_c) \sum_{n=1}^{N} u^e_{l(n)} \psi_{(n)}(\mathbf{x}_c) \tag{3.1}$$

where $\mathbf{x}_c$ is any point on the crack front; J and β are parameters depending on the geometry of the crack-tip element at point $\mathbf{x}_c$ (see more details in the work of Rungamornrat and Mear, 2008b); N denotes the number of nodes in the crack-tip element; $u^e_{l(n)}$ is the nodal degree of freedom associated with the n^{th} node; and $\psi_{(n)}(\mathbf{x}_c)$ is the value of the nodal shape function at point $\mathbf{x}_c$. It is worth noting that $\psi_{(n)}(\mathbf{x}_c)$ is zero for all shape functions associated with nodes not located on the crack front; as a result, the summation appearing in the expression (3.1) involves only extra nodal degrees of freedom along the crack front. In addition, components of all quantities in the formula (3.1) are referring to the local coordinate system defined in section 2.1.

By using the crack-tip elements to approximate the relative crack-face displacement near the crack front along with applying the explicit formula (3.1) in the determination of the stress intensity factors, Rungamornrat and Mear (2008b) found that highly accurate results can be obtained by using only relatively coarse meshes. With such attractive feature, the formula (3.1) is therefore utilized in the present study.

3.3 Geometries of CT specimen

In the present study, we focus only on a particular cracked body with its configuration similar to a compact tension (CT) testing specimen. ASTM E399-90 (1997)

has recommended the geometries of the CT specimen in the experiment for the plane strain fracture toughness K_{IC} as shown in Figure 3.1. The ratio between the crack length a (measured from the center of each hole to the crack front) and the specimen width W (measured from the center of each hole to the back face of the specimen) must be chosen in the range of 0.45 to 0.55 and the thickness is recommended to be $0.5W$. The entire width (measured from the back face to the front face) is equal to $1.25W$. A pair of equal and opposite loads is to be applied at the holes of radius $0.25W$ to open the crack. The distance between the center of each hole and the crack plane is equal to $0.275W$ and the distance from the crack plane to the top and bottom surface of the specimen is equal to $0.6W$. Details of a small starter notch in front of the crack plane can be found in ASTM E399-90 (1997).

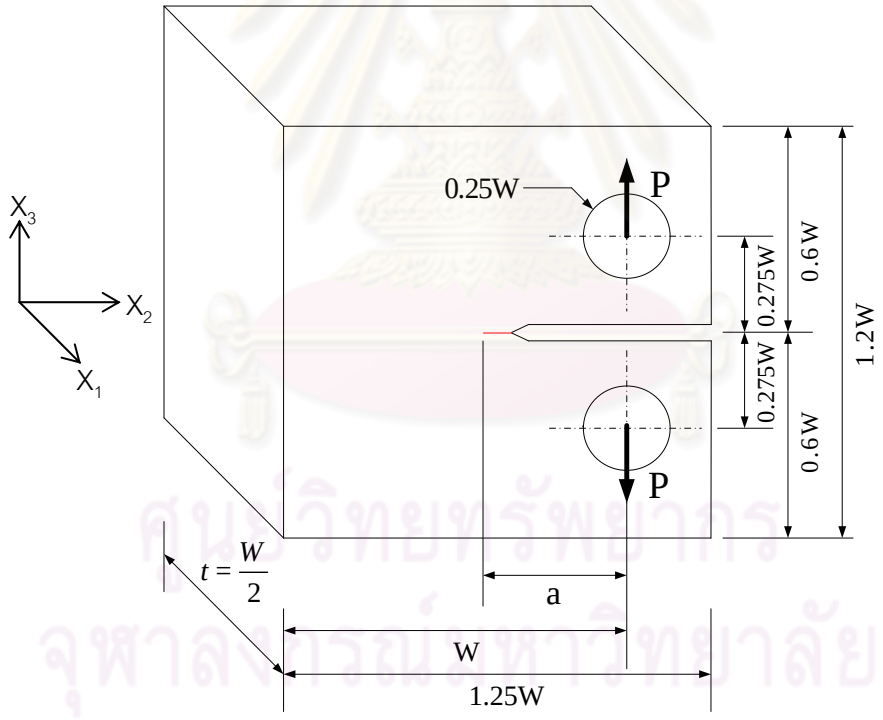

Figure 3.1 Configuration of compact tension (CT) specimen recommended by ASTM E399-90 (1997)

In the modeling, we choose a configuration as shown in Figure 3.2 to represent the CT specimen shown in Figure 3.1. The difference between this model and the actual CT specimen is due to the removal of the notch and then replacing it by a

through-the-thickness crack. It is worth noting that this simplification should not significantly alter the behavior of the problem but substantially reduces the meshing effort. In the analysis, we choose $a/W = 0.5$ and the thickness of the specimen is varied in order to investigate its influence on the distribution of the stress intensity factor. The applied loads at both holes are assumed to be uniformly distributed over the upper part of the upper hole and the lower part of the hole.

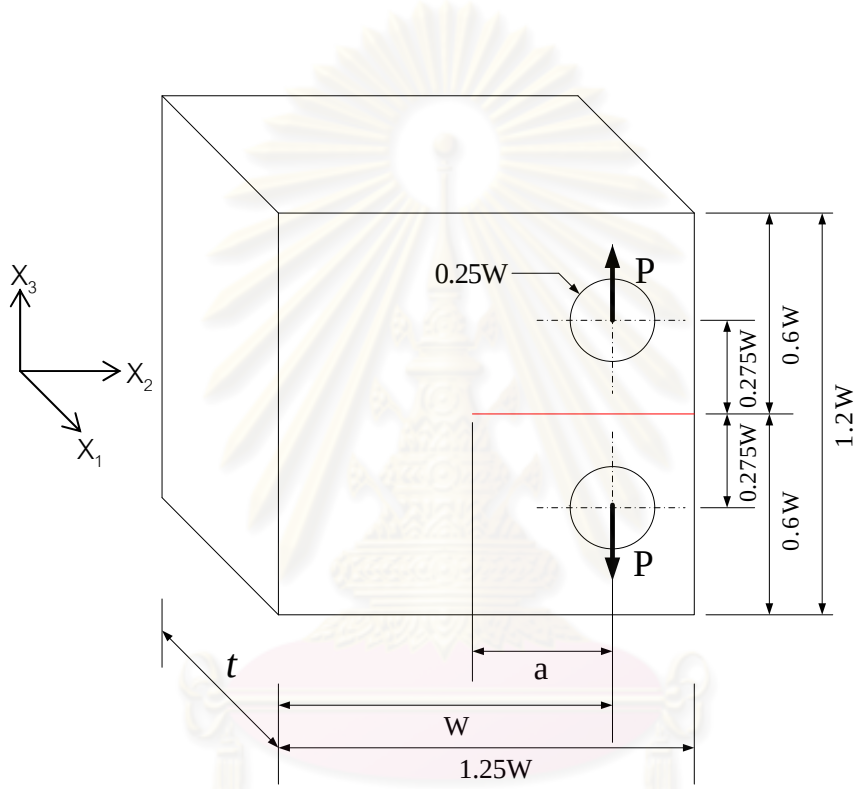

Figure 3.2 Configuration of compact tension (CT) specimen used in the analysis

3.4 Mesh generation

In the construction of a finite element mesh on the boundary of the CT specimen and the crack surface, the number of distorted elements and elements with a large aspect ratio is minimized, a finer mess is utilized in regions where fields are anticipated to be complex such as regions near the crack front and vertices, and a mesh with smooth transition is employed to connect the fine mesh region and the coarse mesh region. Three types of elements are utilized in the discretization of the CT specimen: (i) standard 6-node triangular elements and standard 8-node quadrilateral

elements shown in Figure 3.3(a)-(b), (ii) 9-node quadrilateral crack-tip elements shown in Figure 3.3(c), and (iii) special 9-node quadrilateral elements shown in Figure 3.3(d). More specifically, elements in the second category are utilized only along the entire crack front whereas on the front and back faces of the specimen, two elements of the last type must be used to connect the crack-tip element and the standard elements. The remaining boundary and crack surface are discretized by elements in the first category.

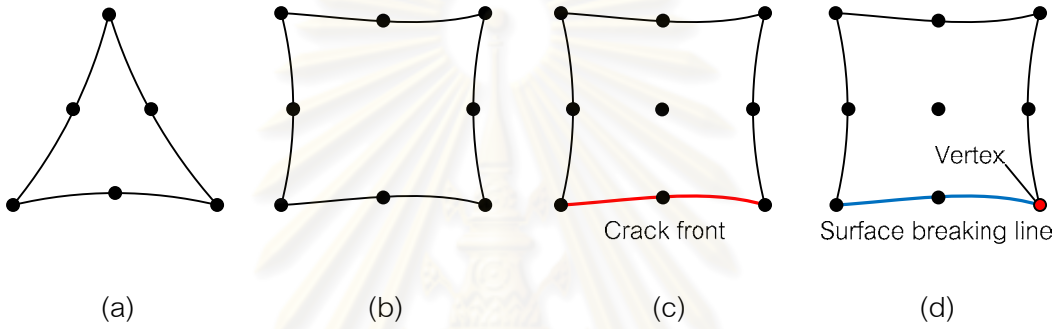

Figure 3.3 Schematic of elements utilized in the discretization of CT specimen: (a) standard 6-node triangular element, (b) standard 8-node quadrilateral element, (c) 9-node crack-tip element, and (d) special 9-node quadrilateral element

An example of a mesh for the CT specimen of a particular thickness $t/a=1$ is shown in Figure 3.4. By exploiting the symmetry of its geometry, the mesh generation effort can be significantly reduced. For instance, only one of the top and bottom surfaces, one of the two holes, one half of the two side-faces, and one half of the crack surface are required to be meshed. Meshes for the remaining boundary and crack surface can simply be obtained by the reflection about a plane of symmetry. It is evident also that only a region on the crack surface close to the crack front (see Figure 3.4(b)) and a region on the two side-faces surrounding the vertices (see Figure 3.4(c)) have a relatively finer mesh when compared with the other regions. Most of the effort and care is therefore spent to achieve a good mesh in such region and the corresponding transition zone. A good quality mesh with sufficient refinement is anticipated to yield accurate stress intensity factors along the entire crack front.

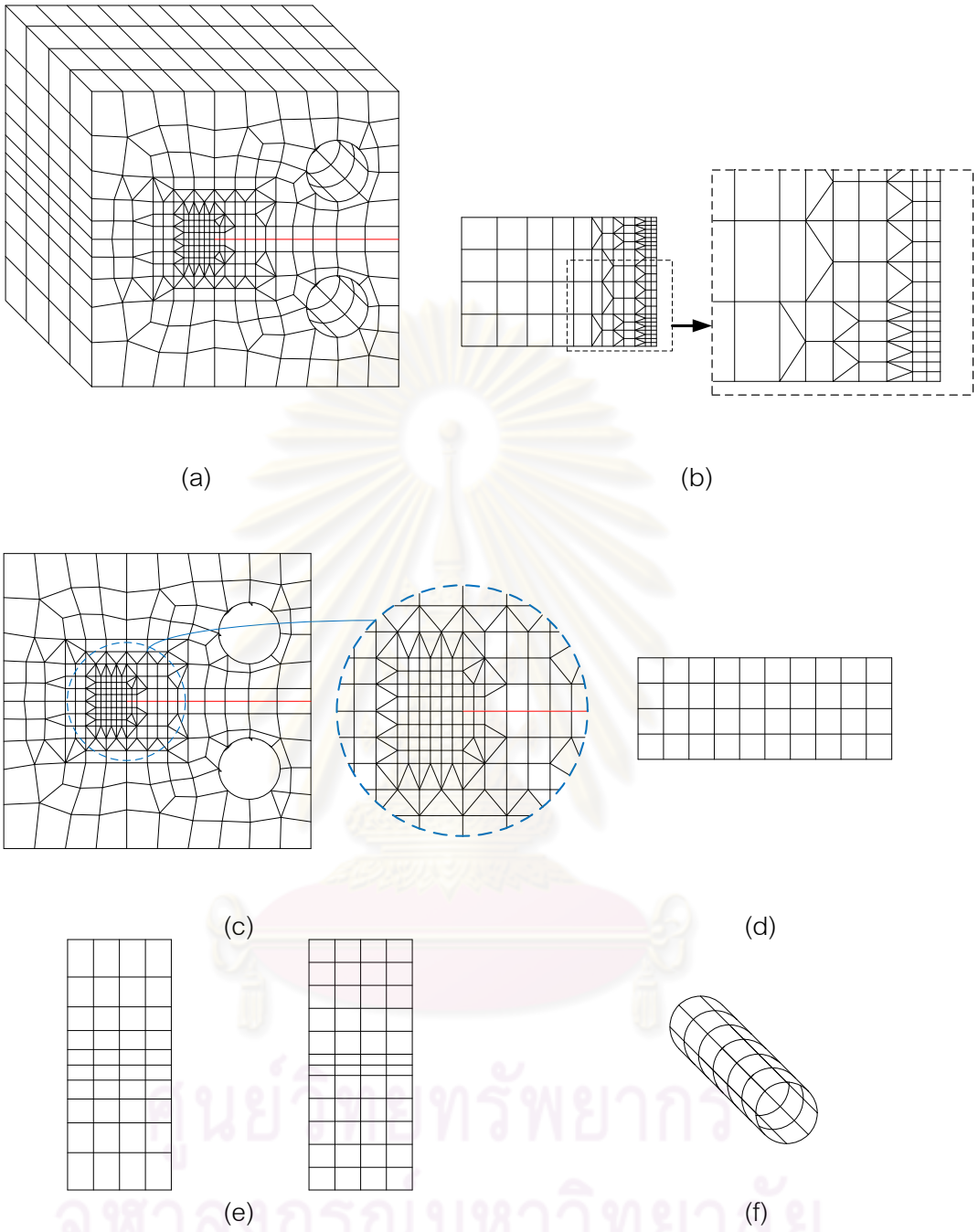

Figure 3.4 Example of mesh for CT specimen of thickness $t/a=1$: (a) mesh for entire specimen, (b) mesh for crack surface, (c) mesh for side faces, (d) mesh for top and bottom surfaces, (e) mesh for back and front faces, and (f) mesh for holes

3.5 Convergence study

The main focus of this section is to explore the convergence of the stress intensity factor along the crack front using a series of meshes with different levels of

refinement. Results from this convergence study are very useful in the selection of a mesh that yields accurate numerical solutions while requiring relatively cheap computational cost.

In the study, three meshes, a coarse mesh denoted by Mesh-1, a medium mesh denoted by Mesh-2 and a fine mesh denoted by Mesh-3, are constructed as shown in Figures 3.5-3.7 for a specimen of thickness $t/a = 1$. The number of nodes and elements on the crack surface and the remaining boundary for the three meshes is reported in Table 3.1. In the analysis, we consider three different materials, one associated with an isotropic material with Poisson's ratio $\nu = 0.30$ and the other two corresponding to the transversely isotropic material with elastic constants chosen to be those for zinc and cadmium as given in Table 3.2. It should be noted that for the last two materials, the axis of material symmetry is chosen to direct perpendicular to the crack surface.

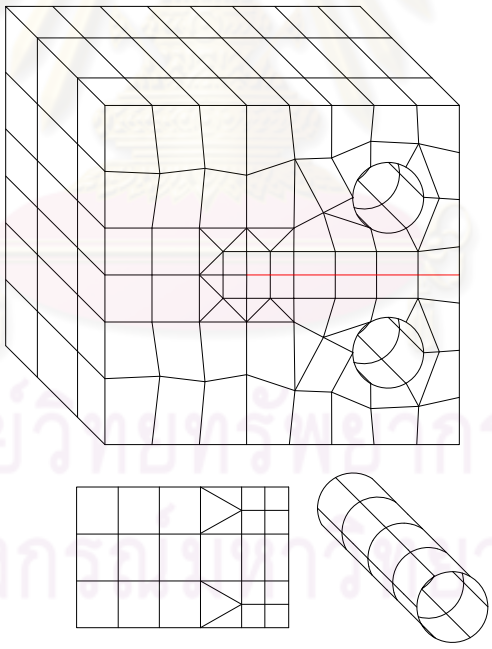

Figure 3.5 Coarse mesh or Mesh-1 for CT specimen thickness $t/a = 1$

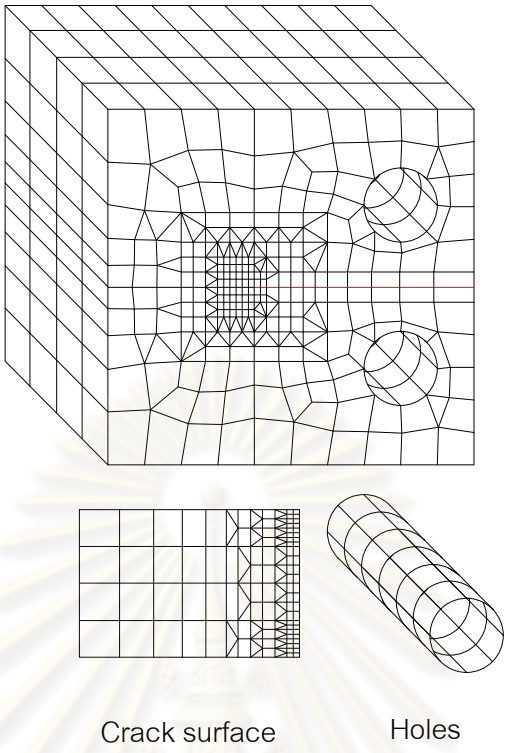

Figure 3.6 Medium mesh or Mesh-2 for CT specimen thickness $t / a = 1$

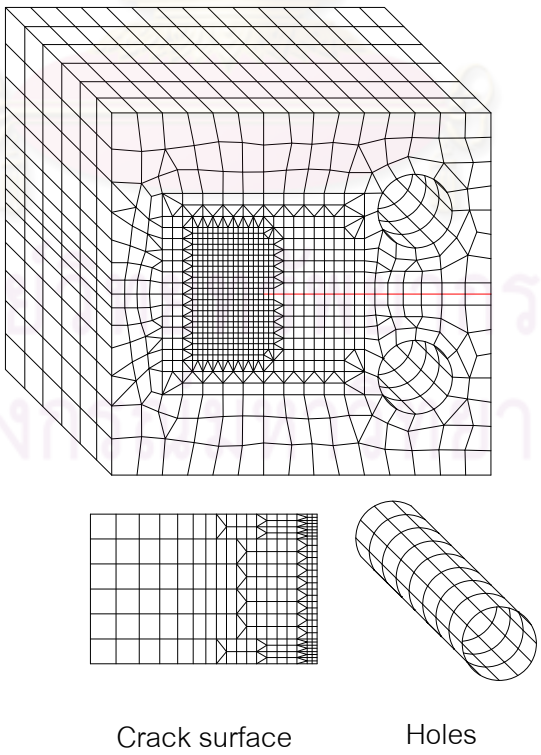

Figure 3.7 Fine mesh or Mesh-3 for CT specimen thickness $t / a = 1$

Table 3.1 Number of nodes and elements for three meshes shown in Figures 3.5-3.7

Mesh	Number of nodes			Number of elements		
	Total	Boundary	Crack	Total	Boundary	Crack
1	927	829	98	324	298	26
2	2892	2425	467	1050	900	150
3	7614	6781	833	2704	2436	268

Table 3.2 Elastic constants (GPa) for zinc and cadmium (e.g. Freund and Suresh, 2003). The axis of material symmetry is taken to direct along the x_3-coordinate direction.

Materials	E_{1111}	E_{1122}	E_{1133}	E_{3333}	E_{1313}
Zinc	161	34.2	50.1	61	38.3
Cadmium	115.8	39.8	40.6	51.4	20.4

Numerical results for the mode-I stress intensity factor along the crack front are reported for three materials and three meshes in Figure 3.8. It is evident that results obtained from the Mesh-2 and Mesh-3 are almost identical while those from the Mesh-1 exhibit slight difference especially very near the vertices where the stress intensity factor drops very rapidly. This should imply the rapid convergence and the weak dependency on the level of mesh refinement for both isotropic and anisotropic cases. Next, we investigate the convergence behavior of numerical results for the same specimen but with the thickness $t/a = 4$. Meshes used in the analysis for this particular case are obtained by simply scaling coordinates in the direction along the thickness of the three meshes shown in Figures 3.5-3.7. Again, results of the mode-I stress intensity

factor (see Figure 3.9) lead to the same conclusion as the previous case and, in particular, stretching meshes in the thickness direction by four times still does not alter the convergence characteristic of the numerical solutions. It is worth noting that approximate solutions of this high quality can be achieved via the use of relatively coarse meshes due mainly to the application of special crack-tip elements along the crack front.

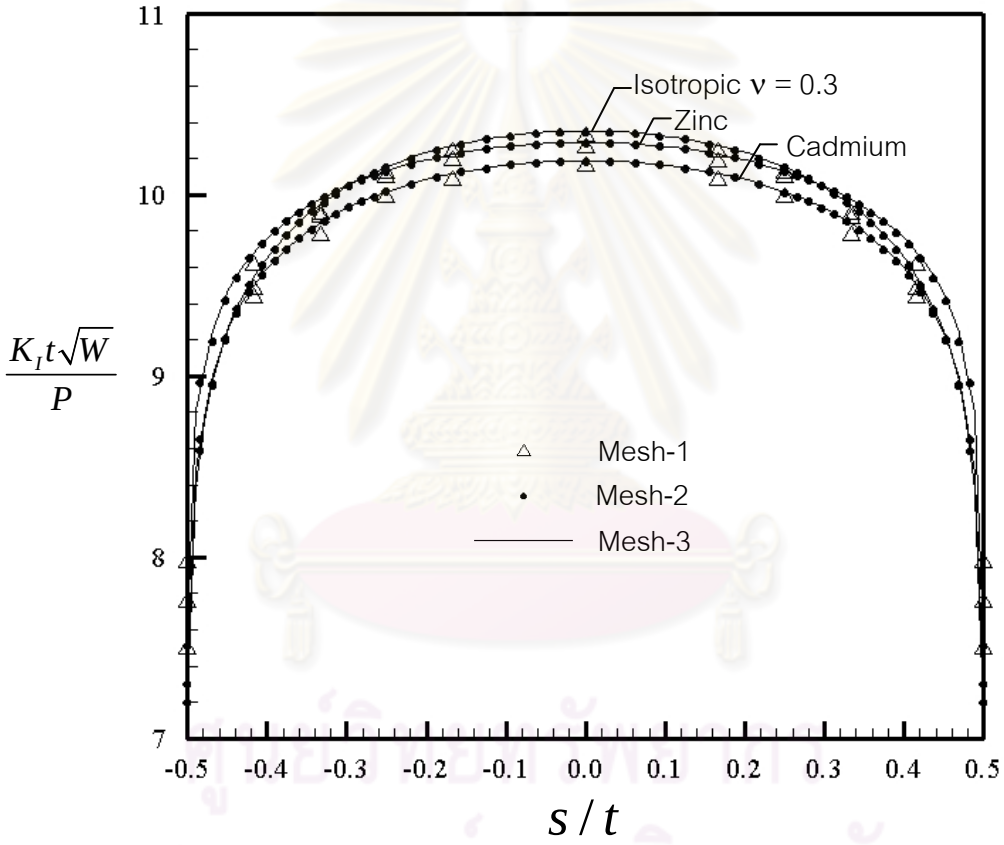

Figure 3.8 Normalized mode-I stress intensity factor along the crack front for CT specimen thickness $t/a=1$. Results are reported for three meshes and three materials and s denotes the distance measured from the center of the crack front.

Since the medium mesh and the fine mesh yields results of comparable accuracy while the latter consumes substantially more computational time, a level of refinement similar to that for the former mesh will be used in the construction of meshes

for a CT specimen of other thicknesses in the parametric study to explore the behavior of the stress intensity factor along the entire crack front.

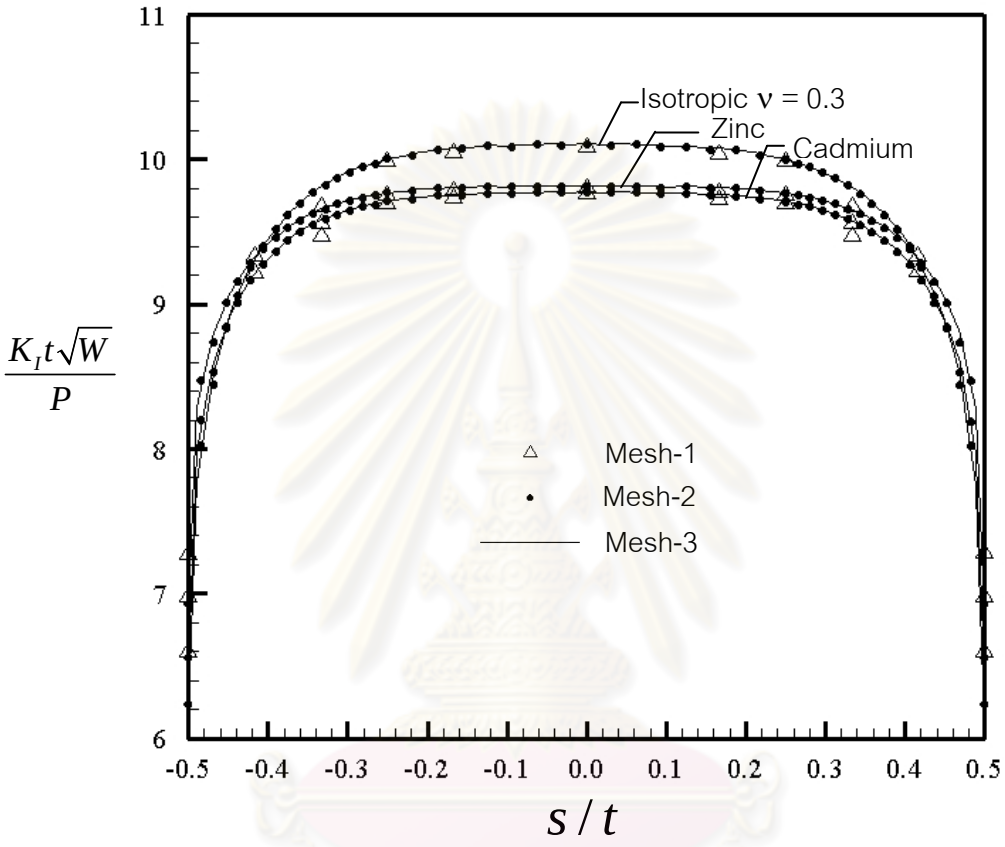

Figure 3.9 Normalized mode-I stress intensity factor along the crack front for CT specimen thickness $t/a = 4$. Results are reported for three meshes and three materials and s denotes the distance measured from the center of the crack front.

3.6 Verification of numerical results

To verify the numerical results obtained from the weakly singular SGBEM, comparisons with existing benchmark solutions for a two-dimensional plane strain case and for isotropic materials are performed. Consider a CT specimen of sufficiently large thickness to ensure the existence of a plane strain condition in the central region of the crack front. Numerical results obtained from a mesh with the same level of refinement as the medium mesh shown in Figure 3.6 are reported along with the plane strain solution proposed by ASTM E399-90 (1997) in Figure 3.10 for Poisson ratio

$\nu = 0.1$ and in Figure 3.11 for Poisson ratio $\nu = 0.3$. It is evident that the SGBEM solutions (in the region exhibiting the plane strain condition) show very good agreement with the benchmark solution. Besides this verification, it should be noted that extensive verification of the weakly singular SGBEM and its formulation used in the present study was already performed by Li *et al*. (1998), Rungamornrat (2006), and Rungamornrat and Mear (2008b) for various crack problems associated with both isotropic and transversely isotropic media.

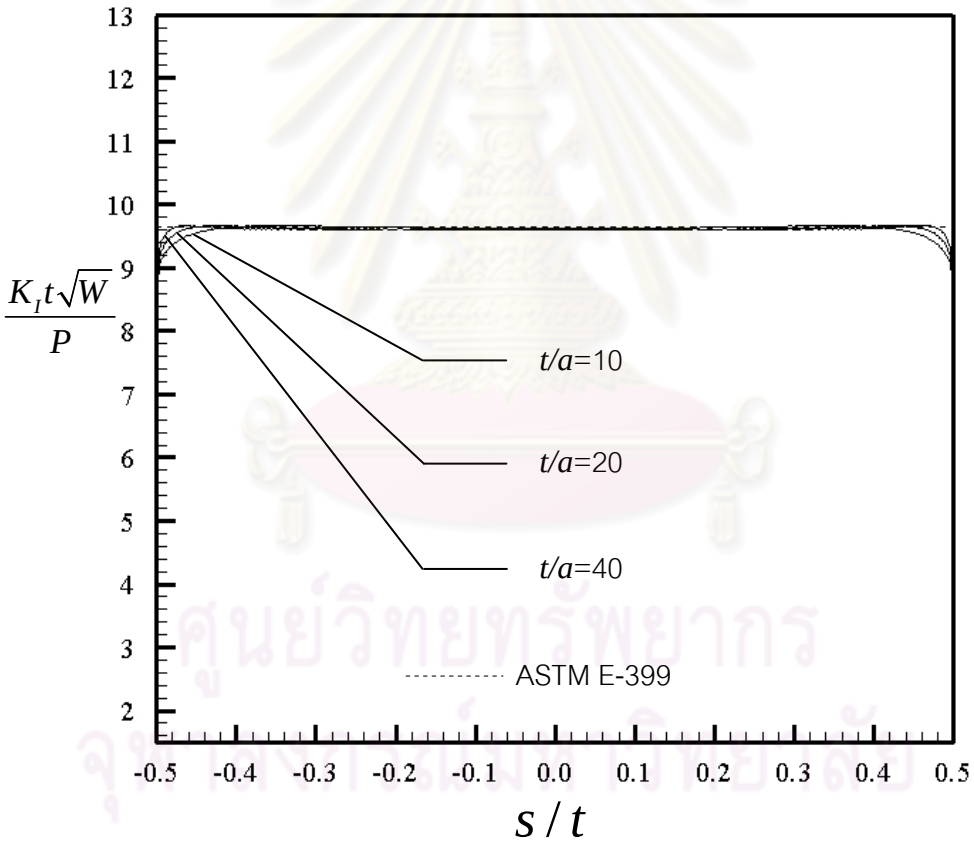

Figure 3.10 Normalized mode-I stress intensity factor along the crack front for CT specimen for sufficiently large thicknesses along with the plane strain solution from ASTM E399-90 (1997). Results are reported for isotropic material with $\nu = 0.1$ and s denotes the distance measured from the center of the crack front.

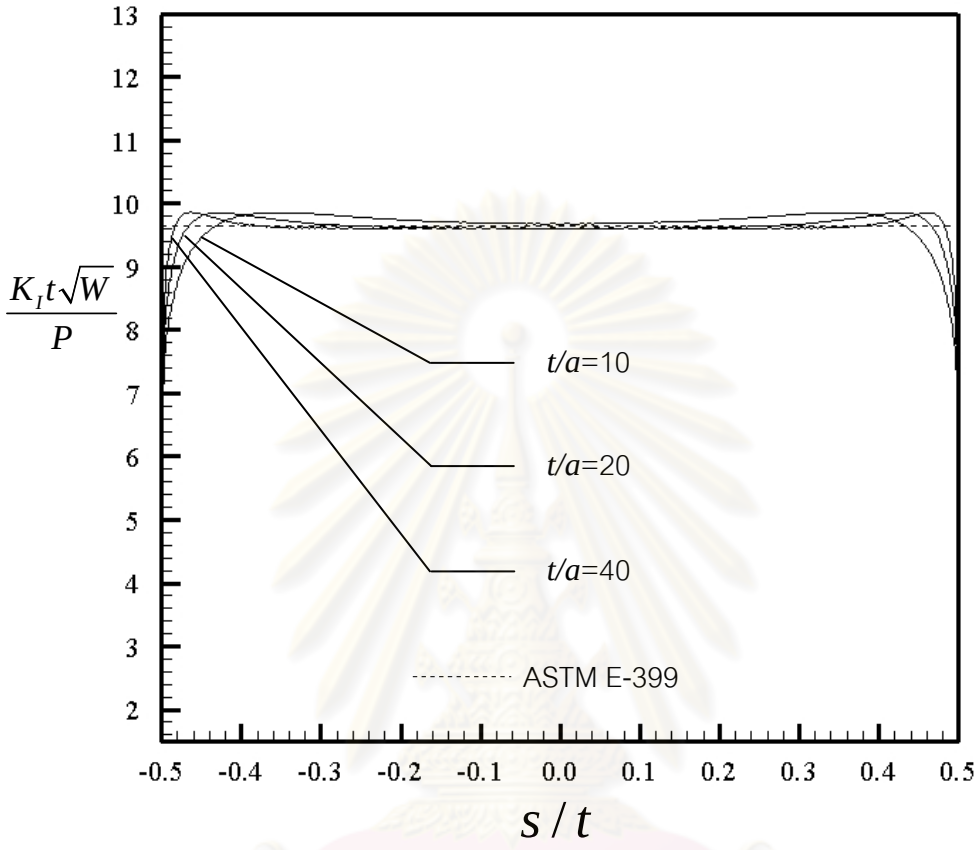

Figure 3.11 Normalized mode-I stress intensity factor along the crack front for CT specimen for sufficiently large thicknesses along with the plane strain solution from ASTM E399-90 (1997). Results are reported for isotropic material with $\nu = 0.3$ and s denotes the distance measured from the center of the crack front.

3.7 Mesh for CT specimen with different thickness

To construct meshes for the CT specimen of various thicknesses, the medium mesh for $t/a = 1$ shown in Figure 3.6 is used as a prototype. Two following simple strategies, (i) mesh stretching along the crack front direction and (ii) adding an inner layer, are employed. The mesh stretching is applied first to obtain a series of meshes for several thicknesses without adding nodes and elements but simply scaling the coordinate along the crack front. However, this strategy can be used up to a certain thickness in order to avoid elements of large aspect ratios and produce too coarse

meshes. For a specimen with too large thickness to use the first strategy, the second strategy is employed instead by adding a layer of elements and nodes in the central region of the crack front. With this particular means, the mesh for the two side-faces does not alter. With the proper combination of these two schemes, a series of meshes can be constructed for the CT specimen of thickness ranging from $t/a = 1$ to $t/a = 40$. Examples of meshes for CT specimen of certain thicknesses are shown in Figures 3.12-3.13.

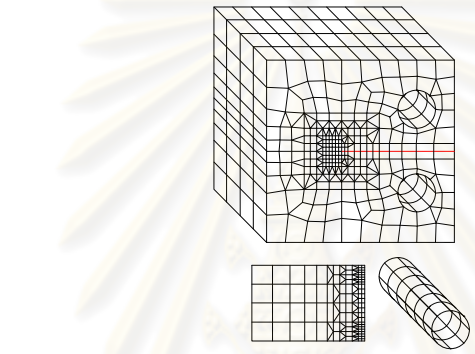

(a)

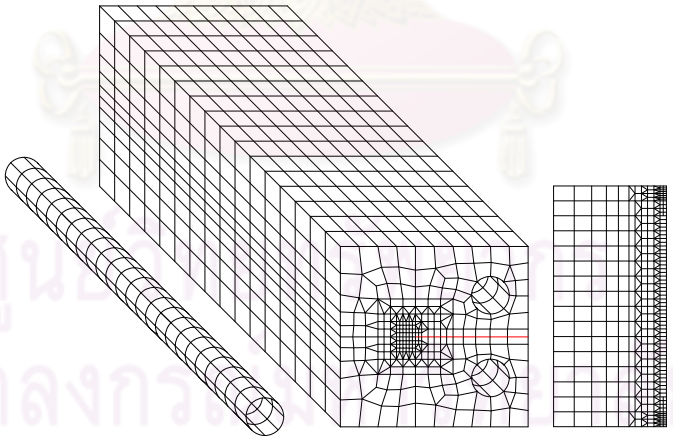

(b)

Figure 3.12 Meshes for CT specimen: (a) $t/a = 1$ and (b) $t/a = 5$

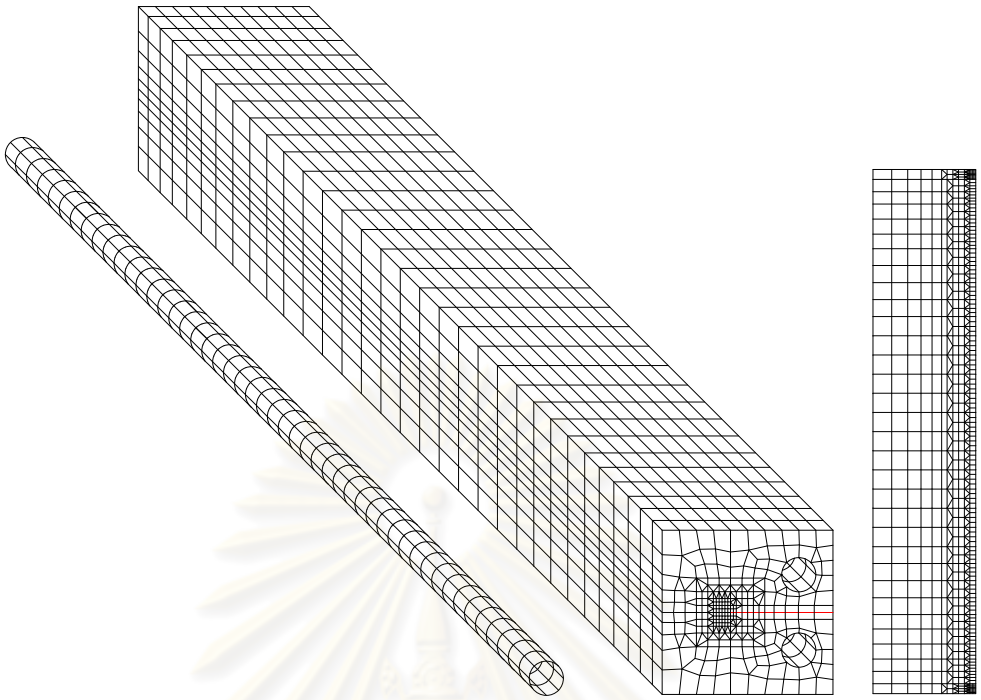

Figure 3.13 Mesh for CT specimen for $t / a = 10$

CHAPTER IV

NUMERICAL RESULTS AND DISCUSSION

In this chapter, results from an extensive parametric study to investigate the influence of the thickness on the distribution of the stress intensity factor along the crack front of the CT specimen are reported and discussed. In the analysis, the specimen thickness is varied from $t/a = 1$ to $t/a = 40$ to ensure that the plane strain condition dominates the majority of the crack front of the specimen with the maximum thickness $t/a = 40$. Two important classes of linear elastic materials, one associated with isotropic materials and the other corresponding to transversely isotropic materials, are examined in the present study. Meshes generated using the strategy described in section 3.4 and section 3.7 are utilized in the analysis for the stress intensity factor.

4.1 Results for isotropic materials

To explore the influence of the specimen thickness and material constants on the behavior of the stress intensity along the crack front for the isotropic case, we perform the analysis for various thicknesses $t/a \in \{1, 2, 3, 4, 5, 10, 20, 40\}$ and several values of Poisson's ratio $\nu \in \{0,\ 0.05,\ 0.10,\ 0.15,\ 0.20,\ 0.25,\ 0.30,\ 0.35,\ 0.40,\ 0.45,\ 0.50\}$ for each thickness. It should be noted that the stress intensity factor exhibits material dependence only on the Poisson's ratio ν not the Young's modulus E. The normalized mode-I stress intensity factors, denoted by $K_I t\sqrt{W}/P$ where P is the total applied load and t and W are the specimen thickness and width, respectively, as indicated in Figure 3.2, is reported as a function of the normalized distance along the crack front, denoted by s/t where s is the distance measured from the center of the crack front, in Figure 4.1 for $\nu = 0$, Figure 4.2 for $\nu = 0.10$, Figure 4.3 for $\nu = 0.30$, and Figure 4.4 for $\nu = 0.50$ (results for other values of Poisson's ratio are shown in Appendix A). For each plot, the plane strain stress intensity factor proposed by ASTM E-399 is also reported to allow the comparison and discussion. From this set of results, following findings are summarized.

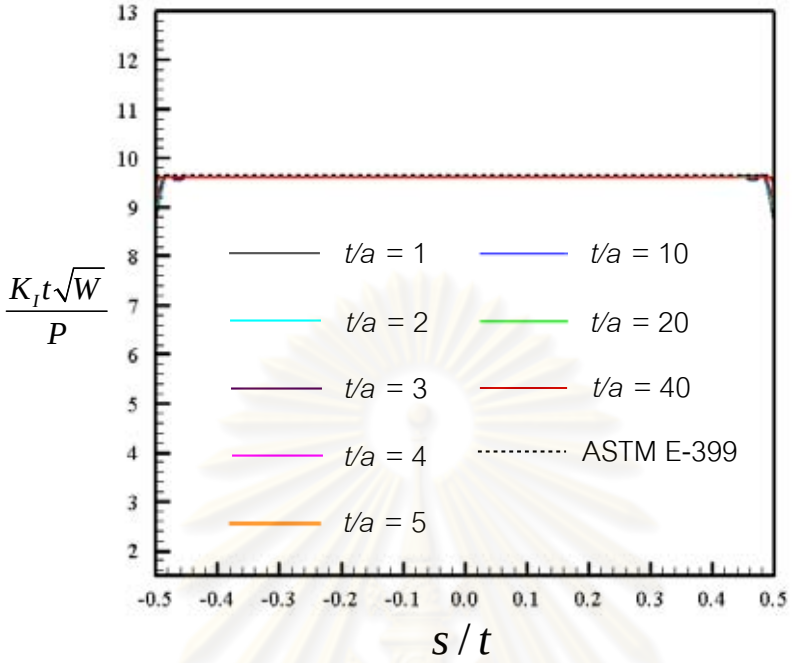

Figure 4.1 Normalized mode-I stress intensity factor versus the normalized distance along the crack front for various thicknesses and ν = 0

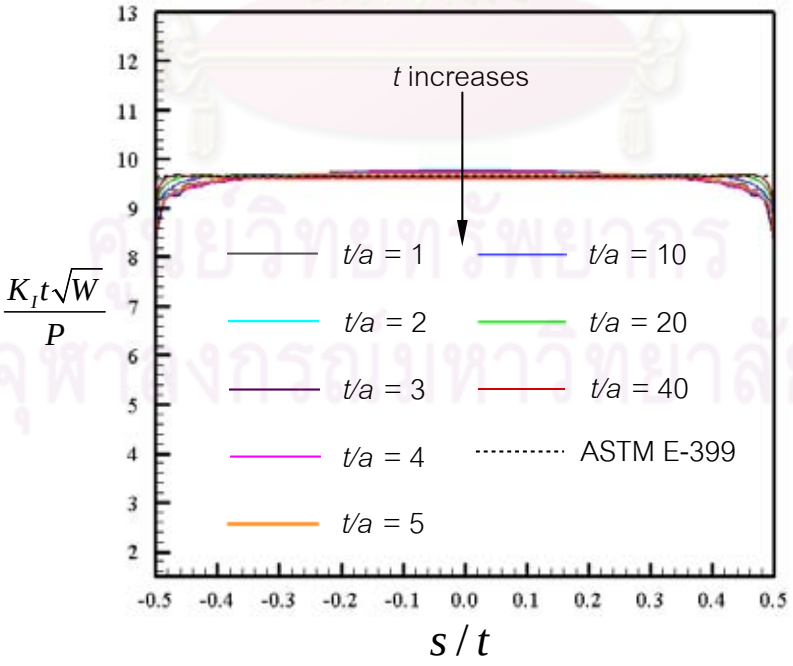

Figure 4.2 Normalized mode-I stress intensity factor versus the normalized distance along the crack front for various thicknesses and ν = 0.1

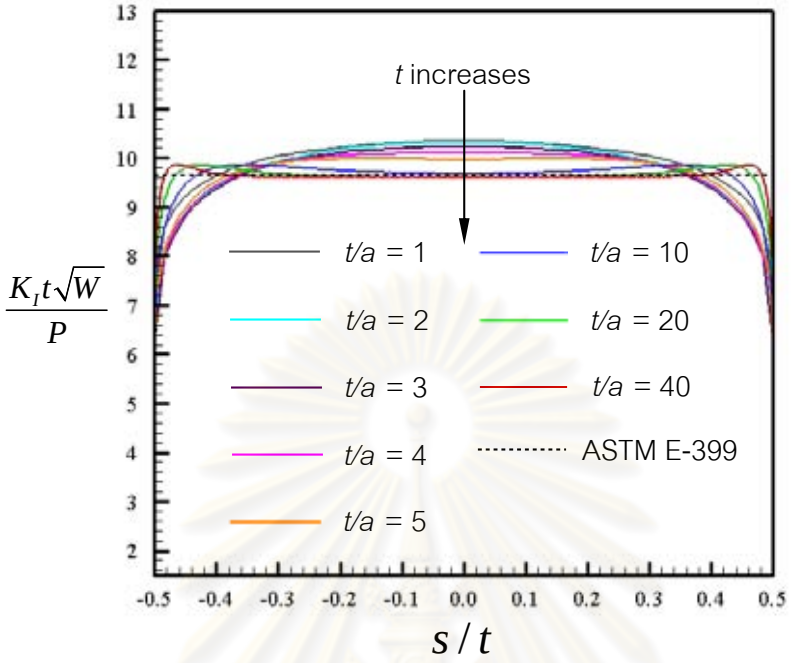

Figure 4.3 Normalized mode-I stress intensity factor versus the normalized distance along the crack front for various thicknesses and ν = 0.3

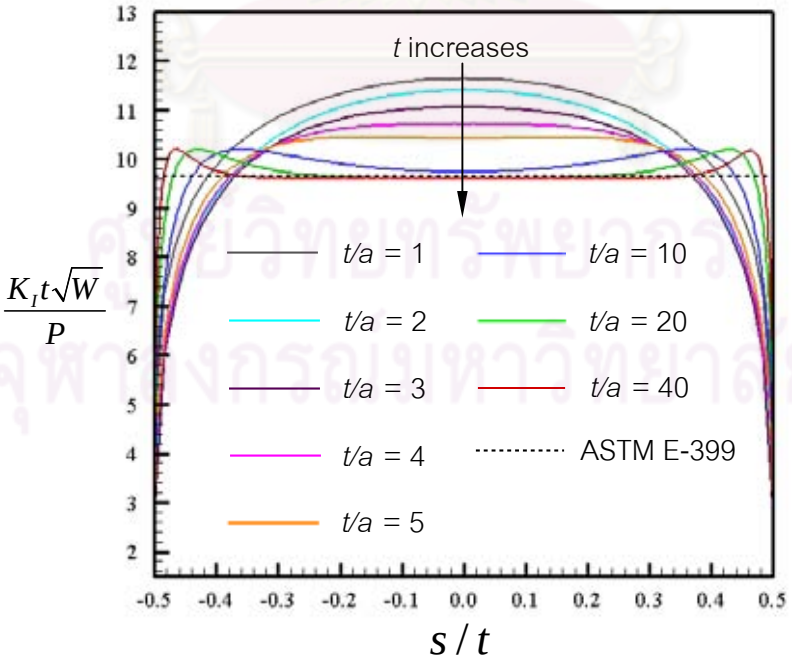

Figure 4.4 Normalized mode-I stress intensity factor versus the normalized distance along the crack front for various thicknesses and ν = 0.5

- For Poisson's ratio $\nu = 0$, the plane strain condition dominates the entire crack front with no regard of the specimen thickness and, in addition, the computed results exhibit excellent agreement with the benchmark solution except in the region close to the surface breaking points. The slightly oscillated behavior of numerical solutions observed in that region is due to the fact that the (reduced-order) special crack-tip element and the adjacent modified boundary element containing the vertices cannot accurately capture the asymptotic field. Note in addition that the stress field at the vertex, for this particular case, is singular of the same order as that for the interior point of the crack front.
- For small Poisson's ratio (i.e. $\nu \le 0.1$), the stress intensity factor varies along the crack front but such variation is still insignificant for all thicknesses considered. The rapid decrease of the stress intensity factor is observed in the neighborhood of the surface breaking point. This implies that the singularity of the stress field at the vertex is of order less than $1/\sqrt{r}$.
- For moderate and large Poisson's ratio (i.e. $\nu \ge 0.2$), the variation of the stress intensity factor across the thick becomes more significant and depends primarily on the specimen thickness. For a specimen with small thickness (i.e. $t/a \le 5$), the stress intensity factor attains its maximum value at the center of the crack front and monotonically decreases to zero at the two vertices. The slight rate of decrease is observed for the majority of the crack front except in a layer near the outer boundary where the rapid drop occurs. In addition, the three-dimensional analysis yields the stress intensity factor higher than the plane strain value for a large portion of the crack front. For a specimen with sufficiently large thickness (i.e. $t/a \ge 10$), the stress intensity factor starts to converge to the plane strain value in the central region

of the crack front and the converged zone spreads towards the vertices as the thickness increases.

- For a specimen with the maximum thickness $t/a = 40$, the plane strain dominated zone covers more than 70% of the crack front for all values of Poisson's ratio treated.

To additionally demonstrate the influence of the Poisson's ratio on both the distribution and magnitude of the stress intensity factor across the thickness, we create different plots between $K_I t\sqrt{W}/P$ and s/t by fixing the specimen thickness but varying the Poisson's ratio. Results are reported in Figure 4.5 for a thinnest specimen ($t/a = 1$), in Figure 4.6 for $t/a = 5$, in Figure 4.7 for $t/a = 10$, and in Figure 4.8 for $t/a = 40$. It can be concluded from these plots that the thickness of a specimen significantly affects the characteristic of the distribution (i.e. shape) of the stress intensity factor along the crack front while the Poisson's ratio only influence its magnitude. More specifically, the larger the Poisson's ratio, the higher the stress intensity factor is observed.

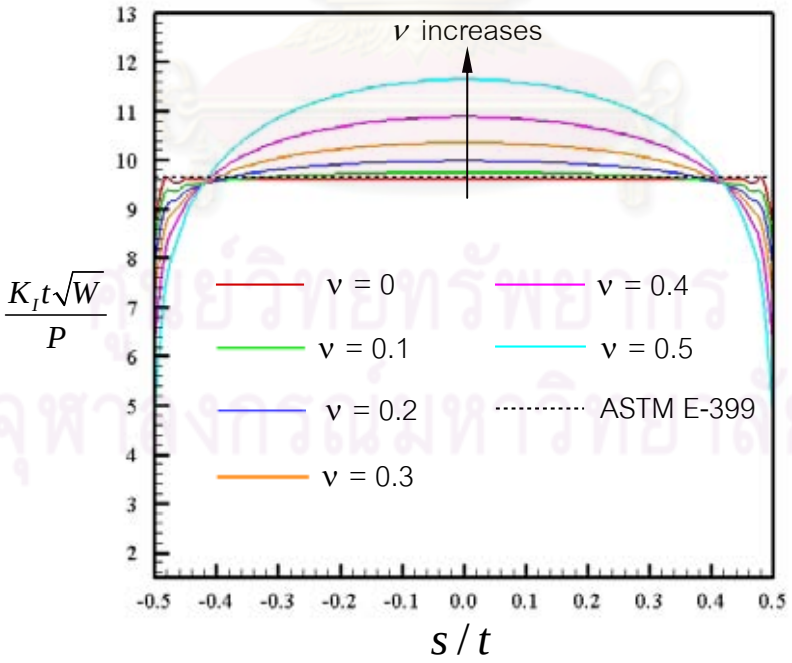

Figure 4.5 Normalized mode-I stress intensity factor versus the normalized distance along the crack front for various Poisson's ratios and $t/a = 1$

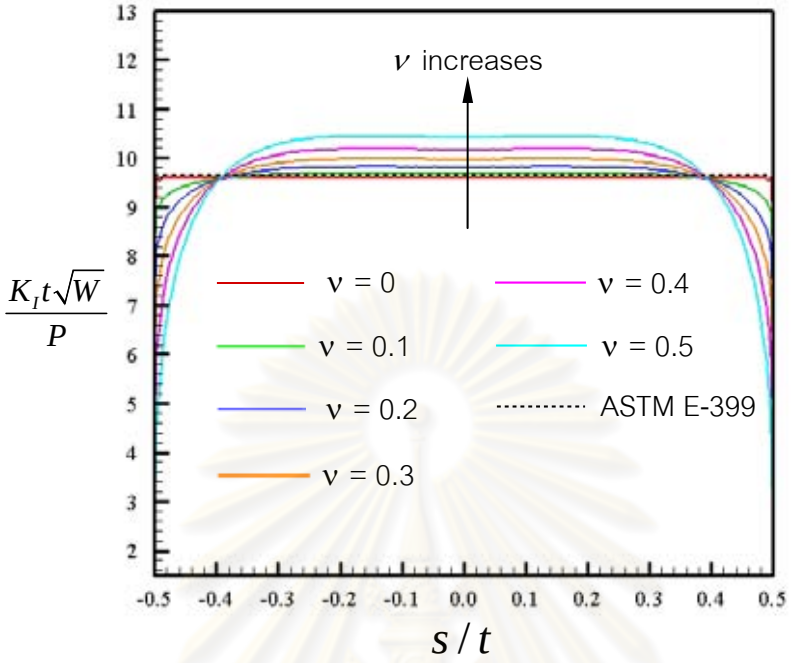

Figure 4.6 Normalized mode-I stress intensity factor versus the normalized distance along the crack front for various Poisson's ratios and $t/a = 5$

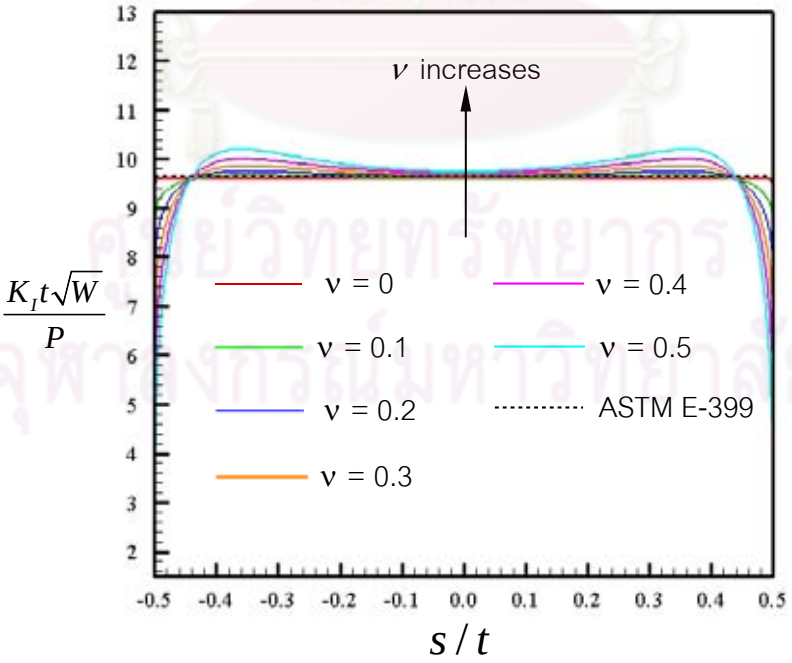

Figure 4.7 Normalized mode-I stress intensity factor versus the normalized distance along the crack front for various Poisson's ratios and $t/a = 10$

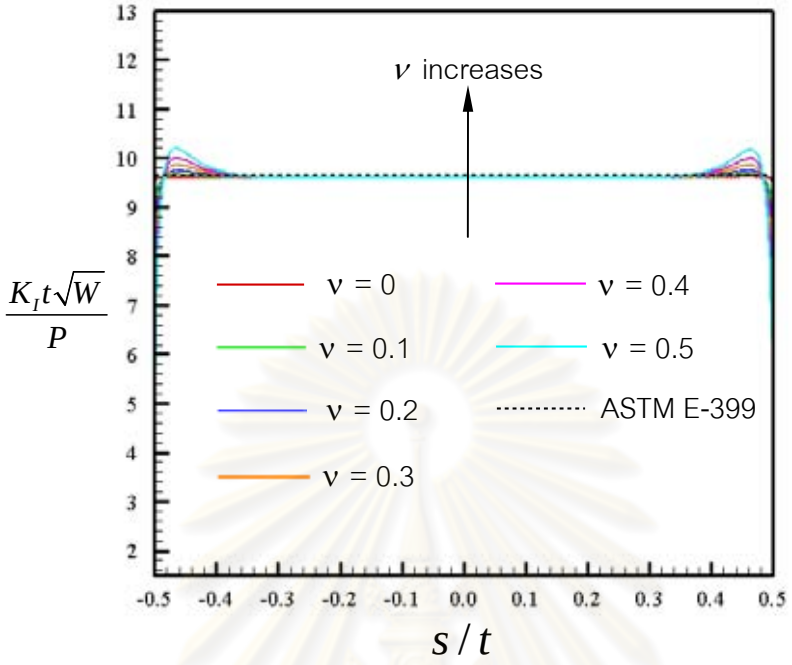

Figure 4.8 Normalized mode-I stress intensity factor versus the normalized distance along the crack front for various Poisson's ratios and $t/a = 40$

Next, we calculate the average of the stress intensity factor over the entire crack front from

$$\overline{K}_I = \int_{-t/2}^{t/2} K_I(s) ds \tag{4.1}$$

where $\overline{K}_I$ denotes the average of the stress intensity factor across the thickness and K_I is the computed stress intensity along the crack front. Although K_I is obtained only at nodes along the crack front, values at all other points can readily be obtained using quadratic interpolation functions (this choice of interpolation functions is not arbitrary but chosen to be consistent with the special crack-tip elements used in the weakly singular SGBEM) as follows:

$$K_I(s) = \frac{(s-s_2)(s-s_3)}{(s_1-s_2)(s_1-s_3)} K_I(s_1) + \frac{(s-s_1)(s-s_3)}{(s_2-s_1)(s_2-s_3)} K_I(s_2) + \frac{(s-s_1)(s-s_2)}{(s_3-s_1)(s_3-s_2)} K_I(s_3)$$

(4.2)

where $K_I(s_1)$, $K_I(s_2)$ and $K_I(s_3)$ are stress intensity factors at nodes along the crack front of the same crack tip element and s_1, s_2, s_3 are distances from the center of the crack front to those three nodes. To demonstrate the influence of the specimen thickness on the existence of the plane strain dominated zone and its size, we plot the average stress intensity factor $\bar{K}_I$, normalized by the plane strain solution K_{PS} (obtained by taking the converged stress intensity factor at the center of the crack front of a specimen with the thickness $t/a = 40$), versus the normalized specimen thickness t/a as shown in Figure 4.9. It is evident that for all Poisson's ratios greater than zero, $\bar{K}_I$ monotonically decreases and asymptotically converges to K_{PS} as the specimen thickness increases. This finding along with results shown in Figures 4.1-4.4 implies that once the plane strain dominated zone exists along the crack front, its size becomes larger as the specimen thickness increases. Furthermore, the rate of convergence to the plane strain solution decreases as the Poisson's ratio increases. This clearly indicates that a specimen made of a material with higher Poisson's ratio requires larger thickness to achieve the same level of plane strain condition along the crack front.

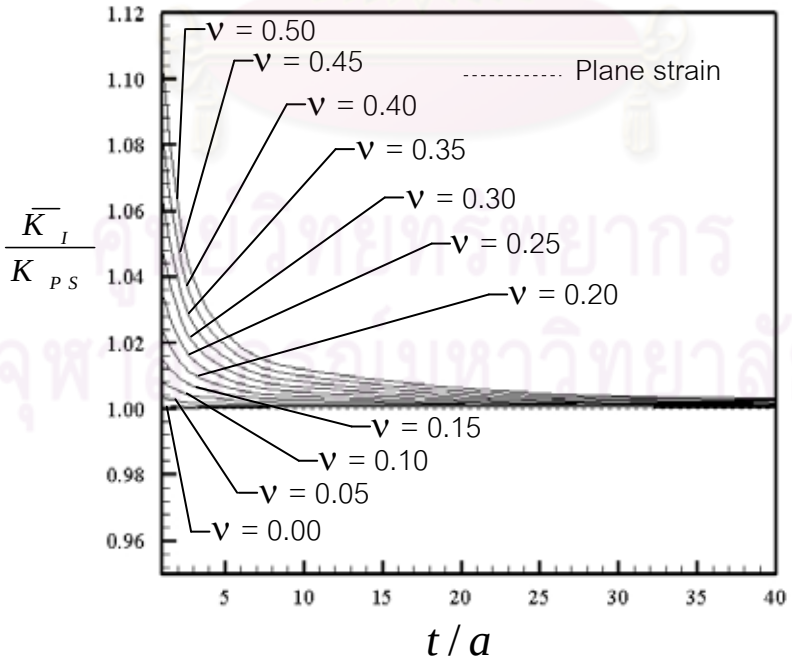

Figure 4.9 Normalized average stress intensity factor versus normalized thickness for various Poisson's ratios

In addition, an empirical relation between the normalized average stress intensity factor $\bar{K}_I / K_{ps}$ and the normalized specimen thickness t/a for any Poisson's ratio can readily be obtained from a standard curve-fitting technique. Based on the data shown in Figure 4.9, a hyperbola function form is suggested in the curve fitting procedure and the final empirical formula is given by

$$\frac{\bar{K}_I}{K_{PS}} = 1 + \frac{0.4008\nu^2 + 0.0591\nu - 0.001}{\frac{t}{a} + 197.05\nu^4 - 298.69\nu^3 + 167.57\nu^2 - 42.76\nu + 4.7006} \tag{4.3}$$

where ν is the Poisson's ratio. Figure 4.10 shows plots between $\bar{K}_I / K_{ps}$ and t/a obtained from the formula (4.3) and from the analysis by the SGBEM. It is evident that the formula (4.3) shows excellent agreement with numerical results for a wide range of the Poisson's ratio and, as a result, can be used confidently to predict the average stress intensity factor for a given specimen thickness and Poisson's ratio.

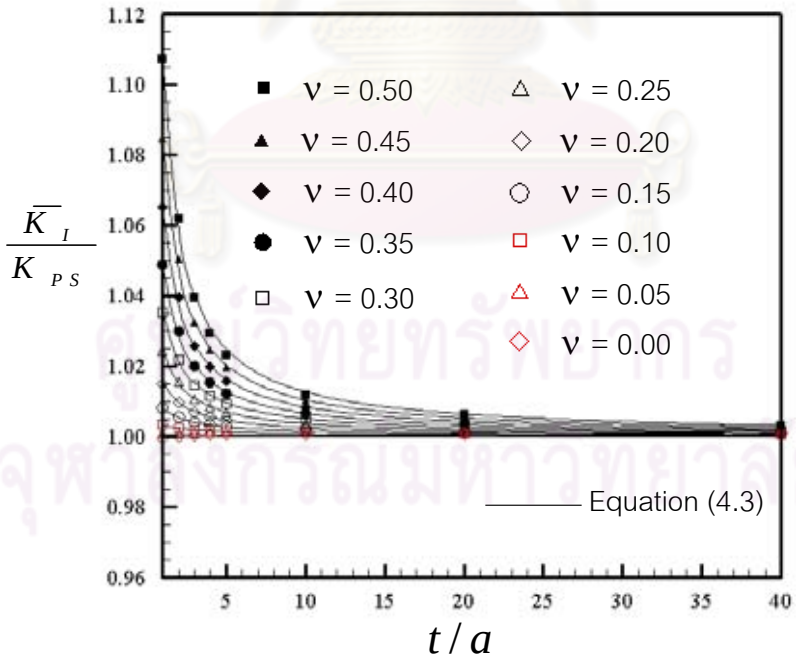

Figure 4.10 Normalized average stress intensity factor versus normalized thickness obtained from equation (4.3) and from analysis data

4.2 Results for transversely isotropic materials

A brief description of a constitutive equation and independent material constants for transversely isotropic materials is given here first to clearly identify some parameters chosen in the parametric study. The six stress components $\{\sigma_{11}, \sigma_{22}, \sigma_{33}, \sigma_{12}, \sigma_{23}, \sigma_{13}\}$ and the six strain components $\{\varepsilon_{11}, \varepsilon_{22}, \varepsilon_{33}, \varepsilon_{12}, \varepsilon_{23}, \varepsilon_{13}\}$ for this particular class of materials (with the axis of material symmetry directing along the X_3-axis and perpendicular to the crack plane) are related by five independent material constants via following two equivalent constitutive equations (e.g. Staab, 1999 and Singh, 2007)

$$\begin{Bmatrix} \sigma_{11} \\ \sigma_{22} \\ \sigma_{33} \\ \sigma_{12} \\ \sigma_{23} \\ \sigma_{13} \end{Bmatrix} = \begin{bmatrix} E_{1111} & E_{1122} & E_{1133} & 0 & 0 & 0 \\ E_{1122} & E_{1111} & E_{1133} & 0 & 0 & 0 \\ E_{1133} & E_{1133} & E_{3333} & 0 & 0 & 0 \\ 0 & 0 & 0 & (E_{1111}-E_{1122}) & 0 & 0 \\ 0 & 0 & 0 & 0 & E_{1313} & 0 \\ 0 & 0 & 0 & 0 & 0 & E_{1313} \end{bmatrix} \begin{Bmatrix} \varepsilon_{11} \\ \varepsilon_{22} \\ \varepsilon_{33} \\ 2\varepsilon_{12} \\ 2\varepsilon_{23} \\ 2\varepsilon_{13} \end{Bmatrix} \tag{4.4}$$

$$\begin{Bmatrix} \varepsilon_{11} \\ \varepsilon_{22} \\ \varepsilon_{33} \\ 2\varepsilon_{12} \\ 2\varepsilon_{23} \\ 2\varepsilon_{13} \end{Bmatrix} = \begin{bmatrix} 1/E_p & -\nu_p/E_p & -\nu_{zp}/E_z & 0 & 0 & 0 \\ -\nu_p/E_p & 1/E_p & -\nu_{zp}/E_z & 0 & 0 & 0 \\ -\nu_{pz}/E_p & -\nu_{pz}/E_p & 1/E_z & 0 & 0 & 0 \\ 0 & 0 & 0 & 2(1+\nu_p)/E_p & 0 & 0 \\ 0 & 0 & 0 & 0 & 1/G_{zp} & 0 \\ 0 & 0 & 0 & 0 & 0 & 1/G_{zp} \end{bmatrix} \begin{Bmatrix} \sigma_{11} \\ \sigma_{22} \\ \sigma_{33} \\ \sigma_{12} \\ \sigma_{23} \\ \sigma_{13} \end{Bmatrix} \tag{4.5}$$

where $E_{1111}, E_{1122}, E_{1133}, E_{3333}$ and E_{1313} are five independent elastic constants; E_p and ν_p are the Young's modulus and Poisson's ratio in the $X_1 - X_2$ symmetry plane; E_z, G_{zp} and ν_{pz} (or ν_{zp}) are the Young's modulus, shear modulus and Poisson's ratio in the X_3 direction; and the two Poisson's ratios are not independent but related through $\nu_{pz}/E_p = \nu_{zp}/E_z$.

In the parametric study, we first investigate the influence of the specimen thickness on behavior of the stress intensity factor along the crack front for two particular transversely isotropic materials (i.e. zinc and cadmium) and then the influence of the

Poisson's ratio ν_p, the modulus ratio E_p / E_z and the modulus ratio G_{zp} / E_p are thoroughly examined.

4.2.1 Results for zinc and cadmium

For this particular case, we perform numerical experiments for various thicknesses $t / a \in \{1, 2, 3, 4, 5, 10, 20, 40\}$ by using the same meshes as those employed in the isotropic case. The elastic constants for zinc and cadmium used in the analysis are given in Table 3.2. The normalized mode-I stress intensity factor ($K_I t\sqrt{W} / P$) are reported as a function of the normalized distance along the crack front (s / t) in Figure 4.11 for zinc and in Figure 4.12 for cadmium. The average stress intensity factor (computed based on equations (4.1) and (4.2)) normalized by the plane strain solution (obtained by taking the converged stress intensity factor at the center of the crack front of a specimen with the thickness $t / a = 40$) is shown in Figure 4.13 as a function of the normalized thickness. From this set of results, it can be concluded that

- The computed stress intensity factors for zinc and cadmium exhibit only slight difference, both in terms of the distribution and magnitude, for all thicknesses considered in the analysis. In addition, the average stress intensity factor for zinc is slightly higher than that for cadmium.
- For thin specimens ($t / a \le 5$), the distribution of the stress intensity factor possesses the same characteristic as that for the isotropic case. For instance, the maximum stress intensity factor still occurs at the center of the crack front and drop rapidly at the region close to the vertices. In addition, the stress intensity factor is higher than the plane strain solution for the majority of the crack front and no plane strain dominated zone is observed in this range of thickness.
- For sufficiently thick specimen ($t / a \ge 10$), the plane strain dominated zone is observed in the central region of the crack front. Similar to the isotropic case, as the specimen thickness increases, this zone expands towards the outer boundary.
- As clearly demonstrated by Figure 4.13, the average stress intensity factor decreases monotonically and asymptotically converges to the plane strain solution as the specimen thickness increases. In

particular, for a specimen with the thickness $t/a \geq 5$, the difference between $\bar{K}_I$ and K_{PS} is less than 2% whereas a specimen with the thickness $t/a \geq 10$, the difference reduce to a fraction of 1%.

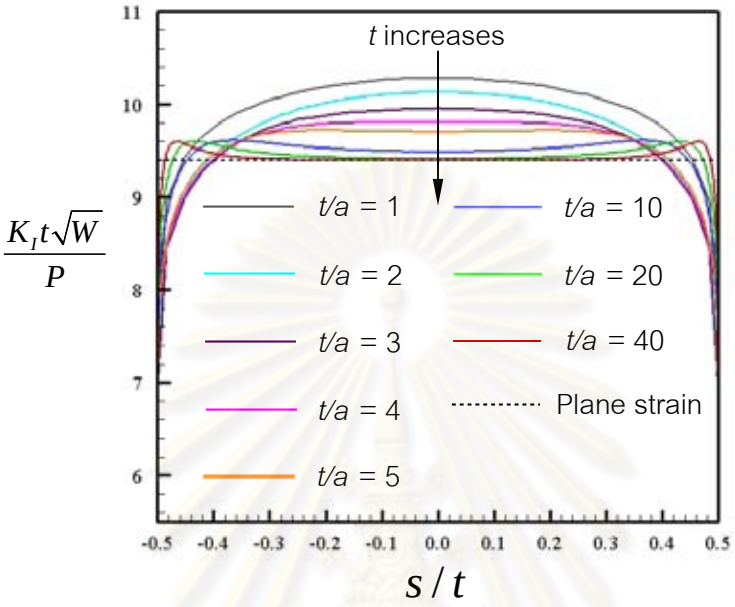

Figure 4.11 Normalized mode-I stress intensity factor versus the normalized distance along the crack front for zinc

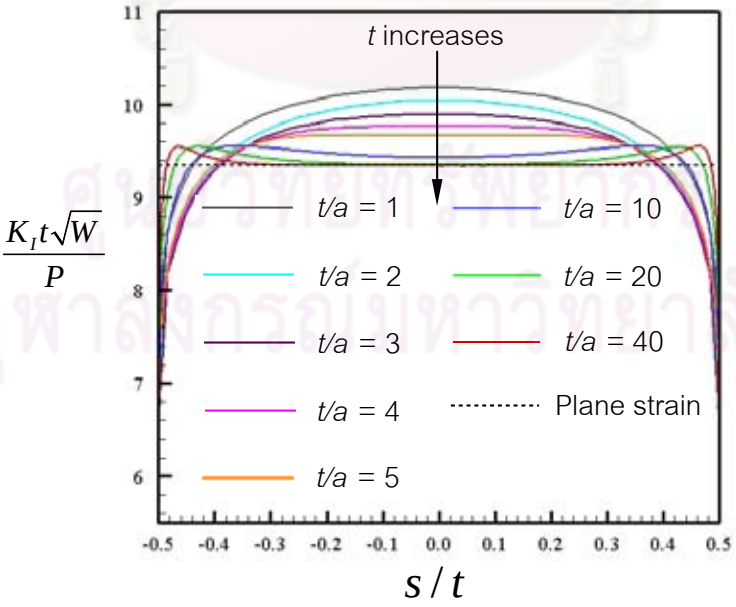

Figure 4.12 Normalized mode-I stress intensity factor versus the normalized distance along the crack front for cadmium

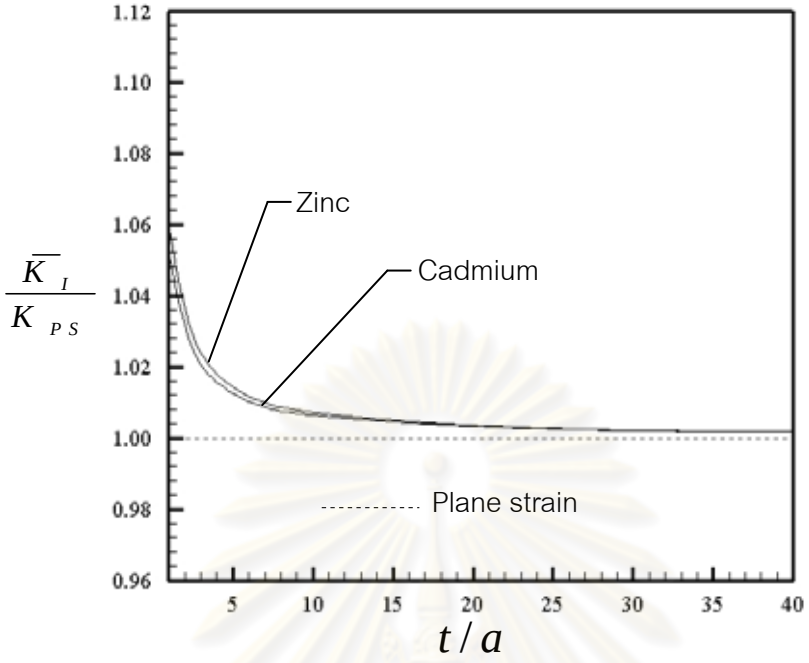

Figure 4.13 Normalized average stress intensity factor versus normalized thickness for zinc and cadmium

4.2.2 Influence of Poisson's ratio ν_p

Next, we investigate the influence of Poisson's ratio ν_p in the $X_1 - X_2$ symmetry plane on the distribution of the stress intensity factor for various thicknesses. In numerical experiments, all other four material constants are fixed except the Poisson's ratio ν_p that is varied over its entire range. The fixed material constants (i.e. E_p, E_z, G_{zp} and ν_{pz} (and ν_{zp})) are taken from those for cadmium as given in Table 4.1. Seven values of Poisson's ratio, i.e. $\nu_p \in \{0.00, 0.10, 0.20, 0.30, 0.40, 0.50, 0.60\}$, are considered and the corresponding elastic constants employed in the SGBEM are shown in Table 4.2.

Table 4.1 Material constants for cadmium used in the investigation of ν_p

Material	E_p (GPa)	E_z (GPa)	G_{zp} (Gpa)	ν_p	ν_{pz}	ν_{zp}
Cadmium	83.0	30.0	20.0	0.10	0.70	0.26

Table 4.2 Elastic constants (GPa) associated with different values of Poisson's ratio (ν_p). The axis of material symmetry is taken to direct along the x_3-coordinate direction.

Materials	E_{1111}	E_{1122}	E_{1133}	E_{3333}	E_{1313}
ν_p=0.00	106.8	23.8	33.9	47.2	20.0
ν_p=0.10	115.2	39.7	40.3	50.4	20.0
ν_p=0.20	129.8	60.6	49.5	55.0	20.0
ν_p=0.30	155.4	91.6	64.2	62.5	20.0
ν_p=0.40	205.5	146.2	91.4	76.3	20.0
ν_p=0.50	332.8	277.5	158.7	110.3	20.0
ν_p=0.60	1178.7	1126.8	599.4	333.3	20.0

Results obtained from this extensive analysis reveal that the distribution of the stress intensity factor along the crack front for both thin and thick specimens possesses the same characteristic as that for zinc and cadmium as clearly demonstrated in Figures 4.14-4.16 for $\nu_p = 0, 0.3, 0.6$ (results for other values of are shown in Appendix B). The Poisson's ratio ν_p only influences the magnitude of the stress intensity factor for a given specimen thickness as indicated in Figures 4.17-4.20 for $t/a = 1, 5, 10, 40$. It is important to point out that results for $\nu_p = 0$ possess totally different behavior from those for the isotropic case with $\nu = 0$. No independence of the specimen thickness is observed for the case of transversely isotropic materials.

The average stress intensity factor $\bar{K}_I$ for different values of ν_p is also reported as a function of the normalized thickness in Figure 4.21. Similar to the isotropic case, obtained results confirmed that as the Poisson's ratio ν_p increases, $\bar{K}_I$ monotonically converges to the plane strain solution with a slower rate. Note in particular that the difference between $\bar{K}_I$ and K_{PS} is less than 2% for a specimen with the thickness $t/a \geq 5$ and less than 1% for a specimen with the thickness $t/a \geq 10$.

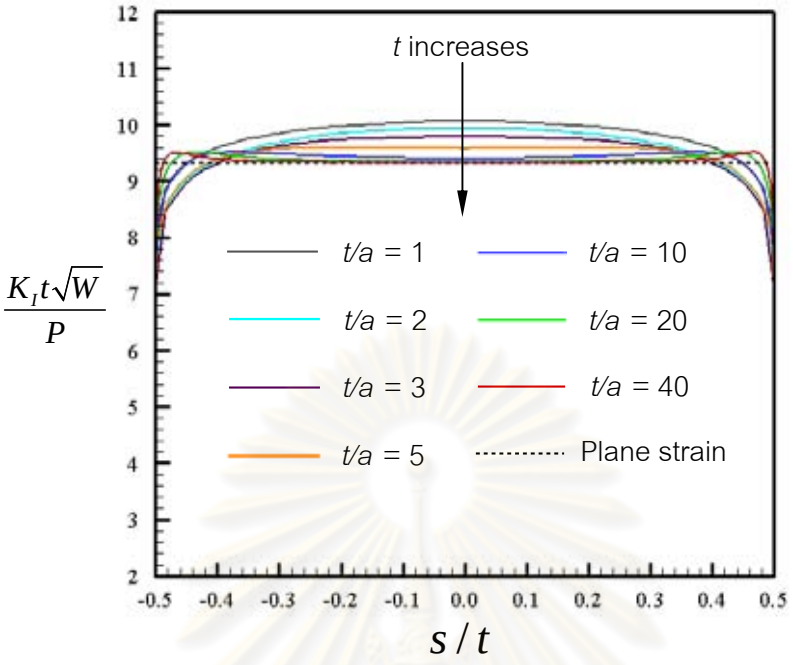

Figure 4.14 Normalized mode-I stress intensity factor versus the normalized distance along the crack front for various thicknesses and ν_p = 0

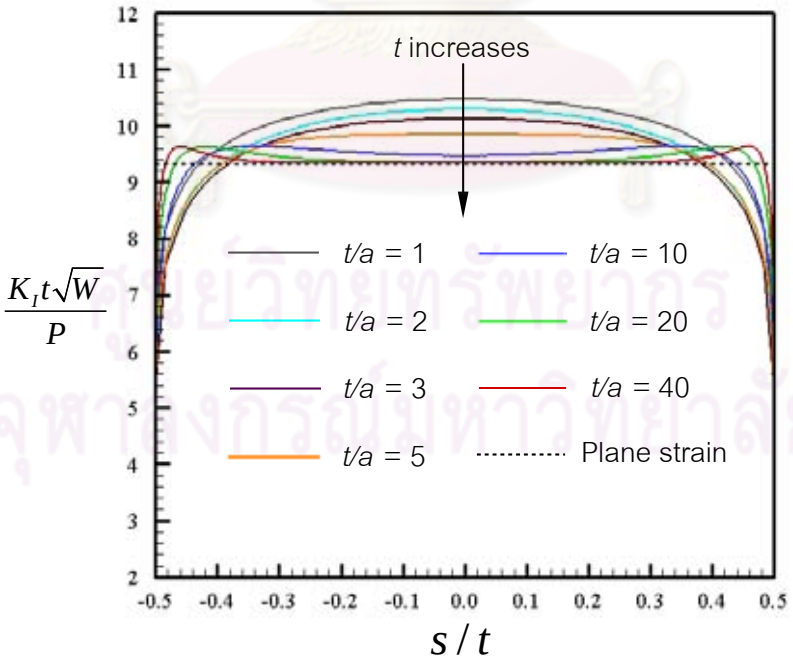

Figure 4.15 Normalized mode-I stress intensity factor versus the normalized distance along the crack front for various thicknesses and ν_p = 0.3

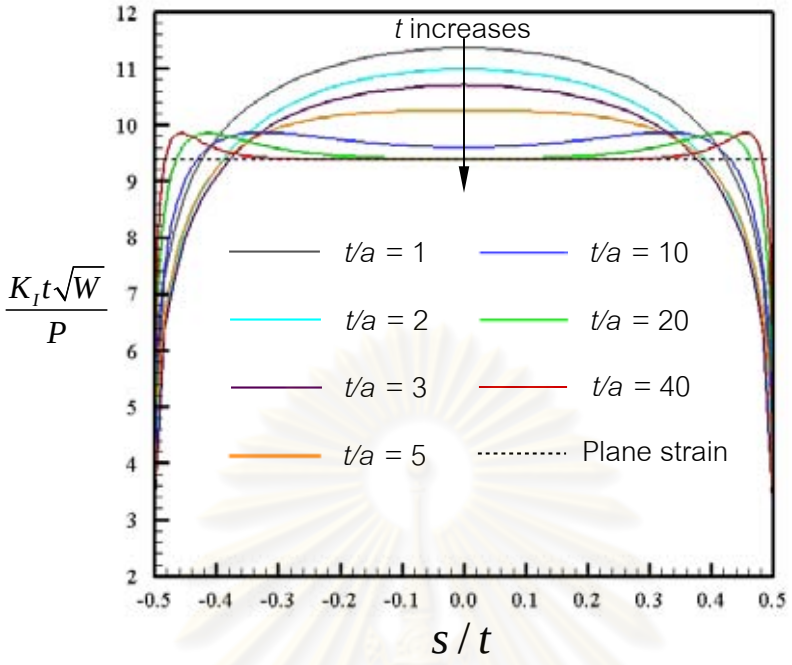

Figure 4.16 Normalized mode-I stress intensity factor versus the normalized distance along the crack front for various thicknesses and ν_p = 0.6

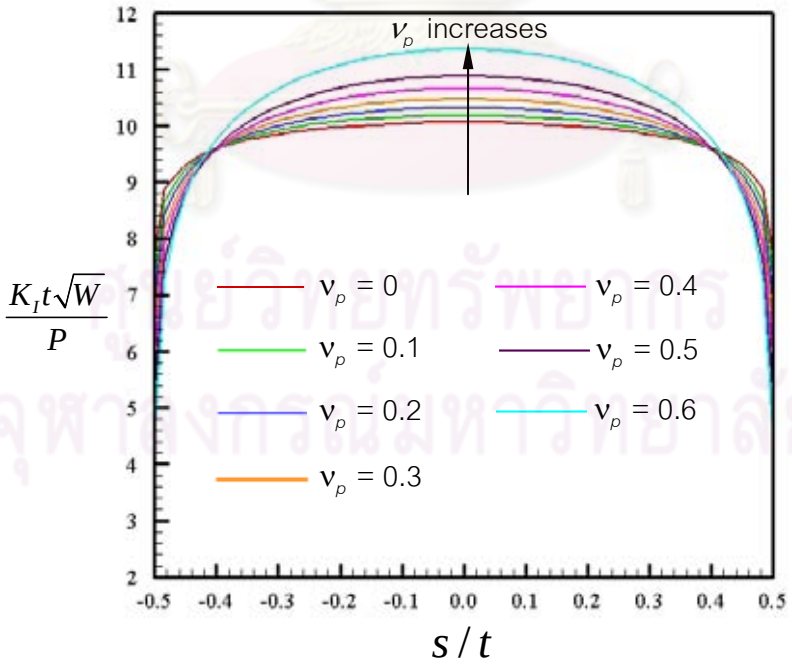

Figure 4.17 Normalized mode-I stress intensity factor versus the normalized distance along the crack front for various Poisson's ratios and $t/a = 1$

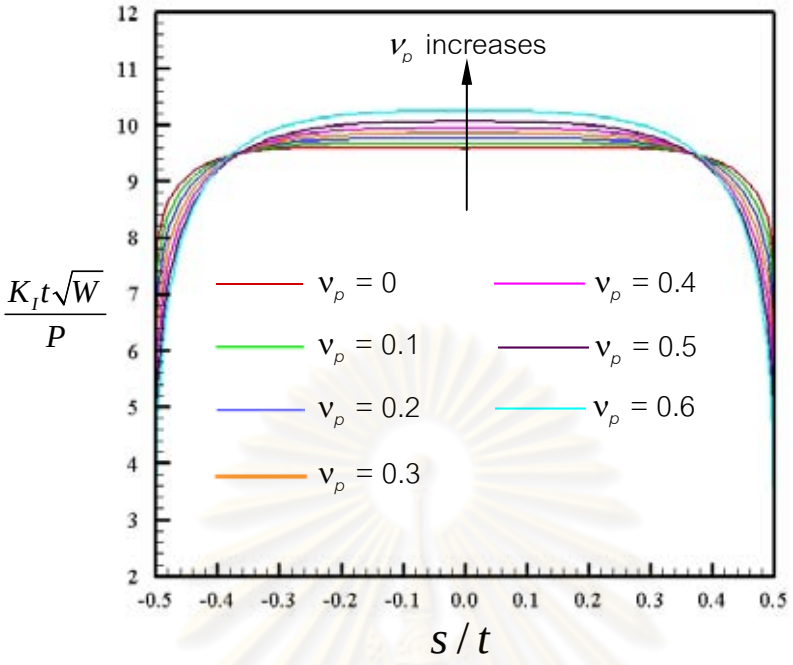

Figure 4.18 Normalized mode-I stress intensity factor versus the normalized distance along the crack front for various Poisson's ratios and $t/a = 5$

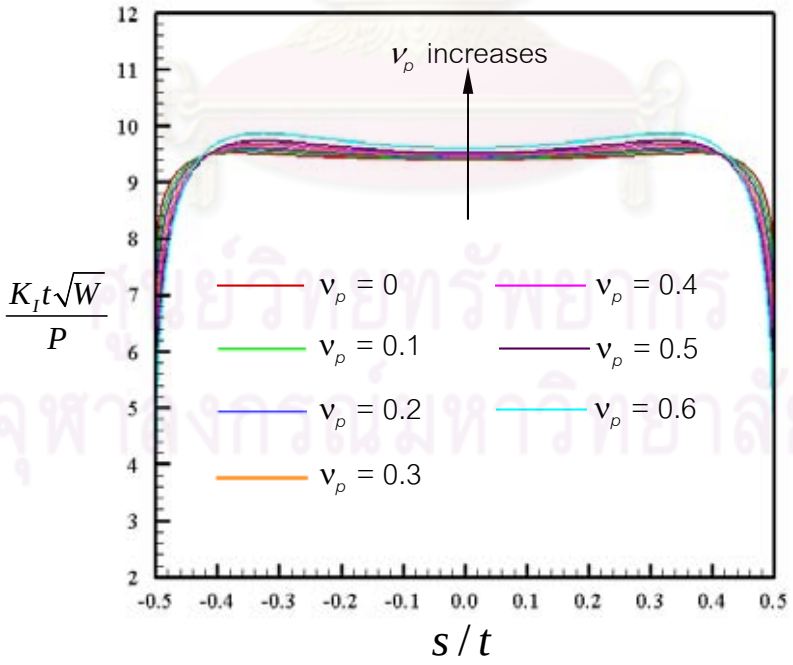

Figure 4.19 Normalized mode-I stress intensity factor versus the normalized distance along the crack front for various Poisson's ratios and $t/a = 10$

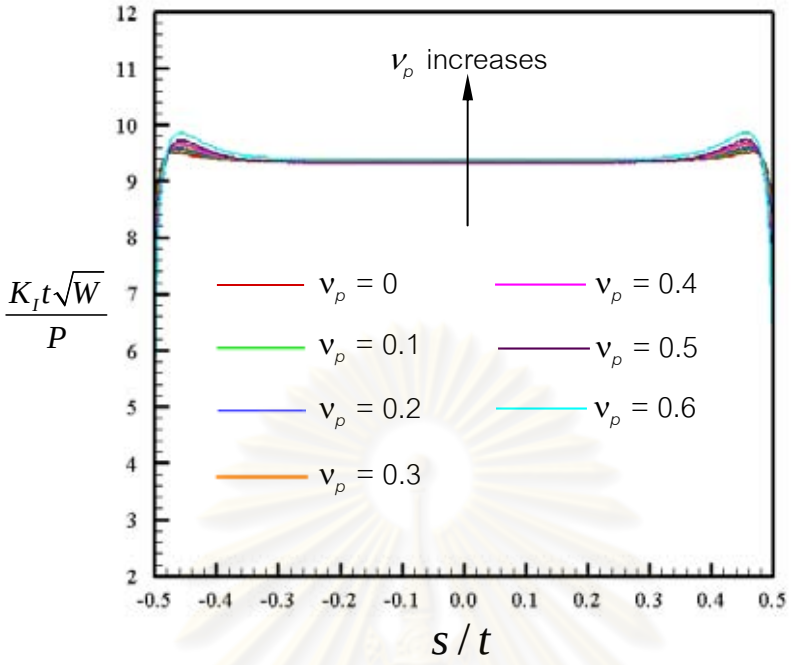

Figure 4.20 Normalized mode-I stress intensity factor versus the normalized distance along the crack front for various Poisson's ratios and $t/a = 40$

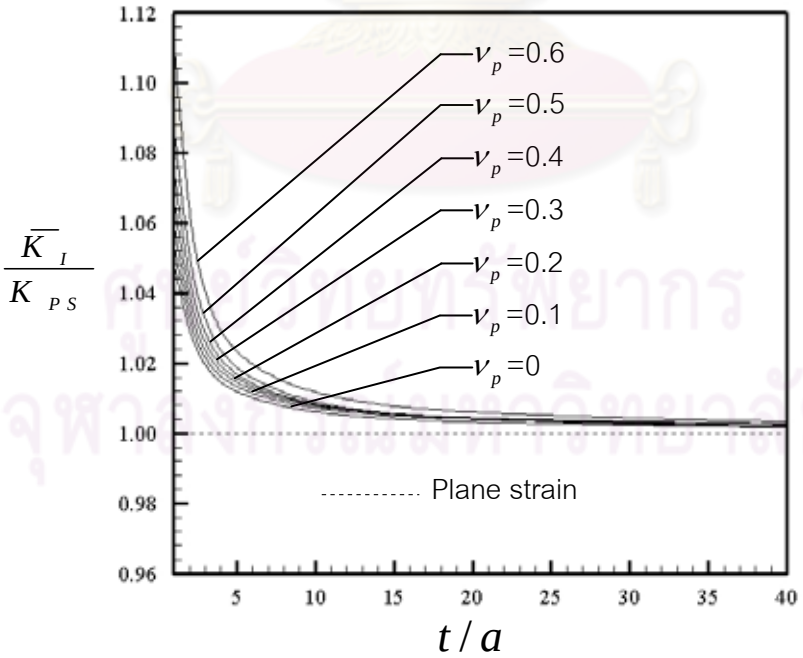

Figure 4.21 Normalized average stress intensity factor versus normalized thickness for different values of ν_p

4.2.3 Influence of modulus ratio E_p / E_z

Next, the influence of the modulus ratio E_p / E_z is investigated. In the analysis, five modulus ratios $E_p / E_z \in \{0.25, 0.5, 1, 2, 3\}$ are considered while other elastic constants remaining fixed. Again, those fixed material constants are taken from cadmium as shown in Table 4.1. Elastic constants associated with each modulus ratio employed in SGBEM are given in Table 4.3. It is important to emphasize that the value of ν_{pz} can readily be computed from the relation $\nu_{pz} = \nu_{zp}(E_p / E_z)$.

The normalized mode-I stress intensity factor is reported along the crack front for various thickness $t/a \in \{1, 2, 3, 5, 10, 20, 40\}$ in Figures 4.22-4.26 for $E_p / E_z \in \{0.25, 0.5, 1, 2, 3\}$, respectively. The plots between the normalized stress intensity and the normalized distance along the crack front for various modulus ratio $E_p / E_z \in \{0.25, 0.5, 1, 2, 3\}$ are also shown in Figures 4.27-4.30 for $t/a = 1, 5, 10, 40$, respectively. The modulus ratio E_p / E_z only slightly influences the distribution of the stress intensity factor along the crack front but significantly affects its magnitude. In addition, as the ratio E_p / E_z increases, the stress intensity factor tends to decreases.

The average stress intensity factor along the crack front is also reported for different values of E_p / E_z in Figure 4.31. It is obvious that the average stress intensity factor exhibits strong dependence on the modulus ratio and, in particular, as E_p / E_z increases, $\bar{K}_I$ increases and it requires larger specimen thickness in order to achieve the same value of $\bar{K}_I$.

Table 4.3 Elastic constants (GPa) associated with different values of modulus ratio E_p / E_z. The axis of material symmetry is taken to direct along x_3-coordinate direction.

Materials	E_{1111}	E_{1122}	E_{1133}	E_{3333}	E_{1313}
$E_p = 0.25E_z$	7.7	0.9	2.3	31.2	20.0
$E_p = 0.50E_z$	15.8	2.2	4.7	32.4	20.0
$E_p = E_z$	33.2	6.0	10.2	35.3	20.0
$E_p = 2E_z$	74.9	20.4	24.8	42.9	20.0
$E_p = 3E_z$	131.9	50.1	47.3	54.6	20.0

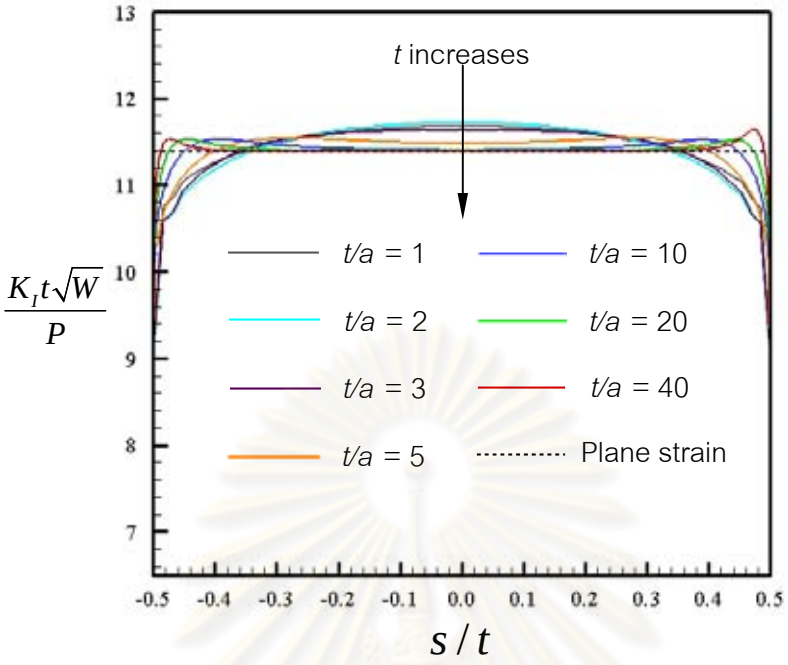

Figure 4.22 Normalized mode-I stress intensity factor versus the normalized distance along the crack front for various thicknesses and E_p / E_z = 0.25

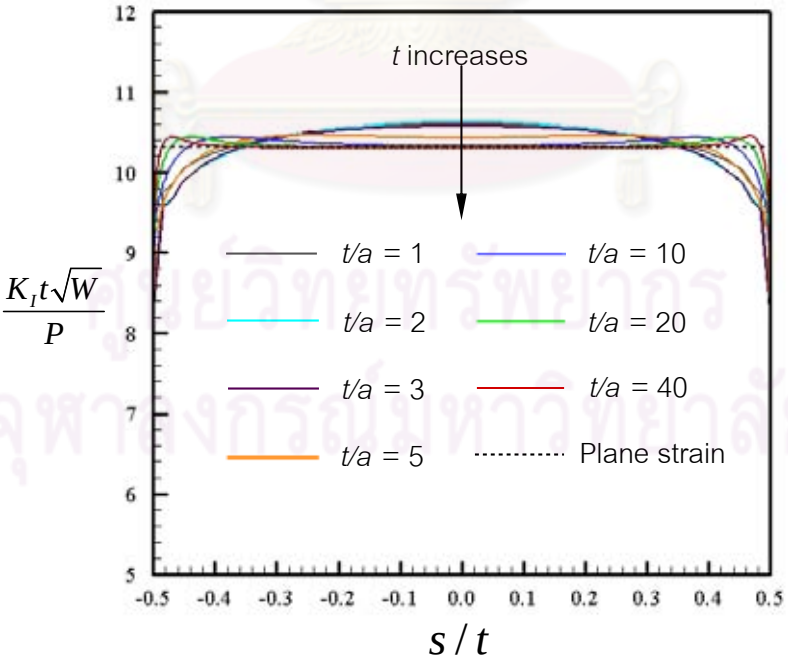

Figure 4.23 Normalized mode-I stress intensity factor versus the normalized distance along the crack front for various thicknesses and E_p / E_z = 0. 5

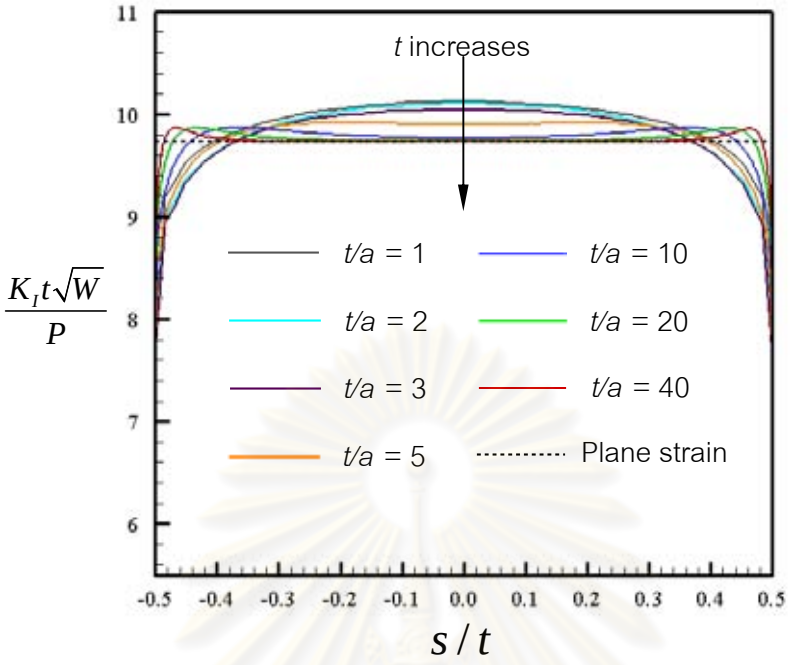

Figure 4.24 Normalized mode-I stress intensity factor versus the normalized distance along the crack front for various thicknesses and $E_p / E_z = 1$

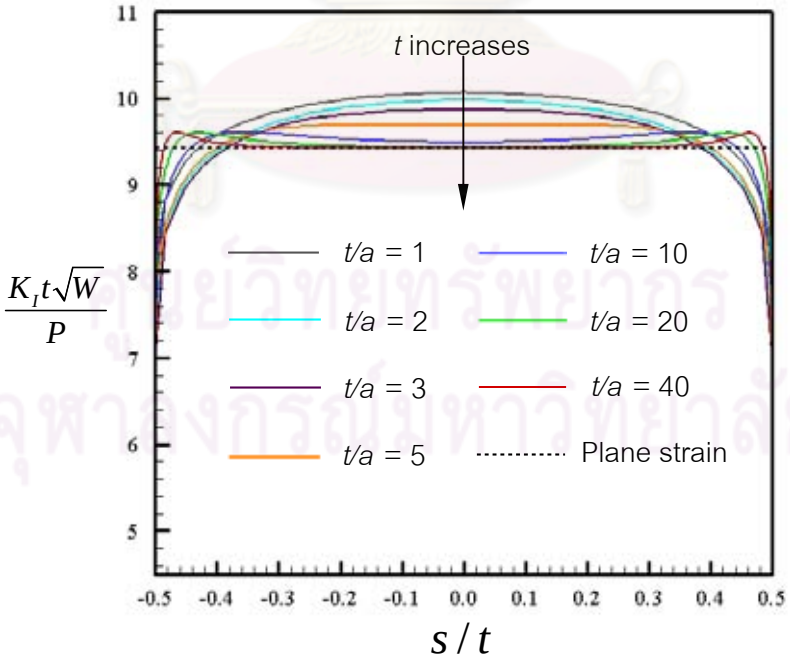

Figure 4.25 Normalized mode-I stress intensity factor versus the normalized distance along the crack front for various thicknesses and $E_p / E_z = 2$

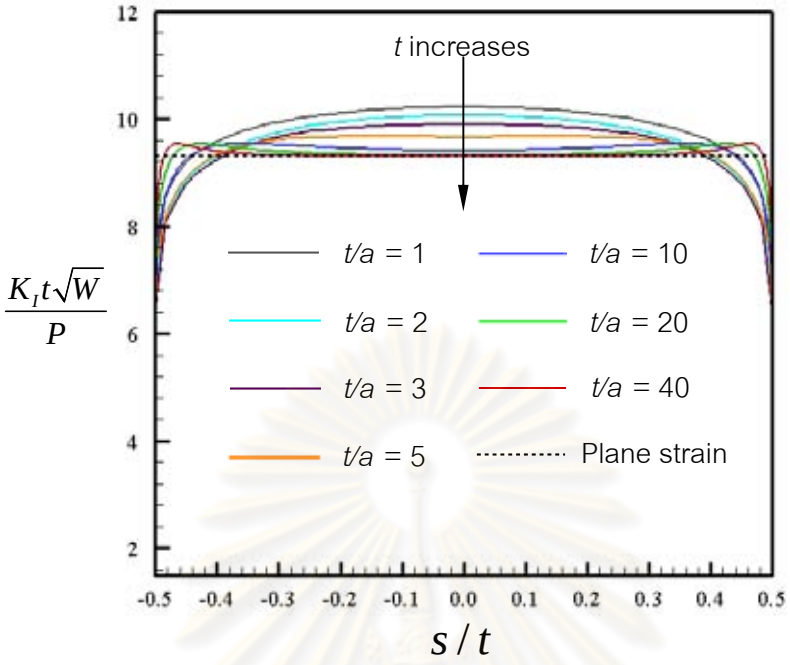

Figure 4.26 Normalized mode-I stress intensity factor versus the normalized distance along the crack front for various thicknesses and E_p / E_z = 3

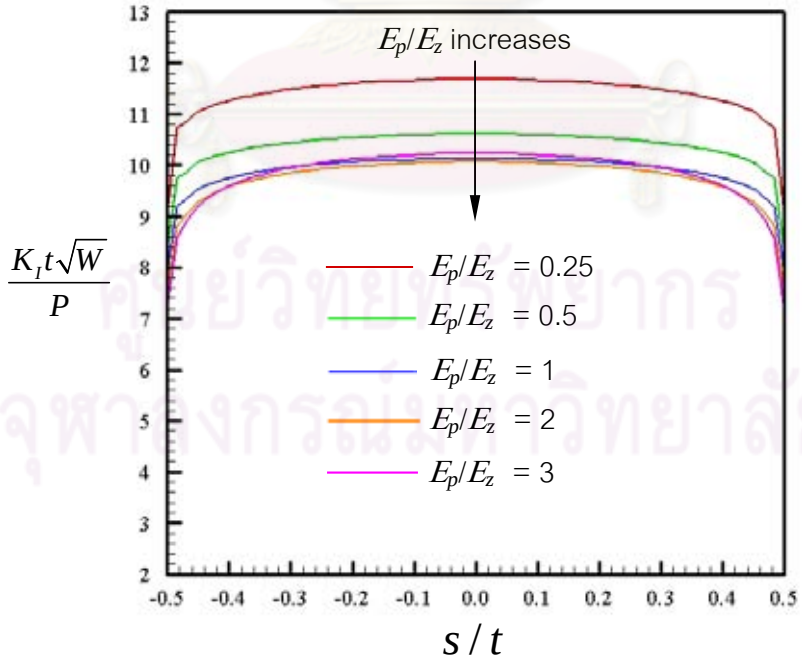

Figure 4.27 Normalized mode-I stress intensity factor versus the normalized distance along the crack front for various modulus ratios E_p / E_z and $t / a = 1$

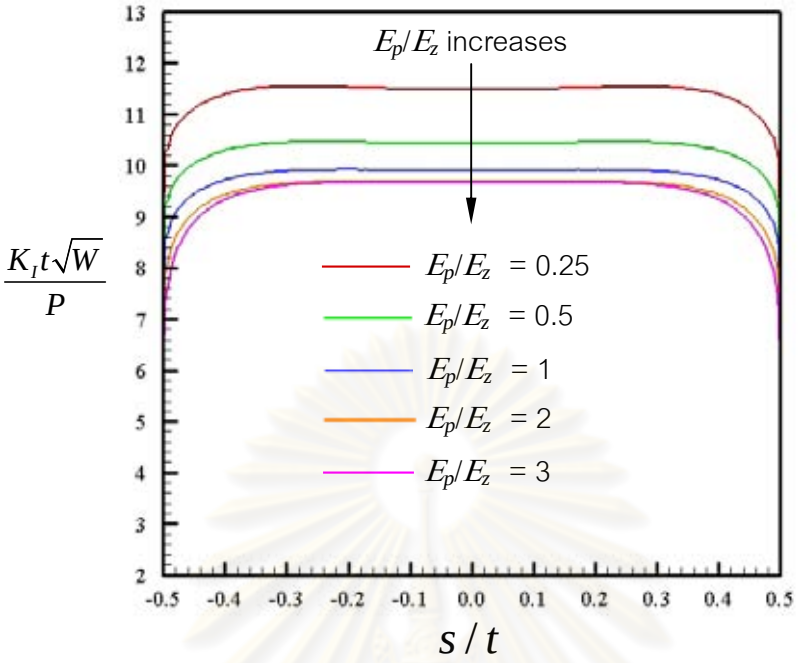

Figure 4.28 Normalized mode-I stress intensity factor versus the normalized distance along the crack front for various modulus ratios E_p/E_z and $t/a=5$

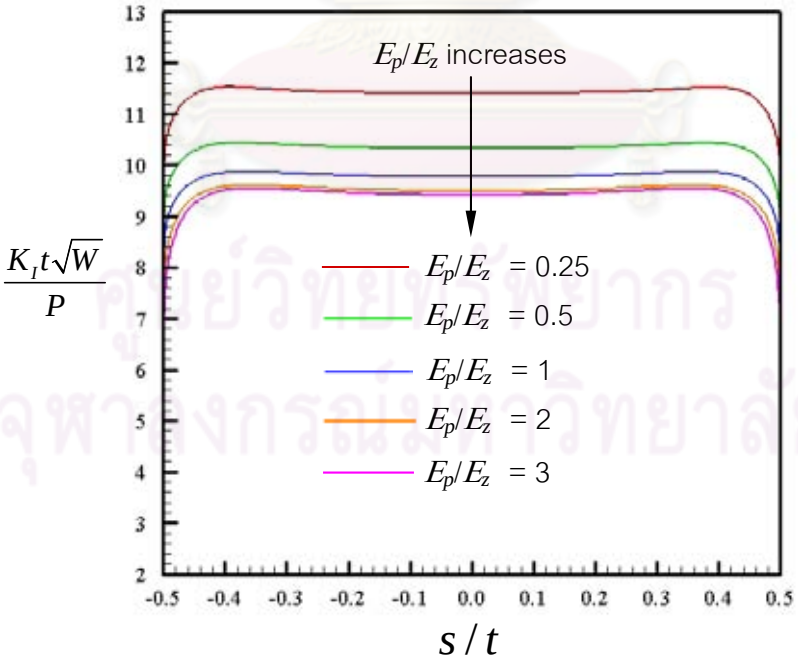

Figure 4.29 Normalized mode-I stress intensity factor versus the normalized distance along the crack front for various modulus ratios E_p/E_z and $t/a=10$

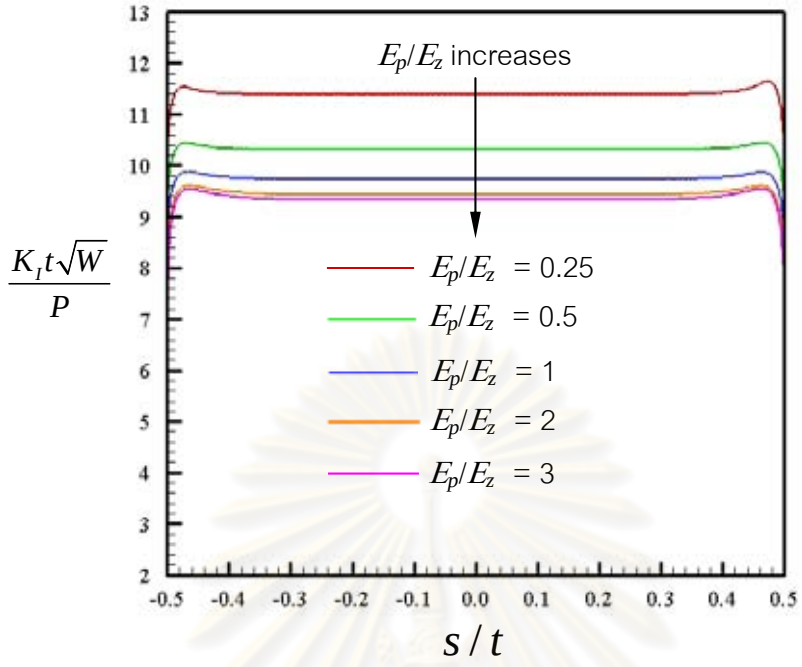

Figure 4.30 Normalized mode-I stress intensity factor versus the normalized distance along the crack front for various modulus ratios E_p / E_z and $t/a = 40$

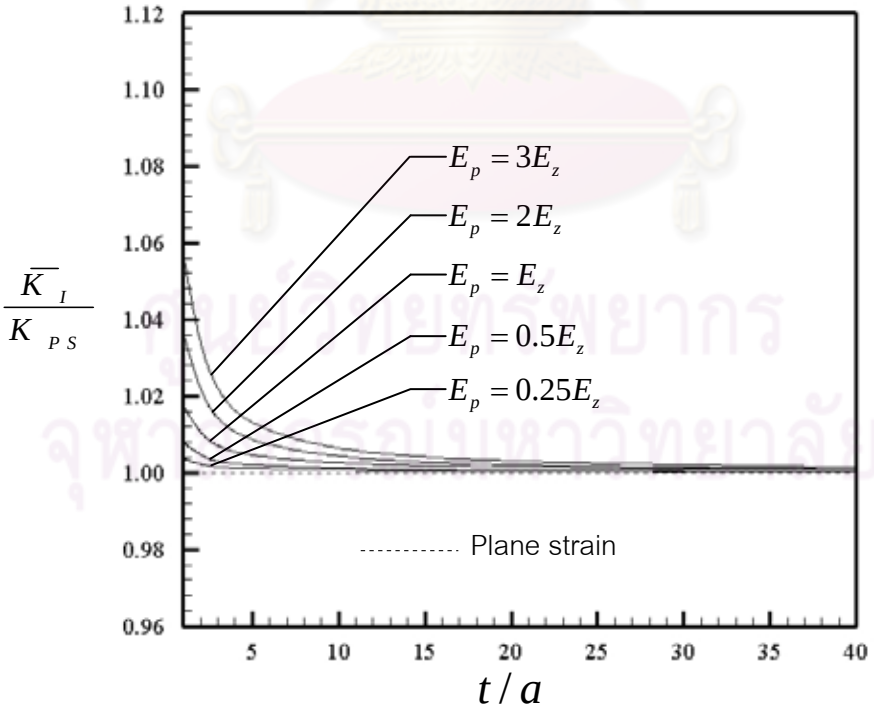

Figure 4.31 Normalized average stress intensity factor versus normalized thickness for different values of E_p / E_z

4.2.4 Influence of modulus ratio G_{zp}/E_p

Finally, we explore the influence of the modulus ratio G_{zp}/E_p. In the analysis, four values of the modulus ratio $G_{zp}/E_p \in \{0.25, 0.5, 1, 2\}$ are considered while other elastic constants remaining fixed. Again, those fixed material constants are taken from cadmium as given in Table 4.1. Elastic constants associated with each value of the modulus ratio employed in analysis by the SGBEM are given in Table 4.4. It is important to emphasize again that the value of ν_{pz} can readily be computed from the relation $\nu_{pz} = \nu_{zp}(E_p/E_z)$.

The normalized mode-I stress intensity factor is reported along the crack front for various thickness $t/a \in \{1, 2, 3, 5, 10, 20, 40\}$ in Figures 4.32-4.35 for $G_{zp}/E_p \in \{0.25, 0.5, 1, 2\}$, respectively. The plots between the normalized stress intensity and the normalized distance along the crack front for various modulus ratio $G_{zp}/E_p \in \{0.25, 0.5, 1, 2\}$ are also shown in Figures 4.36-4.39 for $t/a = 1, 5, 10, 40$, respectively. From these obtained results, similar behavior to the case of Poisson's ratio ν_p and modulus ratio E_p/E_z (e.g. the variation of the stress intensity near the vertex, the existence of the plane strain dominated zone in the central region of the crack front) is deduced when the thickness of the specimen increases. In addition, the modulus ratio G_{zp}/E_p only slightly influences the distribution of the stress intensity factor along the crack front but strongly affects its magnitude. The stress intensity factor tends to increases as the modulus ratio G_{zp}/E_p increases.

The average stress intensity factor along the crack front is also reported for different values of G_{zp}/E_p in Figure 4.40. It is obvious from this set of results that the average stress intensity factor exhibits only slightly dependence on the modulus ratio G_{zp}/E_p and it decays monotonically to the plane strain value as the specimen thickness increases.

Table 4.4 Elastic constants (GPa) associated with different values of modulus ratio G_{zp}/E_p. The axis of material symmetry is taken to direct along the x_3-coordinate direction.

Materials	E_{1111}	E_{1122}	E_{1133}	E_{3333}	E_{1313}
$G_{zp}=0.25E_p$	116.6	41.2	41.0	51.3	20.8
$G_{zp}=0.50E_p$	116.6	41.2	41.0	51.3	41.5
$G_{zp}=E_p$	116.6	41.2	41.0	51.3	83.0
$G_{zp}=2E_p$	116.6	41.2	41.0	51.3	166.0

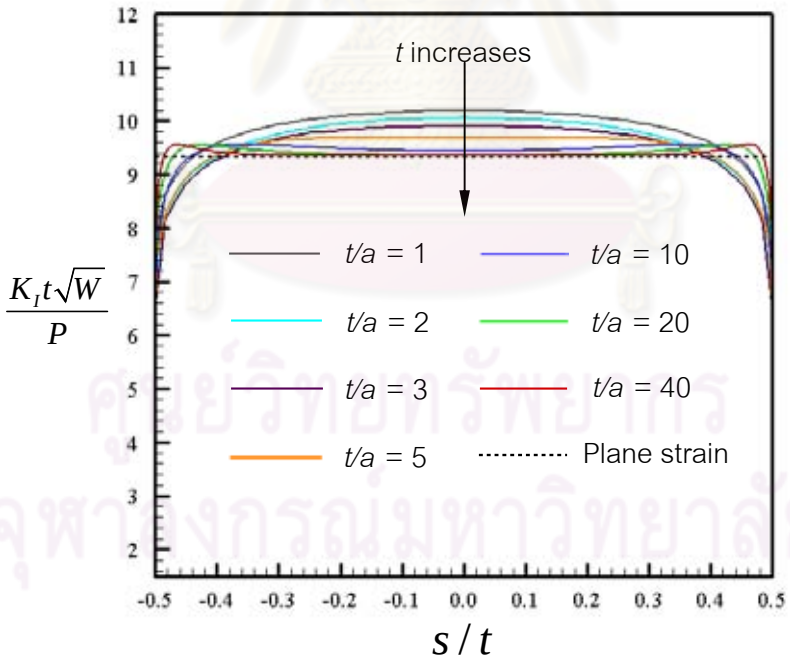

Figure 4.32 Normalized mode-I stress intensity factor versus the normalized distance along the crack front for various thicknesses and G_{zp}/E_p = 0.25

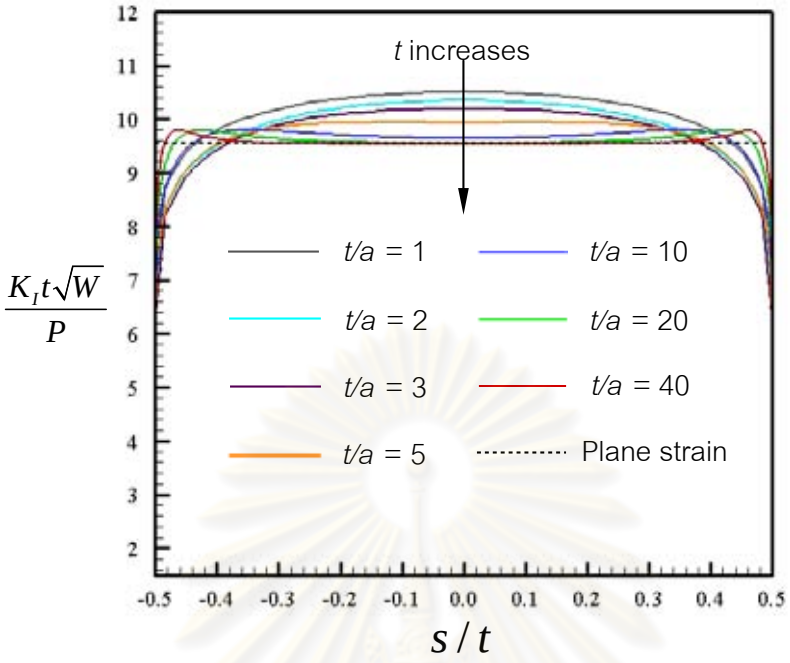

Figure 4.33 Normalized mode-I stress intensity factor versus the normalized distance along the crack front for various thicknesses and G_{zp} / E_p = 0.5

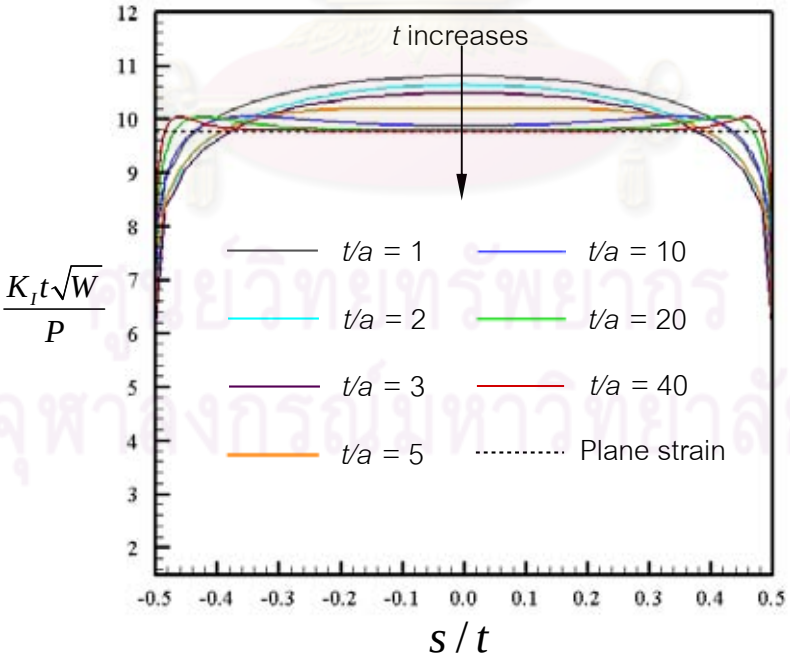

Figure 4.34 Normalized mode-I stress intensity factor versus the normalized distance along the crack front for various thicknesses and G_{zp} / E_p = 1

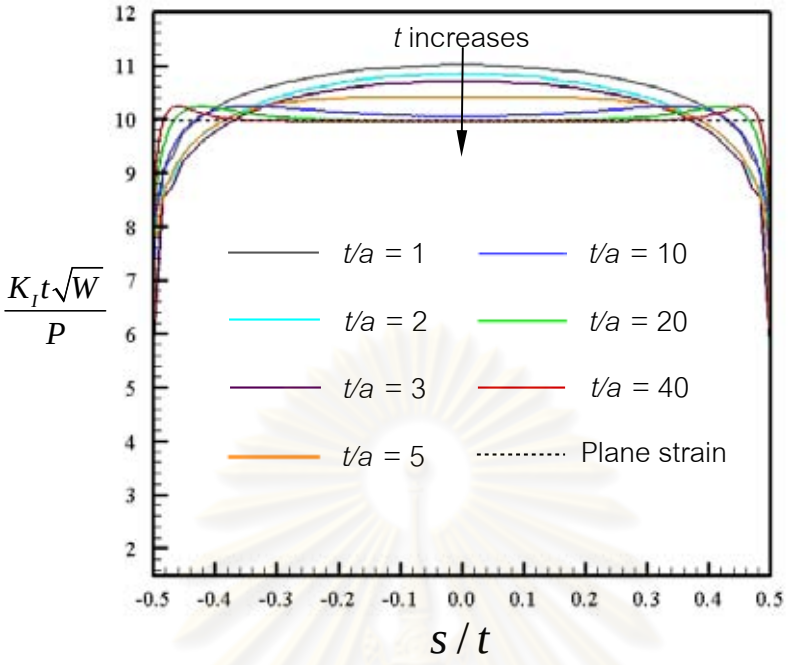

Figure 4.35 Normalized mode-I stress intensity factor versus the normalized distance along the crack front for various thicknesses and G_{zp} / E_p = 2

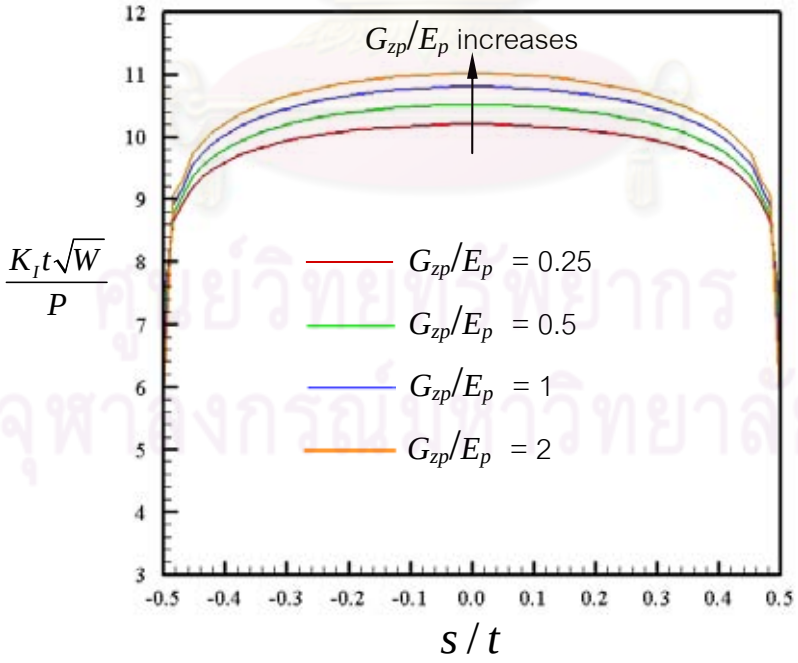

Figure 4.36 Normalized mode-I stress intensity factor versus the normalized distance along the crack front for various modulus ratios G_{zp} / E_p and $t / a = 1$

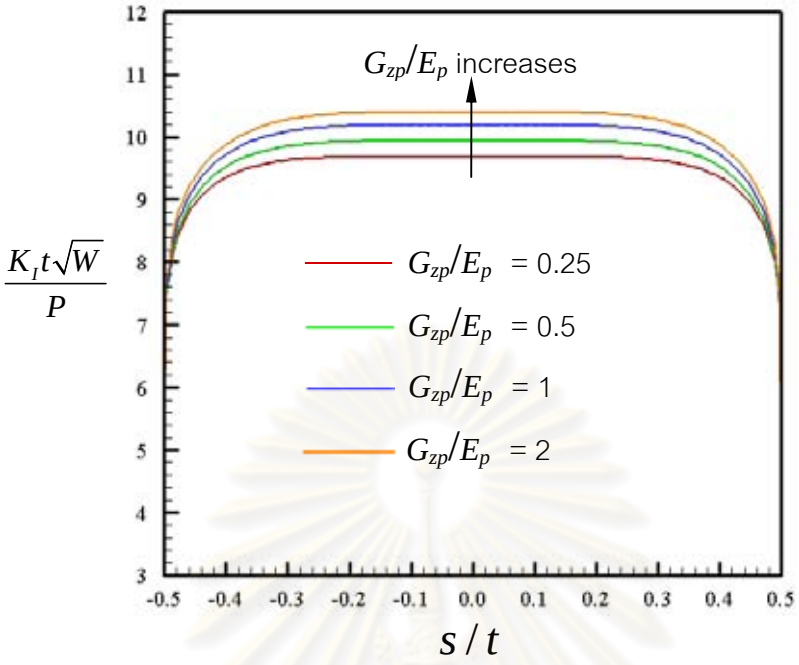

Figure 4.37 Normalized mode-I stress intensity factor versus the normalized distance along the crack front for various modulus ratios G_{zp}/E_p and $t/a = 5$

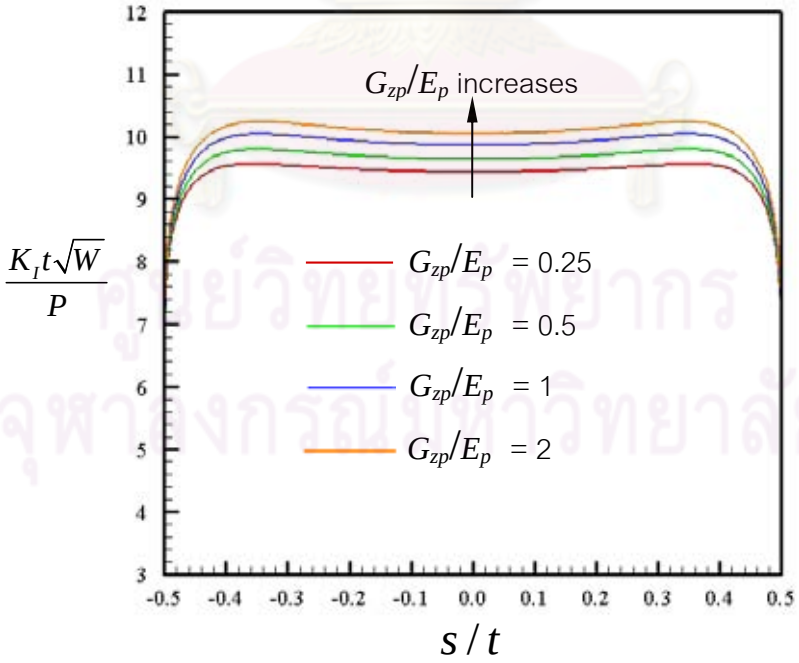

Figure 4.38 Normalized mode-I stress intensity factor versus the normalized distance along the crack front for various modulus ratios G_{zp}/E_p and $t/a = 10$

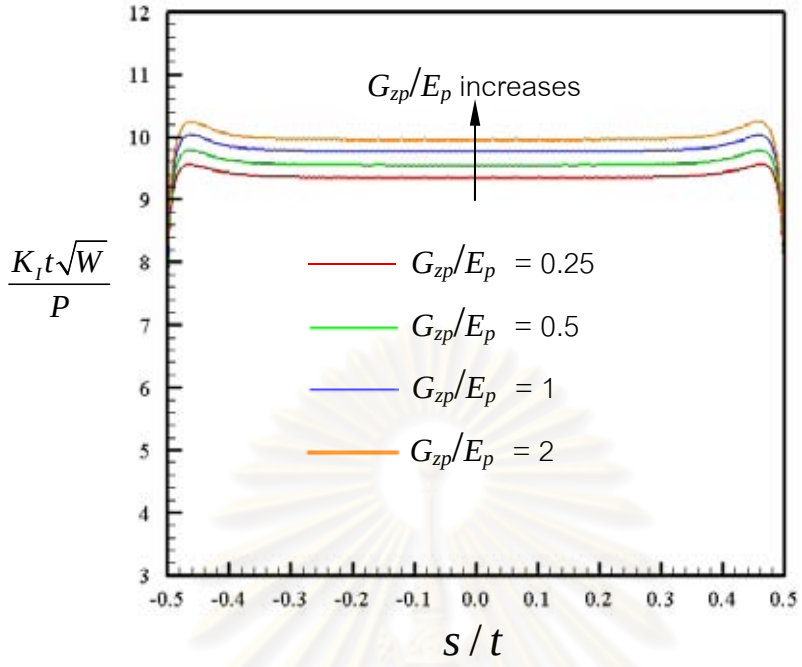

Figure 4.39 Normalized mode-I stress intensity factor versus the normalized distance along the crack front for various modulus ratios G_{zp}/E_p and $t/a = 40$

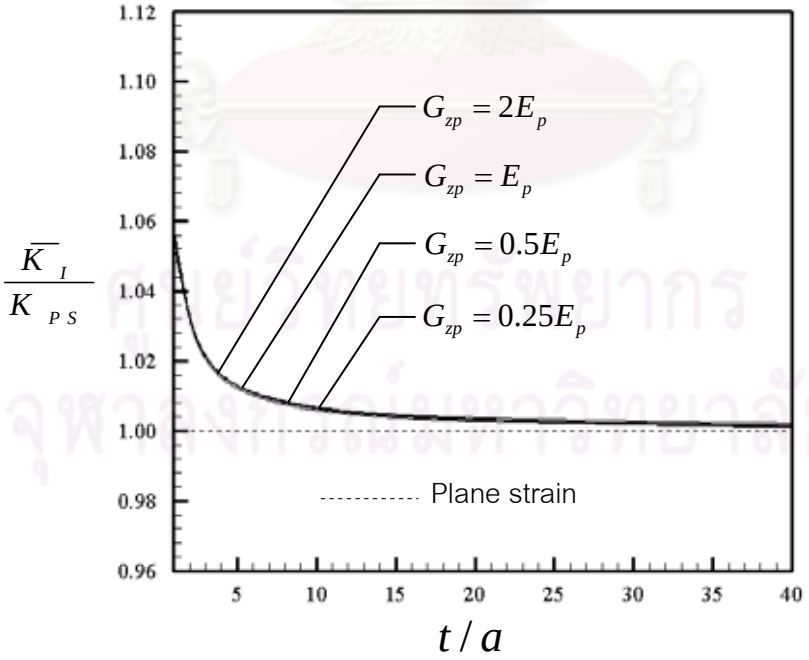

Figure 4.40 Normalized average stress intensity factor versus normalized thickness for different values of G_{zp}/E_p

CHAPTER V

CONCLUSIONS AND REMARKS

An extensive parametric study has been conducted to thoroughly investigate the influence of the thickness and material properties on the behavior of the stress intensity factor along the crack front of the compact tension (CT) specimen. A numerical technique based upon the weakly singular, symmetric Galerkin boundary element method (SGBEM) has been adopted to perform three-dimensional stress analysis of the corresponding boundary value problem. The stress intensity factor has been accurately computed using an explicit formula in terms of the nodal data along the crack front. In the modeling of the relative crack-face displacement in the local region surrounding the crack front, special crack-tip elements with a square-root function embedded in the shape function have been utilized. Use of these crack-tip elements renders the stress intensity factor being captured accurately using relatively coarse meshes.

Geometry of the CT specimen and the loading condition considered in the present study has been chosen to be consistent with ASTM E399-90 except that (i) a notch in front of the crack plane has been removed to simplify the meshing procedure and (ii) the specimen thickness has been varied to investigate its influence on the stress intensity factor across the thickness. A level of mesh refinement has been investigated to ensure that converged numerical results have been obtained for various thicknesses and material properties. To reduce the meshing effort, a simple strategy based on the coordinate stretching and insertion of an interior layer has been exploited to generate meshes for larger thicknesses. In addition, benchmark solutions for some special cases have been compared to verify both the numerical technique used and the meshing scheme.

Extensive numerical experiments have indicated that the specimen thickness shows very significant influence on the value of the mode-I stress intensity

factor across the thickness both in terms of the distribution characteristic and the magnitude. In particular, the stress intensity factors predicted by a three-dimensional model exhibit substantial discrepancy from the plane strain solution for almost the entire crack front when the thickness of the specimen is relatively small compared to other specimen dimensions. However, when the thickness of the specimen is sufficiently large, a plane strain dominated zone has been observed in the central region of the crack front and the size of this zone increases with the specimen thickness. It is important to remark that the behavior of the singular stress field near the vertex (a point where the crack front meets the outer boundary) has been found very complex and the stress intensity factor in this local region generally exhibits the rapid drop when moving towards the vertex. Such complex behavior cannot be captured by using two-dimensional mathematical models. Based on numerous results from a parametric study of material properties for both isotropic and transversely isotropic cases, it has been found that the distribution of the stress intensity factor along the crack front exhibit very weak dependence on the material properties but show significant impact on its magnitude. In addition, material properties have been found to strongly influence the value of the average stress intensity factor across the thickness and the rate of convergence to the plane strain solution. This implies that specimens made of different materials may require different thickness in order to gain the same level of plane strain condition across the crack front.

Results obtained from the present investigation should provide better insight into the behavior of the stress intensity factor along the crack front for brittle materials where the small-scale yielding pertains. This knowledge can be used directly as a useful guideline in the design of test specimens to determine the fracture toughness, an essential material property in fracture mechanics. In general, fracture toughness obtained from experiments can be thickness-dependent if the specimen thickness is not chosen properly. To obtain the fracture toughness that represents the true material property, the specimen thickness must be chosen sufficiently large to ensure that the behavior along the majority of the crack front is dominated by a plane strain condition. A comprehensive, three-dimensional stress analysis (similar to that

employed in the current study) may be performed in advance for various thicknesses to gain an insight into the distribution of the stress intensity factor along the crack front and help to choose proper specimen dimensions.

As a final remark, fracture toughness depends not only on the specimen thickness but also on the temperature, loading rate and the extent of inelastic deformation near the process zone. It has been known that the variation in temperature and loading rate and the plastic zone size ahead of the crack front can have the strong impact on the fracture toughness. Modeling of such influences is not included in this study but still requires further rigorous investigation.

REFERENCES

Alam, J., and Mendelsen, A. (1983). Effect of crack curvature on stress intensity factors. Int. J. Fract. Vol. 23: 317-324.

Anderson, T.L. (2005). Fracture Mechanics: Fundamentals and Applications, Third edition. CRC Press, Taylor & Francis Group. Boca Raton.

ASTM E399-90. (1997). Standard Test Method for Plane-Strain Fracture Toughness of Metallic Materials. The Annual Book of ASTM Standards. 1-31.

Ayhan, A.O., A.C., Laflen, J., McClain, R.D., and Slavik, D. (2003). Fracture analysis of cracks in orthotropic materials using ANSYS. Reports No. GRC370. GEGlobal Research. General Electric Company.

Barnett, D.M., and Asaro, R.J. (1972). The fracture mechanics of slit-like cracks in anistropic elastic media. J. Mech. Phys. Solids. Vol. 20: 353-366.

Barsom, J.M., and Rolfe, S.T. (1999). Fracture and Fatigue Control in Structures: Applications of Fracture, Third edition. ASTM Stock Number: MNL4. West Conshohocken,PA.

Chang, C., and Mear, M.E. (1995). A boundary element method for two dimensional linear elastic fracture analysis. Int. J. Fract. Vol. 74: 219-251.

Chapra, S.C., and Canale R.P. (1990). Numerical Methods for Engineers. McGraw-Hill. New York.

Dirgantara, T., and Aliabadi, M.H. (2002). Stress intensity factors for cracks in thin plates. Engrg. Fract. Mech. Vol. 69: 1465-1486.

Freese, C.E., and Baratta, F.I. (2006). Single edge-crack stress intensity factor solutions. Engrg. Fract. Mech. Vol. 73: 616–625.

Freund, L.B., and Suresh, S. (2003). Thin Film Materials Stress, Defect Formation and Surface Evolution. Cambridge University Press. Cambridge.

Gdoutos, E.E. (2005). Fracture Mechanics: *An Introduction*, Second edition. Springer. The Netherlands.

Hamming, R. (1987). Numerical Methods for Scientists and Engineers. Dover Publications. New York.

Hellan, K. (1984). Introduction to Fracture Mechanics. Mcgraw-Hill. New York.

Hughes, T.J.R. (2000). The finite element method: linear static and dynamic finite element analysis. Dover Publication. New Jersey.

Irwin, G.R. (1957). Analysis of Stresses and Strains near the End of a Crack Traversing a Plate. J. Appl. Mech. Vol. 24: 361-364.

Kanninen, M.F., and Popelar, C.H. (1985). Advanced Fracture Mechanics. Oxford University Press. New York.

Khraishi, T.A., and Demir, I. (2003). On Cauchy singular integrals and stress intensity factors for 2D Mode I cracks in an infinite solid. Mech. Research Communications. Vol. 30: 353-364.

Kotosov, A. (2007). Fracture in plates of finite thickness. Int. J. Solids Struct. Vol. 44: 8259-8273.

Krishna Rao, J.V.S., and Hasebe, N. (1995). Axisymmetric displacement boundary value problem for a penny-shaped crack. Arch. App. Mech. Vol. 66: 1-8.

Kutuk, M.A., Atmaca, N., and Guzelbey, I.H. (2006). Explicit formulation of SIF using neural networks for opening mode of fracture. Engrg. Struct. Vol. 29: 2080-2086.

Kwon, S.W., and Sun, C.T. (2000). Characteristics of three-dimensional stress fields in plates with a through-the-thickness crack. Int. J. Fract. Vol.104, 291-315.

Li, S., and Mear, M.E. (1998). Singularity-reduced integral equations for displacement discontinuities in three-dimensional linear elastic media. Int. J. Fract. Vol. 93: 87-114.

Li, S., Mear, M.E., and Xiao, L. (1998). Symmetric weak-form integral equation method for three dimensional fracture analysis. Comput. Methods Appl. Mech. Engrg. Vol. 151: 435-459.

Martha, L.F., Wawrzynek, P.A. and Ingraffea, A.R. (1993). Arbitrary crack representation using solid modeling. Engrg. With Computers. Vol. 9: 63-82.

Rungamornrat, J. (2006). Analysis of 3D cracks in anisotropic muti-material domain with weakly singular SGBEM. Engrg. Anal. Bound. Elem. Vol. 30: 834-846.

Rungamornrat, J., and Mear, M.E. (2008a). Weakly-singular, weakly-form integral equations for cracks in three-dimensional anisotropic media. Int. J. Solids Struct. Vol. 45: 1283–1301.

Rungamornrat, J., and Mear, M.E. (2008b). A weakly-singular SGBEM for analysis of cracks in 3D anisotropic media. Comput. Methods Appl. Mech. Engrg. Vol. 197: 4319-4332.

Singh, A.K. (2007). Mechanics of Solids. Prentice-Hall of India Private Limited. New Delhi.

Sneddon, I.N. (1946). The Distribution of stress in the Neighbourhood of a Crack in an Elastic Solid. Royal Society of London. Vol. A-187: 229-260.

Sukumar, N., Moran, B., Black, T., and Belytschko, T. (1997). An element-free Galerkin method for three-dimensional fracture mechanics. Comput. Mech. Vol. 20: 170-175.

Staab, G.H. (1999). Laminar Composites. Butterworth-Heinemann. Boston.

Swenson, A.R., and Ingraffea, A.R. (1988). Modeling mixed-mode dynamic crack propagation using finite elements: theory and application. Comput. Mech. Vol. 3: 381-397.

Westergaard, H.M. (1939). Bearing Pressures and Cracks. J. Appl. Mech. Vol.6: 49-53.

Williams, M.L. (1957). On the Stress Distribution at Base of a Stationary Crack. J. Appl. Mech. Vol. 24: 109-114.

Wu, Z. (2006). On the through-thickness crack with a curve front in center-cracked tension Specimens. Engrg. Fract. Mech. Vol. 73: 2600-2613.

Xiao, L. (1998). Symmetric weak-form integral equation method for three-dimensional fracture analysis. Doctoral dissertation. University of Texas at Austin. Texas.

Xin, G., Hangong, W., Xingwu, K., and Liangzhou J. (2010). Analytic solutions to crack tip plastic zone under various loading conditions. Euro. J. Mech. A/Solids. Vol. 29: 738-745.

Xu, G. (2000). A variational boundary integral method for the analysis of three-dimensional cracks of arbitrary geometry in anisotropic elastic solids. J. Appl. Mech. Vol. 67: 403–408.

APPENDICES

Appendix A

The normalized stress intensity factor ($K_I t\sqrt{W}/P$) versus the normalized distance along the crack front (s/t) for various specimen thicknesses $t/a \in \{1, 2, 3, 4, 5, 10, 20, 40\}$ is reported in Figures A.1-A.7 for ν = 0.05, 0.15, 0.20, 0.25, 0.35, 0.40 and 0.45, respectively.

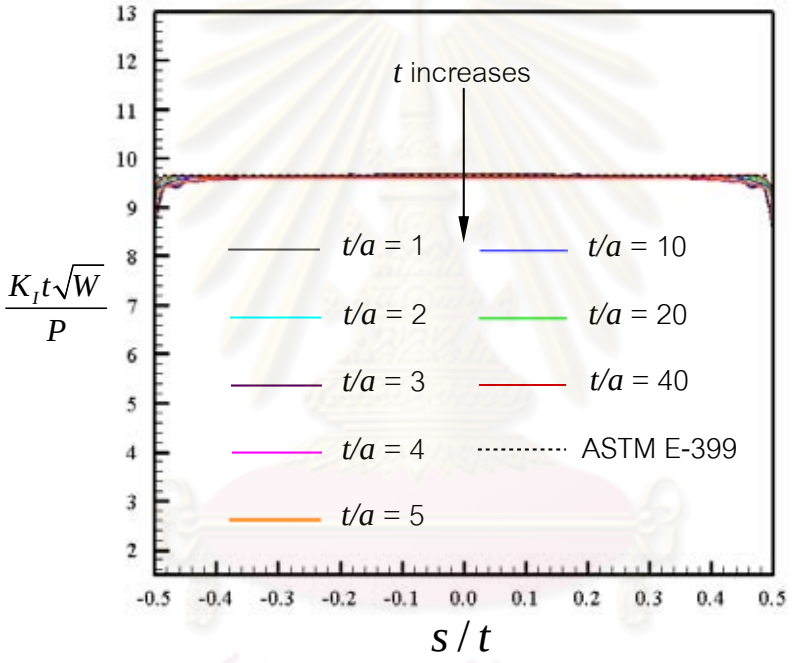

Figure A.1 Normalized mode-I stress intensity factor versus the normalized distance along the crack front for various thicknesses and ν = 0.05

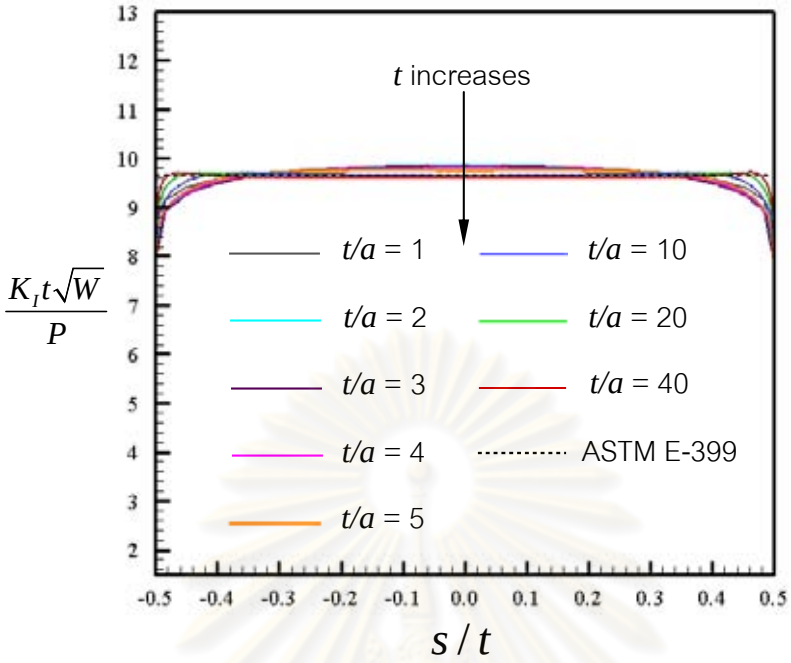

Figure A.2 Normalized mode-I stress intensity factor versus the normalized distance along the crack front for various thicknesses and ν = 0.15

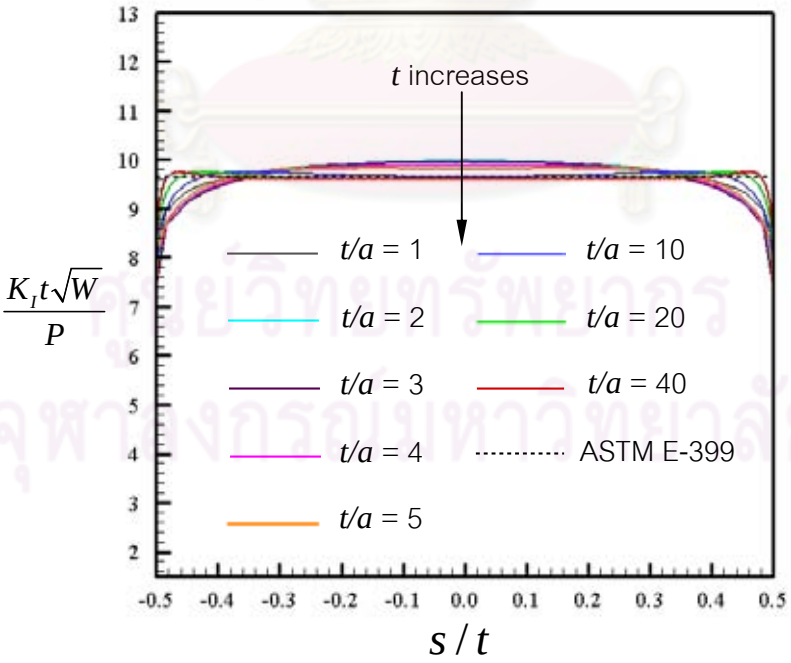

Figure A.3 Normalized mode-I stress intensity factor versus the normalized distance along the crack front for various thicknesses and ν = 0.20

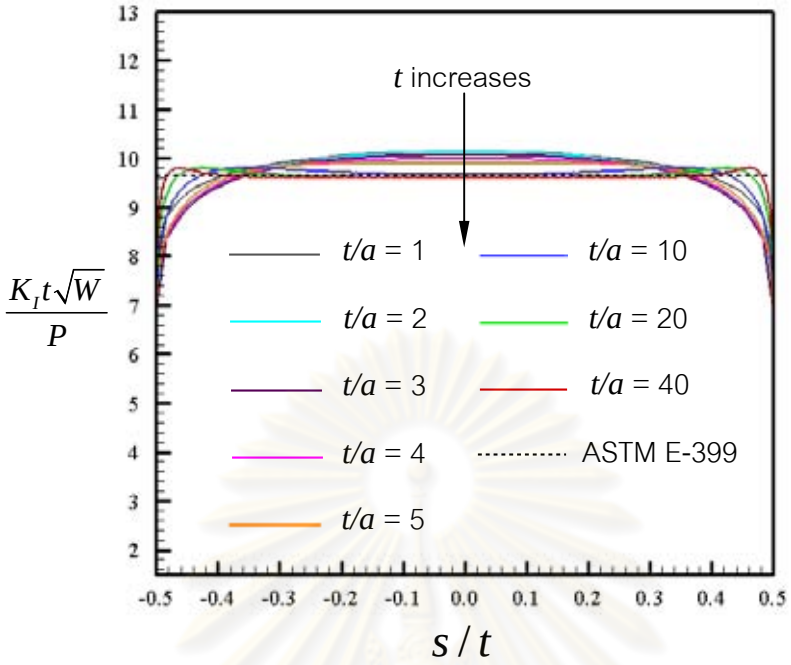

Figure A.4 Normalized mode-I stress intensity factor versus the normalized distance along the crack front for various thicknesses and ν = 0.25

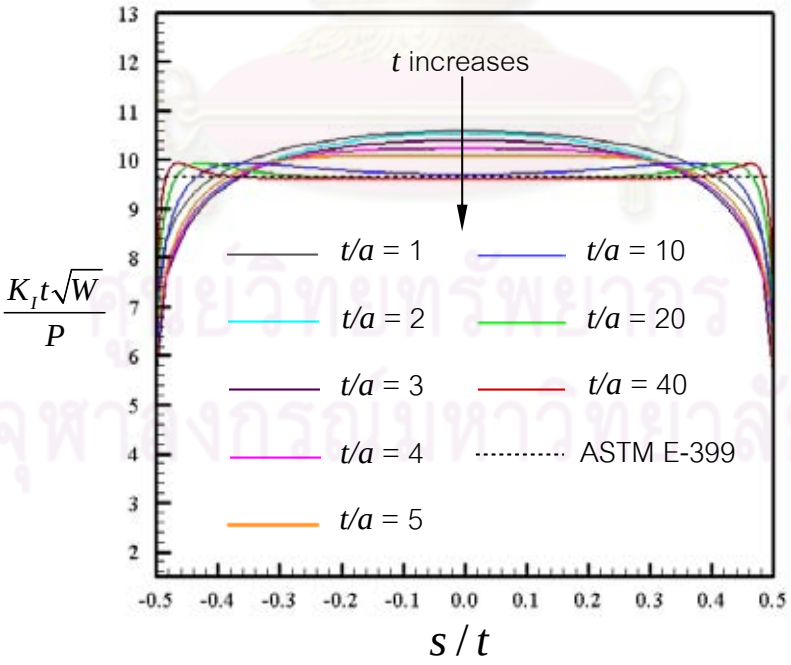

Figure A.5 Normalized mode-I stress intensity factor versus the normalized distance along the crack front for various thicknesses and ν = 0.35

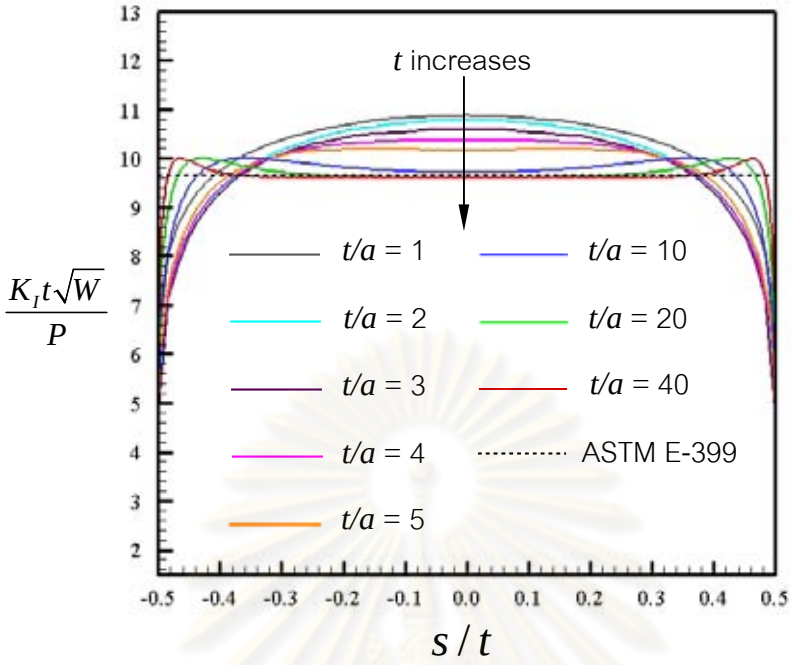

Figure A.6 Normalized mode-I stress intensity factor versus the normalized distance along the crack front for various thicknesses and ν = 0.40

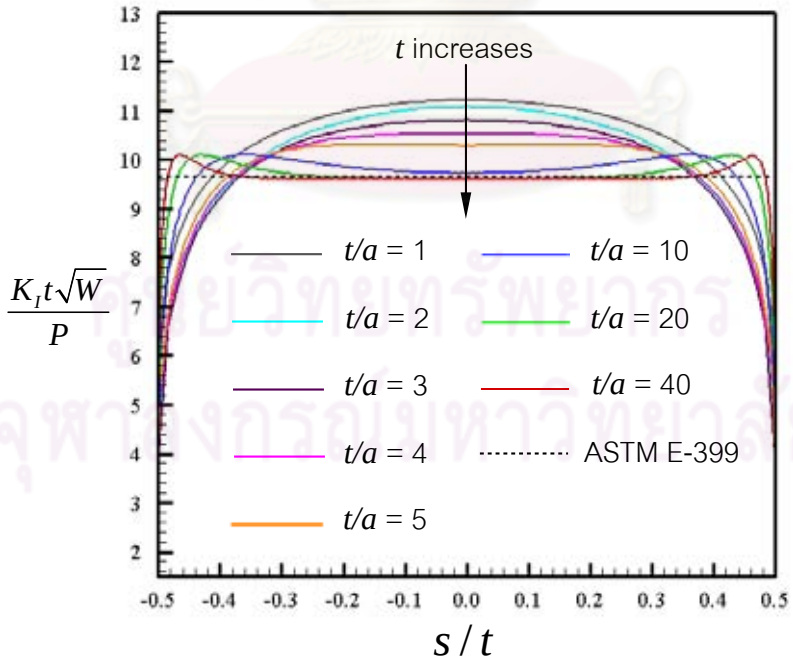

Figure A.7 Normalized mode-I stress intensity factor versus the normalized distance along the crack front for various thicknesses and ν = 0.45

Appendix B

The normalized stress intensity factor ($K_I t\sqrt{W}/P$) versus the normalized distance along the crack front (s/t) for various specimen thicknesses $t/a \in \{1, 2, 3, 5, 10, 20, 40\}$ is reported in Figures B.1-B.4 for ν_p = 0.10, 0.20, 0.40, and 0.50, respectively.

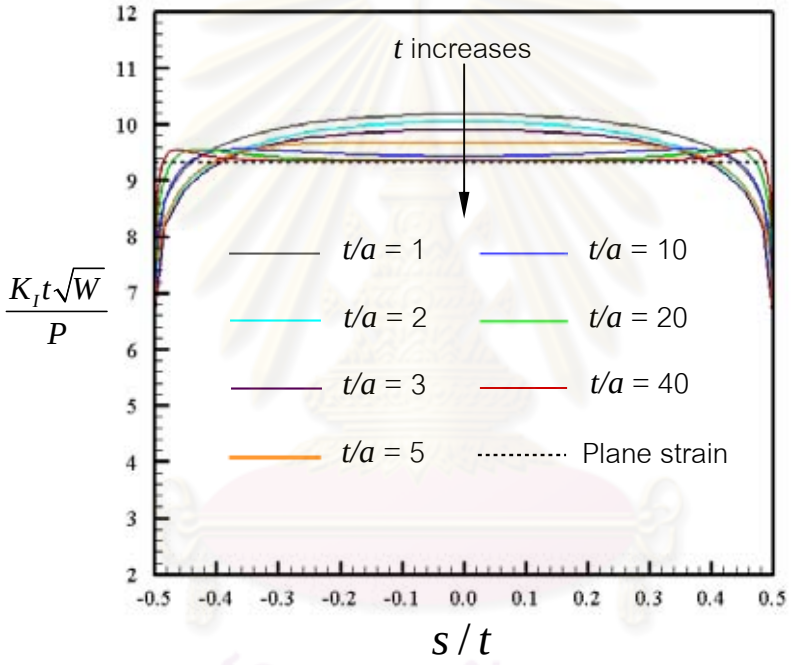

Figure B.1 Normalized mode-I stress intensity factor versus the normalized distance along the crack front for various thicknesses and ν_p = 0.10

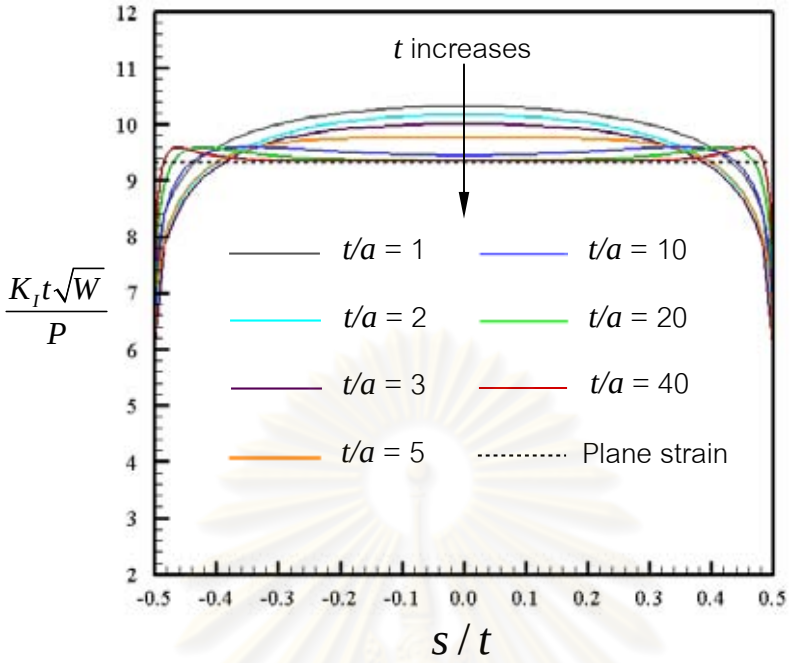

Figure B.2 Normalized mode-I stress intensity factor versus the normalized distance along the crack front for various thicknesses and ν_p = 0.20

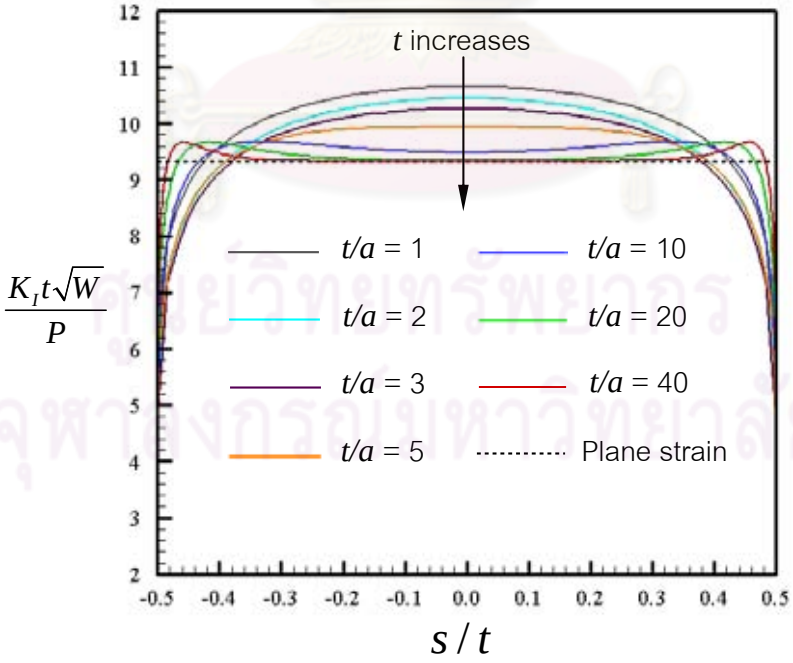

Figure B.3 Normalized mode-I stress intensity factor versus the normalized distance along the crack front for various thicknesses and ν_p = 0.40

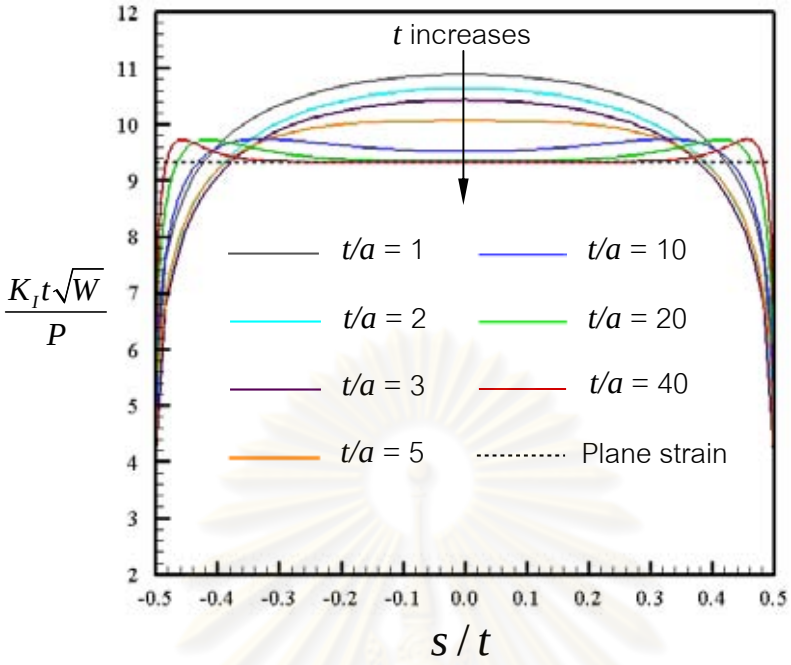

Figure B.4 Normalized mode-I stress intensity factor versus the normalized distance along the crack front for various thicknesses and ν_p = 0.50

BIOGRAPHY

Mr. Kittisak Suisut was born in 1984. He graduated elementary school from Anuban Songkhla school in 1996, high school from Mahavajiravudh Songkhla school in 2002, civil engineering bachelor degree from Prince of Songkla University in 2006. After his postgraduate studies in the Department of Civil Engineering at Chulalongkorn University. The major in his master's degree is structural civil engineering which includes studies and researches in fracture mechanics.